

Hardware Development of a Laboratory-Scale Microgrid Phase 1—Single Inverter in Island Mode Operation

**Base Year Report
December 2000–November 2001**

G. Venkataramanan, M.S. Illindala, C. Houle,
and R.H. Lasseter

*Wisconsin Power Electronics Research Center
Madison, Wisconsin*



NREL

National Renewable Energy Laboratory

1617 Cole Boulevard
Golden, Colorado 80401-3393

NREL is a U.S. Department of Energy Laboratory
Operated by Midwest Research Institute • Battelle • Bechtel

Contract No. DE-AC36-99-GO10337

Hardware Development of a Laboratory-Scale Microgrid Phase 1—Single Inverter in Island Mode Operation

**Base Year Report
December 2000–November 2001**

G. Venkataramanan, M.S. Illindala, C. Houle,
and R.H. Lasseter

*Wisconsin Power Electronics Research Center
Madison, Wisconsin*

NREL Technical Monitor: Holly Thomas

Prepared under Subcontract No. AAD-0-30605-14



NREL

National Renewable Energy Laboratory

1617 Cole Boulevard
Golden, Colorado 80401-3393

NREL is a U.S. Department of Energy Laboratory
Operated by Midwest Research Institute • Battelle • Bechtel

Contract No. DE-AC36-99-GO10337

NOTICE

This report was prepared as an account of work sponsored by an agency of the United States government. Neither the United States government nor any agency thereof, nor any of their employees, makes any warranty, express or implied, or assumes any legal liability or responsibility for the accuracy, completeness, or usefulness of any information, apparatus, product, or process disclosed, or represents that its use would not infringe privately owned rights. Reference herein to any specific commercial product, process, or service by trade name, trademark, manufacturer, or otherwise does not necessarily constitute or imply its endorsement, recommendation, or favoring by the United States government or any agency thereof. The views and opinions of authors expressed herein do not necessarily state or reflect those of the United States government or any agency thereof.

Available electronically at <http://www.osti.gov/bridge>

Available for a processing fee to U.S. Department of Energy
and its contractors, in paper, from:

U.S. Department of Energy
Office of Scientific and Technical Information
P.O. Box 62
Oak Ridge, TN 37831-0062
phone: 865.576.8401
fax: 865.576.5728
email: reports@adonis.osti.gov

Available for sale to the public, in paper, from:

U.S. Department of Commerce
National Technical Information Service
5285 Port Royal Road
Springfield, VA 22161
phone: 800.553.6847
fax: 703.605.6900
email: orders@ntis.fedworld.gov
online ordering: <http://www.ntis.gov/ordering.htm>



Executive Summary

This work summarizes the accomplishments during the first year of a planned three-year project. The overall objective is to develop control software to achieve a synergistic combination of efficient electrical generation systems and the delivery of premium power for critical loads. The planned research and development will enable distributed generation systems to be cost competitive in comparison with conventional power quality solutions such as uninterruptible power systems (UPS) while providing features for higher overall energy efficiency. The planned work will be directly applicable to commercial microturbine generators, fuel cell systems and photovoltaic systems. During the first year, the University of Wisconsin developed tools for this research including a power source emulator (PSE), evaluated system energy storage requirements and inverter vector control, and developed a hardware platform to study inverter operation in island mode of operation.

The need has been demonstrated as critical computing and data processing electronic equipment, which are examples of applications requiring a high quality power supply. Down time of equipment caused by power quality events in such applications has been known to result in significant loss of revenue. Emerging generation systems such as those based on micro-turbines, termed micro-source distributed generation (MSDG) systems here, are rated at small power, so they can be placed close to the load. Invariably, these systems incorporate power electronic converters and are capable of providing UPS functionality, power quality improvement and energy conversion simultaneously at a reasonable cost. However, their operational and control features need to be upgraded in order to meet the requirements of continuous high quality power.

The major issues addressed in the first phase of the project described in this report are (a) internal energy storage requirements for the MSDG system, (b) the modification of a commercial, off the shelf motor drive system inverter to supply utility-grade ac power and (c) investigations on a single inverter MSDG system operating in island mode. In particular, the report provides (a) a methodology for determination of battery energy storage requirements for MSDG inverters, (b) a method for converting a motor drive inverter into a utility-grade inverter effectively and (c) typical characteristics and test results that one may observe using such an inverter in a complex load environment.

- (a) The MSDG systems, under transient conditions in power demand, require a short-term source of energy to meet the stringent demands of premium power systems and, therefore, require auxiliary energy storage equipment to meet sudden changes in load demand during island mode of operation. Key results indicate that lead-acid batteries with deep discharge form the most cost-effective means for realizing energy storage. Flywheels and ultracapacitors represent promising technologies for the future.
- (b) To further develop a demonstration hardware platform, a laboratory-scale MSDG system for island mode of operation was developed. A prototype system was developed and tested. The laboratory-scale MSDG system was found to be an excellent tool for characterizing system performance under island mode of operation.

- (c) Theoretical analyses, computer simulations and experimental investigations of the MSDG system in the island mode feeding a complex set of loads have been carried out for various power factor levels, degrees of imbalance, etc. The voltage regulation properties of inverter systems were found to be less than adequate for loads requiring high quality power under imbalanced and nonlinear load conditions.

These results from the completion of the base year tasks indicate the validity of a laboratory-scale microgrid built using a commercial, off the shelf motor drive inverter using suitable modifications. However, the performance of the inverter system under complex sets of load conditions, such as unbalanced operating conditions, has been sub-optimal. In the subsequent option year tasks, a control strategy for overcoming these problems as well as seamless grid interface while operating multiple inverter units will be demonstrated through the expansion of the hardware system to incorporate multiple inverters and interconnection switchgear. The project activities will emerge as a suitable platform to develop, demonstrate and firmly establish the application of MSDG systems to supply power to sensitive industrial loads.

List of Symbols

η	Inverter efficiency [%]
Ah	Ampere hour rating of the battery [Ah]
ApC	Ampere per cell of the battery [A]
C_b	Battery equivalent capacitance [F]
d	Battery discharge rate specified as a multiple of its C rate
$E_{b, \max}$	Peak energy storage required in the battery [J]
E_{bat}	Energy capacity of the battery [J]
FVpC	Final volts per cell [V]
I_{bat}	Current into the battery [A]
kVA _{fl}	Full-load kVA of the inverter [kVA]
N_c	Number of cells
$P_{b, \max}(t)$	Maximum power drawn from the battery as a function of time [W]
P_{bat}	Power into the battery [kW]
P_{cs}	Power drawn for cold start of a micro-turbine [W]
pf	Power factor of the ac load to the inverter
P_{fl}	Full-load real power demand [W]
P_L	Load power demand [kW]
P_S	Micro-source power response [kW]
R_c	Battery internal resistance [Ω]
R_s	Battery self discharging resistance [Ω]
$T_{r, \max}$	Maximum response time of the micro-source [s]
V_{bat}	Battery terminal voltage [V]
V_{batf}	Terminal voltage of the battery after discharge [V]
V_{cn}	Cell nominal voltage [V]
V_{oc}	Battery open-circuit voltage [V]
w_e	Electrical speed of micro-turbine [rad/s]
w_m	Mechanical speed of micro-turbine [rad/s]
P	Number of poles of the micro-turbine
V_{dc}	Dc bus voltage [V]
I_{dc}	Dc current [A]
V_{ll}	RMS line-line voltage at the diode rectifier input [V]
L_s	Commutating inductance of the diode rectifier [H]
K_v	Model parameter of the micro-turbine
K_e	Model parameter of the micro-turbine
K_x	Model parameter of the micro-turbine
J	Moment of inertia of the micro-turbine and generator [kg-m ²]
M	Mass of the micro-turbine [kg]
r	Shaft radius of the micro-turbine [m]

L_f	Filter inductance of the inverter [H]
R_f	Resistance associated with filter inductor [Ω]
C_f	Filter capacitance of the inverter [F]
L_t	Δ -Y transformer leakage inductance [H]
R_t	Δ -Y transformer leakage resistance [Ω]
V_{xnL}	Phase-neutral voltage at the load terminals (for phase x) [V]
I_{Lx}	Load current (for phase x) [A]
$I_{ind\ x}$	Filter inductor current (for phase x) [A]
P_o	Load power demand [W]
s	Time interval [s]

Table of Contents

No.	Chapter	Page
	List of Figures	vi
	List of Tables	xiii
1	Project Overview	1
2	Energy Storage in Distributed Generation	10
3	Battery Design Issues	15
4	Battery Modeling and Simulation	26
5	Micro-Turbine Modeling and Emulation	31
6	Motor Drive Inverter into MSDG Inverter Conversion	67
7	Island Mode MSDG System Studies	83
8	Conclusions and Future Work	142
9	References	147

List of Figures

Figure 1:	Block diagram of micro-turbine power generation system.....	3
Figure 2:	Block diagram of fuel-cell power generation system	3
Figure 3:	Block diagram of proposed model system.....	7
Figure 4:	One-line conceptual schematic of the experimental test bed.....	8
Figure 5:	CBEMA curves specifying acceptable voltage sensitivity levels..	10
Figure 6:	Block diagram of a micro-turbine-based distributed generation system	11
Figure 7:	Typical step response of a micro-turbine.....	13
Figure 8:	Block diagram of an MSDG system with battery storage	15
Figure 9:	Cell discharge voltage versus time for a lead-acid battery	18
Figure 10:	Peak current and voltage per cell of a lead-acid battery for a high-rate discharge.....	19
Figure 11:	Thevenin equivalent circuit of the battery	20
Figure 12:	Instantaneous power curves of a lead-acid battery for a high-rate discharge	20
Figure 13:	A flowchart describing the design approach.....	25
Figure 14:	MTG response for step change in load	26
Figure 15:	Equivalent circuit of a lead-acid battery	27
Figure 16:	Step response of a battery-based MSDG system	30
Figure 17:	Micro-turbine block diagram	32
Figure 18:	Block diagram of micro-turbine generator connection to utility/load	33
Figure 19:	Power command to the micro-turbine for load change in 15-kW steps.....	34
Figure 20:	Output power of micro-turbine for load change in 15-kW steps...	35
Figure 21:	Shaft speed of micro-turbine for load change in 15-kW steps.....	35
Figure 22:	Dc link voltage of micro-turbine for load change in 15-kW steps.....	36
Figure 23:	Power command of micro-turbine for load change in 30-kW steps.....	37
Figure 24:	Output power of micro-turbine for load change in 30-kW steps...	37
Figure 25:	Shaft speed of micro-turbine for load change in 30-kW steps.....	38
Figure 26:	DC link voltage of micro-turbine for load change in 30-kW steps.....	38
Figure 27:	Circuit model of micro-turbine with passive rectifier.....	39
Figure 28:	Shaft speed model of a micro-turbine.....	41

Figure 29:	Curve-fit shaft speed model of a micro-turbine	42
Figure 30:	Power command to the curve-fit shaft speed model	43
Figure 31:	Output power from the curve-fit shaft speed model	44
Figure 32:	Rotor speed from the curve-fit shaft speed model	44
Figure 33:	DC link voltage from the curve-fit shaft speed model	45
Figure 34:	Torque input model of a micro-turbine	46
Figure 35:	Augmented torque input model of a micro-turbine	48
Figure 36:	Input torque for the torque input model	49
Figure 37:	Inverter load current for the torque input model	49
Figure 38:	Output power from the torque input model	50
Figure 39:	Shaft speed from the torque input model	50
Figure 40:	DC link voltage from the torque input model	51
Figure 41:	Block diagram of the “Bang-Bang” controller	52
Figure 42:	“Bang-Bang” controller and Honeywell™ micro-turbine model ..	53
Figure 43:	Honeywell™ micro-turbine model	53
Figure 44:	Torque input provided by the “Bang-Bang” controller	54
Figure 45:	Shaft speed from Honeywell™ micro-turbine model with the controller	55
Figure 46:	Dc link voltage from Honeywell™ micro-turbine model with the controller	55
Figure 47:	Output power from Honeywell™ micro-turbine model with the controller	56
Figure 48:	Rotor speed from Honeywell™ micro-turbine model with the controller	56
Figure 49:	Dc voltage from Honeywell™ micro-turbine model with the controller	57
Figure 50:	Output power from Honeywell™ micro-turbine model with the controller	57
Figure 51:	Output power from step changes in load	58
Figure 52:	Half-bridge dc-dc converter topology	59
Figure 53:	Simplified dynamic model of half-bridge converter	60
Figure 54:	Simulink™ model of dynamic model of dc-dc converter	60
Figure 55:	Dc-dc converter system with voltage controller	61
Figure 56:	Proportional control of dc bus voltage	61
Figure 57:	Dc output voltage for step changes in load	62
Figure 58:	Output power for step changes in load	62
Figure 59:	Augmented controller with inverter response	64
Figure 60:	DC voltage of model with the augmented controller	64
Figure 61:	Output power of converter with the augmented controller	65

Figure 62:	Block diagram of the island distributed generation system	68
Figure 63:	Circuit schematic of the inverter-based island micro-source distributed generation system	69
Figure 64:	Single-phase equivalent circuit of the LC filter for the PWM inverter	70
Figure 65:	Bode plot of $\left \frac{V_L(s)}{V_{inv}(s)} \right $	71
Figure 66:	Single-phase equivalent circuit of the LC filter for a nonlinear load that is represented as a current source	71
Figure 67:	Bode plots of $\left \frac{I_{ind}(s)}{I_L(s)} \right $ and $\left \frac{V_{cap}(s)}{I_L(s)} \right $	72
Figure 68:	Circuit schematic of the MSDG system for simulation in MATLAB Simulink™	76
Figure 69:	Load terminal voltages and load currents	77
Figure 70:	Load terminal voltage phasor diagram	78
Figure 71:	Load current phasor diagram	78
Figure 72:	Filter inductor current in three phases	79
Figure 73:	Load terminal voltages – V_{anL} & V_{bnL} and load currents – I_{La} & I_{Lb}	80
Figure 74:	Filter capacitor voltages – V_{ACf} & V_{BCf} and filter inductor currents – $I_{ind a}$ & $I_{ind b}$	80
Figure 75:	Phasor diagram of the load terminal voltages	81
Figure 76:	Phasor diagram of the load currents	82
Figure 77:	Photograph of inverter incorporating LC filter and transformer ...	82
Figure 78:	Single-phase equivalent circuit of the MSDG system	85
Figure 79:	Real power delivered at full load as a function of power factor	87
Figure 80:	Reactive power delivered at full load as a function of power factor	88
Figure 81:	Voltage regulation curve for leading power factor loads for an island mode MSDG system	89
Figure 82:	Voltage regulation curve for leading power factor loads for an island mode MSDG system	90
Figure 83:	Load characteristics of an MSDG system for leading power factors	91
Figure 84:	Load characteristics of an MSDG system for lagging power factors	91
Figure 85:	Inverter output voltage for constant load terminal voltage (for leading power factors)	92

Figure 86:	Inverter output voltage for constant load terminal voltage (for lagging power factors)	93
Figure 87:	Simplified schematic of the circuit to test the regulation of Δ -Y transformer secondary voltage	94
Figure 88:	Results of regulation test against variation in balanced resistive load	95
Figure 89:	Results of regulation test against variation in balanced inductive load	96
Figure 90:	Results of regulation test against variation in balanced capacitive load	97
Figure 91:	Results of regulation test against variation in unbalanced resistive load	98
Figure 92:	Results of regulation test against variation in unbalanced inductive load	99
Figure 93:	Results of regulation test against variation in unbalanced capacitive load	100
Figure 94:	Schematic of the regulation test circuit containing the equivalent circuit representation of the Δ -Y transformer	102
Figure 95:	Transformer secondary terminal voltage waveform for a balanced resistive load	103
Figure 96:	FFT of the transformer secondary terminal voltage in three phases for a balanced resistive load	103
Figure 97:	Phasor diagram of the three-phase voltages for a balanced resistive load	104
Figure 98:	Three-phase filter inductor current waveform for a balanced resistive load	104
Figure 99:	Three-phase load current waveform for a balanced resistive load	105
Figure 100:	FFT of the load current in three phases for a balanced resistive load	105
Figure 101:	Phasor diagram of the three-phase currents for a balanced resistive load	106
Figure 102:	Instantaneous powers in three phases (top) and total power (bottom) for a balanced resistive load	106
Figure 103:	Transformer secondary terminal voltage waveform for a balanced inductive load	108
Figure 104:	FFT of the transformer secondary terminal voltage in three phases for a balanced inductive load	108
Figure 105:	Phasor diagram of the three-phase voltages for a balanced inductive load	109
Figure 106:	Three-phase filter inductor current waveform for a balanced inductive load	109

Figure 107:	Three-phase load current waveform for a balanced inductive load.....	110
Figure 108:	FFT of the load current in three phases for a balanced inductive load.....	110
Figure 109:	Phasor diagram of the three-phase currents for a balanced inductive load.....	111
Figure 110:	Instantaneous powers in three phases and total power for a balanced inductive load.....	111
Figure 111:	Transformer secondary terminal voltage waveform for a balanced capacitive load	113
Figure 112:	FFT of the transformer secondary terminal voltage in three phases for a balanced capacitive load	113
Figure 113:	Phasor diagram of the three-phase voltages for a balanced capacitive load	114
Figure 114:	Three-phase filter inductor current waveform for a balanced capacitive load	114
Figure 115:	Three-phase load current waveform for a balanced capacitive load.....	115
Figure 116:	FFT of the load current in three phases for a balanced capacitive load.....	115
Figure 117:	Phasor diagram of the three-phase currents for a balanced capacitive load	116
Figure 118:	Instantaneous powers in three phases and total power for a balanced capacitive load	116
Figure 119:	Transformer secondary terminal voltage waveform for an unbalanced resistive load	118
Figure 120:	FFT of the transformer secondary terminal voltage in three phases for an unbalanced resistive load.....	118
Figure 121:	Phasor diagram of the three-phase voltages for an unbalanced resistive load	119
Figure 122:	Three-phase filter inductor current waveform for an unbalanced resistive load	119
Figure 123:	Three-phase load current waveform for an unbalanced resistive load.....	120
Figure 124:	FFT of the load current in three phases for an unbalanced resistive load	120
Figure 125:	Phasor diagram of the three-phase currents for an unbalanced resistive load	121
Figure 126:	Instantaneous powers in three phases and total power for an unbalanced resistive load	121
Figure 127:	Transformer secondary terminal voltage waveform for an unbalanced inductive load.....	123

Figure 128:	FFT of the transformer secondary terminal voltage in three phases for an unbalanced inductive load	123
Figure 129:	Phasor diagram of the three-phase voltages for an unbalanced inductive load.....	124
Figure 130:	Three-phase filter inductor current waveform for an unbalanced inductive load.....	124
Figure 131:	Three-phase load current waveform for an unbalanced inductive load.....	125
Figure 132:	FFT of the load current in three phases for an unbalanced inductive load.....	125
Figure 133:	Phasor diagram of the three-phase currents for an unbalanced inductive load.....	126
Figure 134:	Instantaneous powers in three phases and total power for an unbalanced inductive load.....	126
Figure 135:	Transformer secondary terminal voltage waveform for an unbalanced capacitive load	128
Figure 136:	FFT of the transformer secondary terminal voltage in three phases for an unbalanced capacitive load	128
Figure 137:	Phasor diagram of the three-phase voltages for an unbalanced capacitive load	129
Figure 138:	Three-phase filter inductor current waveform for an unbalanced capacitive load	129
Figure 139:	Three-phase load current waveform for an unbalanced capacitive load.....	130
Figure 140:	FFT of the load current in three phases for an unbalanced capacitive load	130
Figure 141:	Phasor diagram of the three-phase currents for an unbalanced capacitive load	131
Figure 142:	Instantaneous powers in three phases and total power for an unbalanced capacitive load	131
Figure 143:	Filter capacitor line voltage ac & bc and filter inductor current a & b for a resistive load.....	132
Figure 144:	Load terminal voltage a & b and load current a & b for a resistive load	133
Figure 145:	Phasor diagrams of load terminal voltage and load current for a resistive load.....	133
Figure 146:	Filter capacitor line voltage ac & bc and filter inductor current a & b for a series RL load.....	134
Figure 147:	Load terminal voltage a & b and load current a & b for a series RL load	135
Figure 148:	Phasor diagrams of load terminal voltage and load current for a series RL load.....	135

Figure 149:	Load terminal voltage a & b and load current a & b for a parallel RC load	136
Figure 150:	Phasor diagrams of load terminal voltage and load current for a parallel RC load	136
Figure 151:	Load terminal voltage a & c and load current a & c for an unbalanced load	137
Figure 152:	Phasor diagrams of load terminal voltage and load current for an unbalanced load	138
Figure 153:	Load terminal voltage a & b and load current a & b for a three-phase diode rectifier.....	139
Figure 154:	Transient waveforms – load terminal voltage a & b and load current a & b for a resistive load.....	140
Figure 155:	Transient waveforms – load terminal voltage a & b and load current a & b for a series RL load.....	141
Figure 156:	Photograph of cable tray system that forms the backbone of the laboratory-scale microgrid	145

List of Tables

Table 1:	Typical capacity variation at different discharge rates	17
Table 2:	PNGV charge sustaining HEV, battery specification	21
Table 3:	LC circuit parameters.....	73
Table 4:	Circuit parameters for simulation studies	75
Table 5:	Load parameters for the simulation studies	76
Table 6:	Circuit parameters for the island-mode MSDG system.....	84
Table 7:	Filter and transformer impedances in per-unit.....	93
Table 8:	Summary of results on load regulation	100
Table 9:	RisACE2000™ measurements for a resistive load	133
Table 10:	RisACE2000™ measurements for a series RL load	135
Table 11:	RisACE2000™ measurements for a parallel RC load	136
Table 12:	RisACE2000™ measurements for an unbalanced load	138
Table 13:	RisACE2000™ measurements for three-phase diode bridge rectifier load	139

1 Project Overview

This project activity is focused on a systems approach to using clusters of micro-sources with storage to bring high value to the customer of electrical energy. Advantages to customer applications include: deferred distribution cost, local voltage control and reliability, coordinated demand side management and premium power. The project addresses the control and placement of distributed resources as a solution to the sensitive load problem. In particular, the focus is on systems of distributed resources that can switch from grid connection to island operation without causing problems for critical loads.

The presence of power electronic interfaces in fuel cells, photovoltaics, micro-turbines and storage technologies creates a very different situation when compared with more conventional synchronous generator sources in power sources and standby emergency power systems. This project takes advantage of the properties of the power electronic interface to provide additional functionality to distributed generators. The concepts are verified using computer simulation models, and their feasibility is established on a hardware test bed developed for that purpose. The hardware demonstration component is based on a three-phase 480 V distribution test bed with emulated micro-sources and storage, passive loads, induction machines and adjustable speed drives. This report describes the activities from the first phase of the project.

1.1 Sensitive Loads

In recent years, various industries are installing precision equipment such as robots, automated machine tools and materials processing equipment to realize increased product quality and productivity. These may be termed critical electric loads or sensitive loads. As a result, modern industrial facilities depend on sensitive electronic equipment that can be shut down suddenly by power system disturbances. Although voltage spikes, harmonics and grounding-related problems may cause such problems, they can be overcome through appropriate design of robustness into the control circuits. A majority of the problems occur because of the fact that processes are not able to maintain precision control because of power outages that last a single cycle or voltage sags, which last more than two cycles. A few cycles of disturbance in voltage waveform may cause a motor to slow down and draw additional reactive power. This depresses the voltage even deeper, eventually leading to a process shut down. This results in equipment malfunctioning and high restart cost. The number of outages, voltages dips and duration is important. In the manufacture of computer chips alone, losses from sags amount to \$1 million to \$4 million per occurrence, accordance to Central Hudson Gas & Electrical Corp. Poor power quality, particularly voltage sags, are becoming increasingly unacceptable in competitive industries in which product defects can mean dire economic consequences.

Electric utilities have traditionally responded to such needs of the customers and their demands for reliable electric supply to a high degree of satisfaction. This has been achieved through increased capital investment in generation, transmission and

distribution infrastructure. Increased investments to maintain a quality infrastructure had been possible in a regulated economic scenario of guaranteed prices and returns.

However, in the unfolding deregulated operating environment, electric utilities face a competitive marketplace in which it is increasingly difficult to commit capital expenses to meet the needs of a select group of customers. The problem is exacerbated by the fact that increased demands in power quality by customers have coincided with reduced availability of capital for infrastructure investment. In addition, the technologies such as dynamic voltage restorers (DVR) necessary for providing such ultra-reliable power supply for large and sensitive customers is just becoming available.

Faced with such a scenario, several sensitive consumers of electricity have taken to installing large uninterruptible power supply (UPS) systems to meet contingent situations. This is particularly common in the information industry segment. These systems convert utility power into dc, which is stored in large battery banks and converted back into ac to feed customer equipment. This solution is expensive because the initial cost of the equipment is high, and the operating cost of equipment is also high because of losses. The overall demand for UPS and standby power supply equipment has been growing rapidly in the past years, illustrating the severity of the problem.

To address this problem, concepts such as custom power and premium power have been proposed, with modest success. Typically, these solutions do not integrate distributed power generation into developing solutions to the sensitive load problem. Recent investigations have shown that there is a high degree of match between the capabilities of distributed generation systems and the demands of sensitive loads, and this can be a viable and competitive solution to the problem. The work during the first year of the project addressed the control and placement of distributed generation as a solution to the sensitive load problem.

1.2 Distributed Generation

Small, distributed generation (DG) technologies such as micro-turbines, photovoltaics and fuel cells are gaining wide interest because of rapid advances in technologies. The deployment of these generation units on distribution networks could potentially lower the cost of power delivery by placing energy sources nearer to the demand centers. The capacity of the devices ranges from 1 kW to 2 MW in power level.

One of the cost-effective DG technologies is a small, gas-fired micro-turbine in the 25- to 100-kW range that can be mass-produced. It is designed to combine the reliability of on-board commercial aircraft generators with the low cost of automotive turbochargers. A block diagram of the system is illustrated in Figure 1. The prime mover is a high-speed turbine (50,000-90,000 rpm) with airfoil bearings. The ac generator, coupled to the turbine, typically generates power at about 1 to 2 kHz. It is rectified into dc. A three-phase inverter converts the dc into utility-grade ac for the load. Examples include Allison Engine Cos.' 50-kW generator and Capstone's 30-kW system.

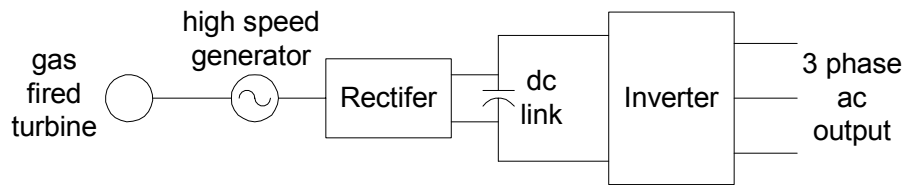


Figure 1: Block diagram of micro-turbine power generation system

Fuel cells are also well suited for distributed generation applications. They offer high efficiency and low emissions, but today's costs are high. Phosphoric acid cells are commercially available in the 200-kW range, and solid oxide and molten carbonate cells have been demonstrated. In October 1997, the U.S. Department of Energy and Arthur D. Little unveiled the “first-ever on-board gasoline-powered fuel cell for the automobile.” The possibility of using gasoline as a fuel for cells has resulted in a major development effort by automotive companies. This work is focused toward the polymer electrolyte membrane (PEM) fuel cells. Ballard Power Systems expects to sell a 250-kW PEM fuel-cell based generator at prices competitive with the grid to shopping malls and large commercial buildings.

Mixed fuel cell and micro-turbine systems will also be available as distributed generation. In a joint DOE-Westinghouse project, a solid oxide fuel cell was combined with a gas turbine, creating a combined cycle power plant. It has an expected electrical efficiency of greater than 70%. The expected power levels range from 250 kW to 2.5 MW.

A block schematic of a fuel cell-based utility-grade power generation system is shown in Figure 2. The primary energy conversion device consists of the fuel cell stack, which converts fuel input into electrical energy feeding the dc link. As in the case of the micro-turbine generation system, the inverter converts dc into three-phase utility-grade ac power.

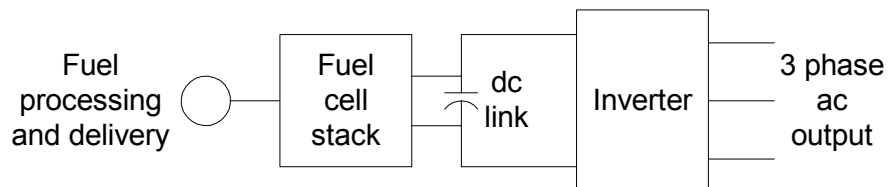


Figure 2: Block diagram of fuel-cell power generation system

Other distributed resources include more than small generators and fuel cells. Storage technologies such as batteries, ultra-capacitors and flywheels play an important role. Combining storage with micro-sources provides peak power and ride-through capabilities during disturbances. Storage systems are far more efficient than 5 years ago. Flywheel

systems can deliver 700 kW for 5 seconds while 28-cell ultra-capacitors can provide up to 12.5 kW for a few seconds.

One of the common features of virtually all DG devices is the use of a common dc link and an inverter as the interface between the primary electric power source and the utility-grade power system. This important feature will enable the investigations being conducted herein to be applicable to several platforms, independent of the primary energy source.

1.3 Development Scenarios for Distributed Generation

Distributed generation systems provide an alternative to traditional investments made by electrical distribution companies. As demand increases, or becomes uncertain, DG resources make it possible to defer or delay, indefinitely, traditional capacity improvements necessary by distributing generation and storage throughout the system. To meet certain customer demands on reliability and power levels, it may be less expensive to apply DG locally at a load location than to upgrade to provide the same level of service to all customers. Integrated service companies, which provide gas and electricity, may have an incentive to provide electricity through local generation and heat as the byproduct to the same customer at the same location, thereby maximizing resource utilization.

DG devices may be purchased and installed by consumers of electric power in various commercial and industrial settings as a supplement to electric power purchased from utilities. In such settings, they may also be used in the role of more traditional standby or emergency electric power generation systems based on reciprocating engine-generator sets.

The capital costs associated with DG systems range from \$500/kW to \$5,000/kW for technologies ranging from turbogenerators to fuel cells and solar photovoltaics. This price level is considered rather high to provide the “market pull” necessary for DG to be applied widely in either of the above scenarios. However, for these technologies to become widespread and realize the fullest potential they are capable of, they need to be applied in less cost-sensitive applications, such as those posed by sensitive loads in industrial and commercial applications, to gain acceptance.

This market scenario will allow the DG technology to be adopted by high-performance applications, and as they gain acceptance in the marketplace and the technology matures, they will see more penetration in the power network. Hence, there is a need to definitively establish the feasibility of DG devices to solve the sensitive load problems.

1.4 Distributed Generation for Sensitive Loads

As discussed previously, the UPS systems and custom power devices provide alternate approaches to deliver ultra-reliable power to sensitive load centers. UPS systems typically use battery energy storage to provide power to sensitive loads. Custom power

systems for controlling voltage disturbances use a voltage source inverter, which injects reactive power into the system to achieve voltage correction. One method is to inject shunt reactive current; the other is to inject series voltage. These systems are effective in protecting against single-phase voltage sags (or swells) due to distant faults or unbalanced loads. These systems are costly and complex and are needed only during voltage disturbance events.

At the outset, it is clear that DG devices can increase reliability and power quality by allowing them to be placed near the load. This provides for a stiffer voltage at the load and UPS functions during loss of grid power. At a more subtle level, the power electronic interface found on virtually all DG devices, namely the inverter, has the potential to control voltage sags and imbalances.

Hence, through appropriate implementation of control functions and integration of storage with the system, DG devices can be made to provide additional functionality, which is superior to UPS systems and various custom power devices. This provides for a more robust system for protection against single-phase voltage drops and swells. However, state-of-the-art DG devices have not yet been shown to be capable of providing functionalities in a definitive manner. Hence, it is necessary to develop appropriate design techniques to integrate storage and micro-sources through control techniques to provide the functionality and demonstrate them in hardware before they can be deployed in the field. It is the broad objective of this proposal to demonstrate such features.

1.5 Technical Challenges

DG devices are fundamentally different from conventional central station generation technologies. For instance, fuel cells and battery storage devices have no moving parts and are linked to the system through electronic interfaces. Micro-turbines have extremely lightweight moving parts and also use electronic system interfaces. The dynamic performance of such inertialess devices cannot be modeled simply as if they were scaled-down central station units. One large class of problems is related to the fact that micro-turbines and fuel cell have slow response and are inertialess. It must be remembered that the current power systems have storage in the generators' inertia. When a new load comes on line, the initial energy balance is satisfied by the system's inertia. This results in a slight reduction in system frequency. A system with clusters of micro-generators could be designed to operate in an island mode to provide some form of storage to provide the initial energy balance as "virtual inertia."

A system with clusters of micro-generators and storage could be designed to operate both in an island mode and in satellite mode, connected to the power grid.

It is essential to have good control of the power angle and the voltage level by means of the inverter. Control of the inverter's frequency dynamically controls the power angle and the flow of the real power. To prevent overloading the inverter and the micro-sources, it

is important to ensure that the inverter takes up load changes in a predetermined manner, without communication.

The control of inverters used to supply power to an ac system in a distributed environment should be based on information available locally at the inverter. In a system with many micro-sources, communication of information between systems is impractical. The communication of information may be used to enhance system performance, but it must not be critical for system operation. Essentially, this implies that the inverter control should be based on terminal quantities.

More than 90% of voltage disturbances in the utility lines are single-phase voltage sags caused by momentary line-to-ground faults in distribution systems. Hence, the control strategy of the inverter should be able to meet situations when the utility grid has residual imbalances in voltage and when the load system has imbalances in current.

When multiple units are connected in parallel at the same location or in close proximity, thereby forming a “microgrid,” the individual inverters should be capable of sharing active and reactive power in a predetermined manner, and circulating power should be avoided.

It may be expected that the application centers of DG systems may consist of nonlinear loads such as rectifiers. The control strategy of the inverters should be such that they are capable of supplying real and reactive power demands as well as the harmonic currents necessary to feed such loads without exacerbating the situation.

1.6 Systems Approach

As has been discussed previously, virtually all DG technologies require power electronics to interface with the power network and its loads. In all cases, there is a dc voltage source, which must be converted to an ac voltage source at the required frequency, magnitude and phase angle. In most cases, the conversion will be performed using a voltage source inverter. Hence, the inverter forms the heart of the system. Addressing most technical challenges discussed above requires an examination of the control of the inverter. As a result, the primary focus of the proposed research will be centered on the operation and control of the inverters in a microgrid.

However, the properties of the primary power source represent an important limitation of the DG device with respect to power and energy flow. For instance, a micro-turbine requires about a 10 s interval for a 50% change in power output. A fuel cell requires about a 10 s interval for a 15% change in power output but requires a recovery period of a few minutes to establish equilibrium before it can provide another step change in power output. Hence, it is rather important to include such limitations in the models of the power sources while the inverter control algorithms are being developed.

Such limitations in instantaneous power output capability of various sources indicate that some form of storage is necessary at the ac or dc bus to cope with instantaneous changes in power demand as required by sensitive loads. Without any storage, these systems will be incapable of meeting load requirements and may worsen the situation.

Hence, the generic model illustrated in Figure 3 is used to study the operation of a variety of DG devices. Using this model, the limitations of the power source can be programmed through appropriate limits on the current source, and the storage battery can be chosen to represent the virtual inertia of the system as desired. The inverter and the dc link represent the power electronic interface common to various DG devices. The dc and ac voltages and currents will be actual values to ensure correct parasitic in the test bed.

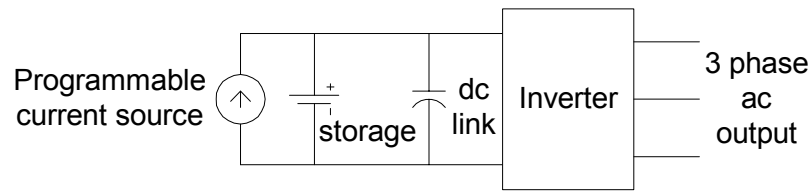


Figure 3: Block diagram of proposed model system

1.7 Hardware Test Bed

A hardware test bed is being developed to implement the control strategies and verify the operation of the proposed concepts. Experimental results from the test bed will be used further to refine the control algorithms and iterate on the best possible approach to realize the performance objectives.

A conceptual one-line schematic of the hardware test bed is illustrated in Figure 4. The system has been designed to provide the maximum amount of flexibility and variety of loads to study the operation of the systems under various operating scenarios.

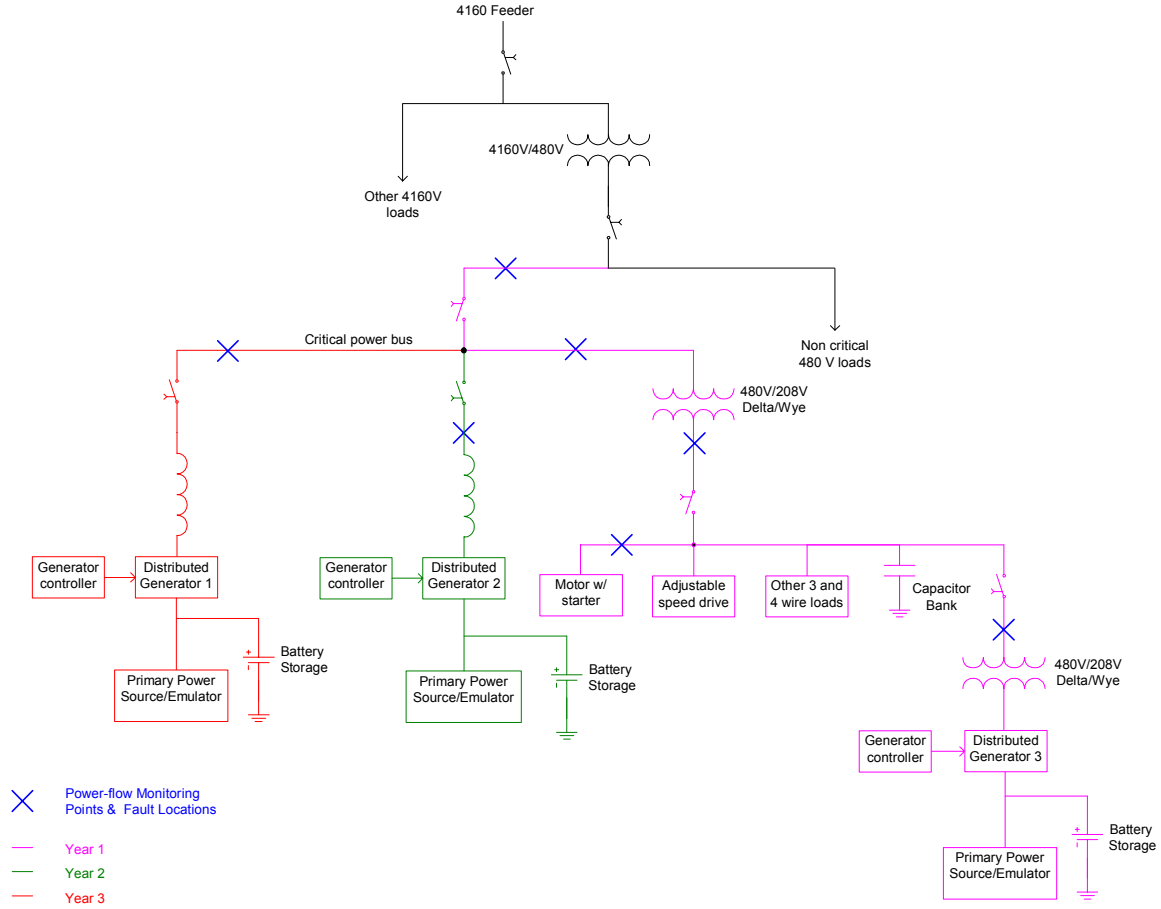


Figure 4: One-line conceptual schematic of the experimental test bed

The test bed is being commissioned in various phases over the period of the project. In its complete version, the experimental system features (a) a directly interfaced DG system, (b) a transformer coupled DG system, (c) the possibility of island operation, (d) the possibility of satellite operation, (e) induction motor loads, (f) adjustable speed drive loads, (g) four wire systems, (h) single phase loads and (i) ac side capacitor banks.

The components and the interconnection infrastructure necessary for the experimental test bed are located at the ECE department's power lab at the University of Wisconsin - Madison. The laboratory infrastructure has been upgraded to facilitate such flexible interconnections in a systematic and safe manner.

A prototype prime power source/emulator has been developed using a programmable dc power source feeding the dc bus of the DG system to emulate the properties of the primary power source, which may be a fuel cell system, a micro-turbine system or a photovoltaic system.

The emulator is fed from the dc power system in the lab equipped with a current regulated switched mode power supply. The emulator settings can be adjusted such that the input power ramp rate can be limited to match the dynamics of the DG system being studied. This strategy of using a power source emulator to provide the primary power source to the dc bus of the inverter rests on the architectural similarity of most DG devices. The dc buses of the inverters essentially decouple the dynamics of the primary power source, except to limit the instantaneous changes in power demand. It also ensures that the strategies that are being developed will be equally applicable to different types of primary power sources.

1.8 Report Organization

In Chapter 2 of the report, issues related to energy storage requirements of MSDG systems are identified. The results from this chapter are used to develop a battery selection strategy for providing energy storage, found in Chapter 3. The performance of the system is studied using battery models and simulations and is presented in Chapter 4. In Chapter 5, models of micro-turbine-based MSDG systems to obtain the dynamic properties of the dc link are developed.

The hardware platform uses low-cost, off-the-shelf inverters intended for motor drive systems to realize the inverter systems in MSDG. The modifications necessary to realize the same and testing of the inverter are discussed in Chapter 6. In Chapter 7, test and simulation results of the performance of an island mode inverter system feeding a complex set of loads in the hardware test bed are presented.

An outline of future work and a summary of the work completed is shown in the concluding chapter.

2 Energy Storage in Distributed Generation

2.1 Introduction

In the recent past, dramatic improvements in productivity have been realized in the high technology sector as well as in the traditional industries. For the electric power supply to these industries, this has led to a concomitant increase in the number of loads that are sensitive to power quality. Some of the industries that have such large sensitive loads include semiconductor manufacturing, textile mills, paper mills and plastic injection molding. Of course, a number of smaller but equally critical loads such as computers and electronic data processing equipment are also sensitive to power quality. The tolerance levels of computer equipment are specified by the Information Technology Industry/Computer and Business Equipment Manufacturers' Association (ITI/CBEMA) curves[1]. Figure 5 illustrates the CBEMA curves. This figure gives the percent of nominal voltage versus duration in (60-Hz) cycles. The CBEMA curves represent the boundary of the ac input voltage envelope that can be tolerated (typically) by most computer-based equipment. The upper curve represents the maximum voltage below which the equipment will continue to function normally. The lower curve is the minimum voltage above which the equipment will continue to function normally.

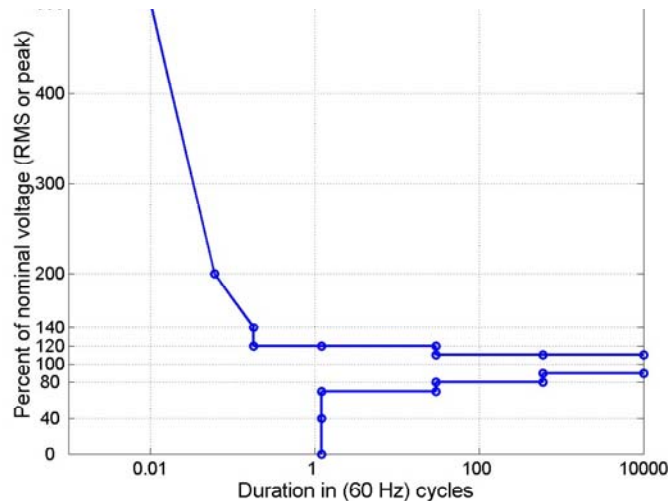


Figure 5: CBEMA curves specifying acceptable voltage sensitivity levels

As seen in Figure 5, the steady state range of tolerance for computer equipment is $\pm 10\%$ from the nominal voltage, i.e., the equipment continues to operate normally when sourced by any voltages in this range for an indefinite period of time. Similarly, voltage swells to a magnitude of 120% of the nominal value can be tolerated for about 0.5 s or 30 cycles; voltage sags to 80% of nominal for 10 s, or 600 cycles, can be tolerated [1,2]. When the supply voltage is outside the boundaries of the susceptibility curves, improvement of the

quality of power supplied to sensitive loads is essential to avoid a possible failure in their operation.

The traditional approach to obtaining a high quality power for sensitive loads involves the use of uninterruptible power supply (UPS) systems for conditioning the input voltage. A UPS consists of a rectifier, a battery system and an inverter. The batteries supply backup power during momentary interruptions or severe voltage sags. However, the problems in battery management at high power levels and high capital costs, while providing minimal use under normal operating conditions, are some of its drawbacks. These systems also contain transfer switches whose operation is critical to providing continuous power to loads.

Back-up generation systems based on rotating machines can be used as an alternative to UPS to power the sensitive loads during temporary interruptions in power supply. But they have a slower response time and require automatic transfer switches for a change over between power sources in case of power quality events. During the transfer between the main supply and backup, there may be a loss of continuity of power to the load, and hence, these systems are unable to meet the requirements of reliability. Moreover, they cause air pollution and may not be used more than a limited number of hours per year because of limits on exhaust emissions. This will result in suboptimal use of the capital investment made on them.

More recently, electrical generation systems based on small generators are gaining popularity. They may be classified as micro-source distributed generation (MSDG) systems [3]. These consist of small-rated micro-sources such as micro-turbines or fuel cells and power electronic converters to interface with the load. The block diagram of a micro-turbine-based MSDG system is shown in Figure 6. It contains a high-speed turbine, an ac generator, an ac/dc rectifier with optional battery and a three-phase dc/ac inverter. The power electronics equipment in them makes it possible to provide UPS functionality, power quality improvement and energy conversion simultaneously at a reasonable cost.

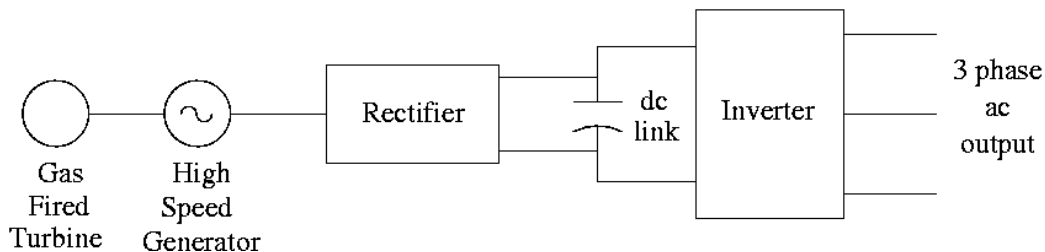


Figure 6: Block diagram of a micro-turbine-based distributed generation system

In the grid-connected mode of operation, an MSDG system can be connected to sensitive loads alongside their main supply. Another possible operating mode involves direct connection of MSDG systems to the load, also known as island mode of operation. Use

of MSDG systems in grid-connected mode improves the reliability of power distribution because they can be located close to the sensitive loads. During interruption in the main power supply, they need to be operated in island mode. However, MSDG systems are characterized by low inertia in contrast to conventional high-rated generation systems such as synchronous and induction generators. In contrast, conventional generation systems contain large rotating masses in which energy is stored in the form of inertia. Under load and supply transients, the inertia of the system delivers or absorbs any power mismatch between generation and demand. Because MSDG systems have low inertia, they do not have sufficient energy storage capacity to meet the demands of loads in the event of transients. Thus, to provide continuous power to sensitive loads during abrupt changes in load power demand, it is necessary to install auxiliary energy storage in them. If not, operation of the MSDG system may deteriorate in the island mode of operation.

Transient changes in load power demand may result from faults in transmission line or load switching. For instance, a 75-kW Honeywell micro-turbine took about 35 s to respond for a 50% change in power demand under the grid-connected mode of operation [4]. On the other hand, some fuel cells require about 10 s for a 15% change in power output [5]. Furthermore, a fuel cell also has a recovery period of a few minutes to establish equilibrium before it can meet another step change in power output. The typical response that can be expected of a micro-turbine for a step change in load demand is illustrated in Figure 7. In the figure, P_L denotes the load power demand, P_S is the response of the micro-turbine, and $(P_L - P_S)$ is the shortage in power that needs to be supplied through some means. In the grid-connected mode of operation, the grid supplies the shortage in power until the micro-source responds to a step change in power demand. However, in the island mode of operation, this sudden demand can be met only if additional storage is included in the MSDG system.

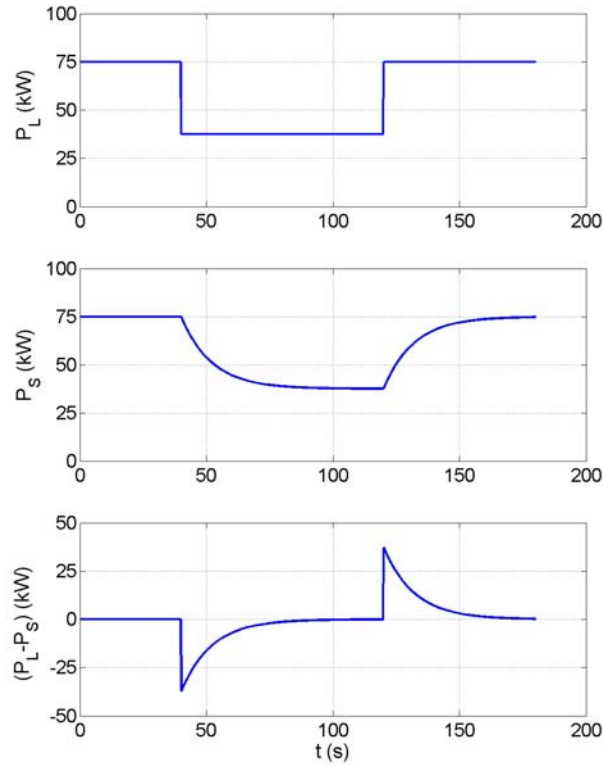


Figure 7: Typical step response of a micro-turbine
 P_L - load power demand, P_S - response of the micro-turbine

Furthermore, the addition of storage in an MSDG system can be used for energy stabilization, ride-through and dispatchability [6]. Energy stabilization and ride-through are achieved by the use of storage to provide a stable supply of power in the event of failure of the micro-source or transient changes in load power. And dispatchability is possible when the MSDG system with storage is controlled such that it supplies a particular percentage of the load demand as compared with the main supply.

Energy storage can be provided in an MSDG system through several means, such as batteries, super-conducting magnetic energy storage (SMES), flywheels and ultra-capacitors. Among these, the technology of batteries is the most developed and is well established for a variety of applications. The other forms of energy storage are either still in the prototype stage of development or are not suitable for mass production.

In Chapters 3 and 4, battery storage is studied in detail for meeting the storage requirements of the MSDG system. Because an MSDG system is basically composed of a micro-source and a three-phase dc/ac inverter, its dc link is the most appropriate location for installing storage. Thus, battery storage in the dc link of the MSDG system is used to meet the power requirements during abrupt changes in power demand from the load. However, the analysis conducted in this report can also be applied to other energy storage devices with appropriate modifications.

In this chapter, the energy storage requirements in MSDG systems for typical load scenarios have been investigated. Chapter 3 consists of the battery design issues and provides guidelines on sizing of battery storage for a given MSDG system. In Chapter 4, the MSDG system with battery storage is modeled. The results of simulation of the power supply/demand of the model are presented.

3 Battery Design Issues

This chapter describes a technical approach for the selection of suitable batteries for MSDG systems. The current state of the art in battery technology for MSDG applications is also briefly discussed. The characteristics of a lead-acid battery for successfully meeting the transient demands of loads in an MSDG system are then described.

This chapter gives a strategy for appropriately oversizing the battery capacity to ensure that it is adequate to meet the demands of the MSDG system. Commonly used battery parameters are introduced, and the mathematical expressions relating the parameters are derived. A design procedure is described in the form of a flowchart for sizing these batteries. The main criterion to be satisfied by the battery is to meet any change in load power demand until the micro-source responds to follow it. Provisions can also be made for including UPS functional capability in the MSDG system, i.e., operation of the system for extended periods without any power delivered from the micro-source.

3.1 Technical Approach

Electrical loads, in general, draw real and reactive power from the MSDG system. The interface between an MSDG system and the load/utility is typically a three-phase dc/ac inverter [3]. The use of a three-phase inverter allows dynamic control of voltage and real and reactive power supplied to the load. The three-phase inverter is capable of supplying reactive power to the ac system without energy storage elements. Only a capacitor on its dc bus is adequate for the purpose of reactive power compensation. This is because reactive current circulates among the three phases of an inverter and is not drawn from its dc side [7]. So any changes in reactive power demand of the loads will not affect battery sizing in the MSDG system. However, only real power demand of the load is drawn from the dc bus of the inverter, and a step change in real power will determine the sizing of battery storage. Thus, in general, references to power in this report deal with real power unless stated explicitly.

The block schematic of a general battery-based MSDG system is given in Figure 8, in two possible configurations, (a) and (b). Figure 8(a) represents an unregulated dc bus configuration, and 8(b) represents a regulated dc bus configuration.

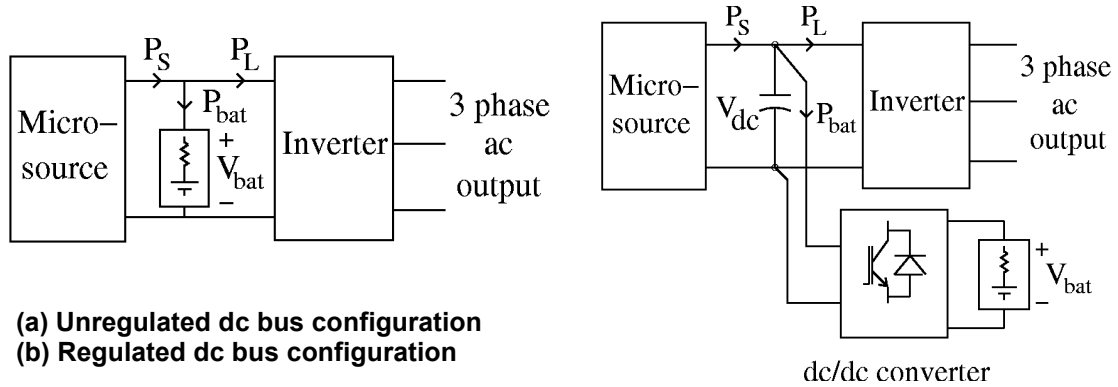


Figure 8: Block diagram of an MSDG system with battery storage

The battery is represented in the figures as an ideal voltage source in series with an internal resistance. V_{bat} is the terminal voltage of the battery, and P_S , P_L and P_{bat} are the micro-source power, load power demand and battery power, respectively.

In the unregulated dc bus configuration, the battery is connected directly to the dc bus, and the state of the battery during the charging and discharging cycles dictates the dc bus voltage. Because the power flow in and out of the battery is for a very short duration, it requires a battery with the ability to discharge to final voltage and recharge to 100% state of charge within a short interval of time.

In the regulated dc bus configuration, the dc bus contains a capacitor whose voltage is regulated and is independent of the battery charging and discharging cycles. A dc/dc converter is used as the interface between the battery and the dc bus capacitor. By controlling the switching scheme of either the rectifier (at the micro-source end), the inverter or the dc/dc converter, the dc bus voltage can be regulated.

The dc/dc converter in the regulated dc bus configuration may be used to step down (buck) or step up (boost) the voltage at the terminal of the battery. A battery consists of several cells stacked in series, where a cell is its basic unit. It is generally beneficial to have less current drawn from the battery, as this will maintain the instantaneous power drawn from each cell to a minimum. Therefore, it may be desirable to have a battery on the higher voltage side of the dc/dc converter. But the choice of too large a battery voltage would require a large number of series-connected cells resulting in charge equalization problems.

The MSDG system is a utility application of batteries. The currently available rechargeable batteries include lead-acid, nickel cadmium (NiCd), nickel metal hydride (NiMH) and Lithium (Li-ion). NiCd and NiMH are not preferred in utility applications because they have very high self-discharge rates. Although Li-ion has the highest energy density, it is also the most expensive. The cost per kWh of a lead-acid battery is the least expensive among these, and it can meet the power density requirements of MSDG applications. For these reasons, a lead-acid battery is considered the most suitable for MSDG applications for further study in this report.

Lead-acid batteries can be designed for deep-cycle or starting applications. Deep-cycle batteries are used in back-up power applications in which power is needed for longer durations. These batteries are typically applied in electric vehicles and UPS systems. Starting batteries are commonly used to start internal combustion engines. No power is drawn from these batteries during the normal operation of the engines. They are capable of providing large currents for a very short interval of time. Hence, starting batteries of higher capacity are suitable for MSDG applications.

Battery sizing is dependent on the number of cells it contains and the capacity of each cell. The cell capacity is normally measured in ampere-hours, denoted here as Ah. A

method of specifying charge and discharge rates of a cell is the C rate, which is defined as the current flow rate that is numerically equal to the cell rated capacity [8]. For example, the C rate of a 1-Ah capacity cell is 1 ampere. Both charge and discharge rates are normally represented as multiples of the C rate. A current that would nominally discharge the battery in 1 hour is represented as 1 C. A current that would nominally discharge the battery in 10 hours is specified as 0.1 C. Similarly, a current that would nominally discharge the battery in a short interval of 6 minutes would be represented as 10 C. The short duration discharge typically at 3 C or higher is termed as a high-rate discharge.

Lead-acid batteries are usually rated at 8-, 10-, or 20-hour rates. For example, the Absolyte IIP series of valve regulated lead-acid (VRLA) batteries are rated on an 8-hour rate, with capacities ranging from 105 Ah to 4,800 Ah [9], and the NP series is rated on a 20-hour rate with capacities ranging from 1.2 Ah to 65 Ah [10]. For a battery, the MSDG system is a high-rate discharge application. The maximum discharge in MSDG applications involving micro-turbines typically occurs in 100 s, and therefore, the discharge rate of these applications is about 36 C. Battery parameters need to be derated at high discharge rates because of increased losses under these conditions. Table I gives the nominal capacity of lead-acid batteries at different rates of discharge. From the table, we observe that a battery rated on a 10-hour rate has only 44% deliverable capacity if the discharge is conducted in 0.2 hours (i.e., 12 minutes).

Table 1: Typical capacity variation at different discharge rates [8]

Discharge Time (Hours)	Discharge Current (Multiple of C)	Actual Capacity (%)
0.2	50	44
1.0	10	72
5.0	2	92
10.0	1	100
20.0	$\frac{1}{2}$	108

Loss of capacity at high discharge rates may also be graphically represented, as is more common among battery manufacturers' data sheets. Figure 9 shows the cell discharge voltage as a function of discharge rate.

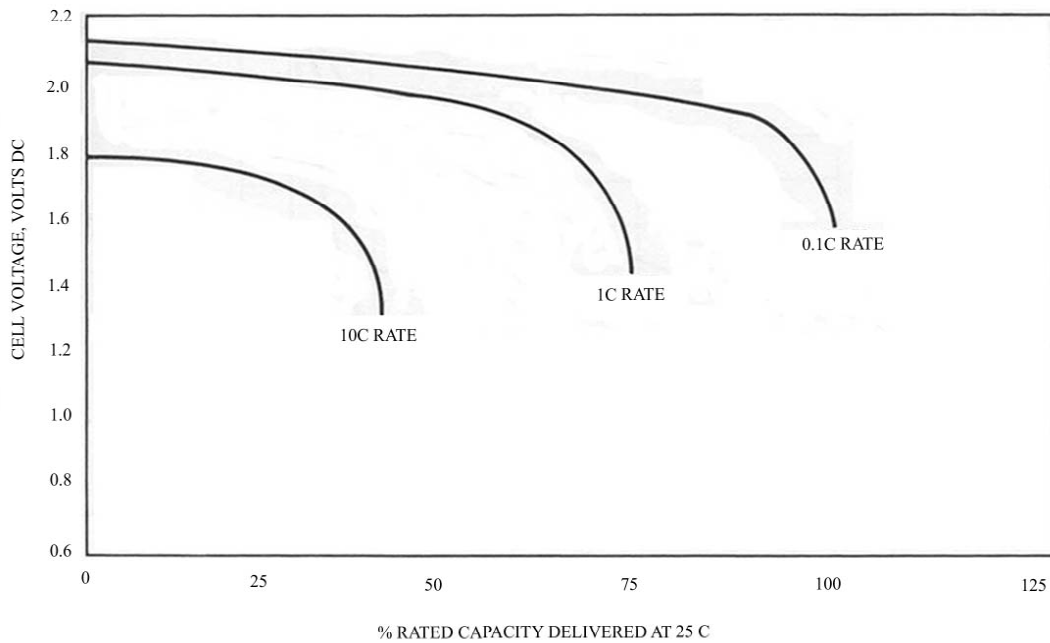


Figure 9: Cell discharge voltage versus time for a lead-acid battery [8]

Most battery manufacturers' data sheets provide tables containing dc amperes that the battery can source at different final volts per cell and for different periods of time. These tables incorporate the derating necessary for high-rate discharge applications for values at lower time intervals. It may be noted that all battery ratings are for a nominal room temperature of 25°C or 77°F, and additional derating will be necessary for lower temperatures.

In addition to the loss of energy storage capacity, the terminal voltage of the battery is also strongly affected by the discharge rate. Figure 10 illustrates the battery current and the corresponding terminal voltage for two sizes of cell, 'X' and 'D', at two temperatures. In the figure, battery 'X' is rated at 3.2 Ah and 'D' at 1.8 Ah.

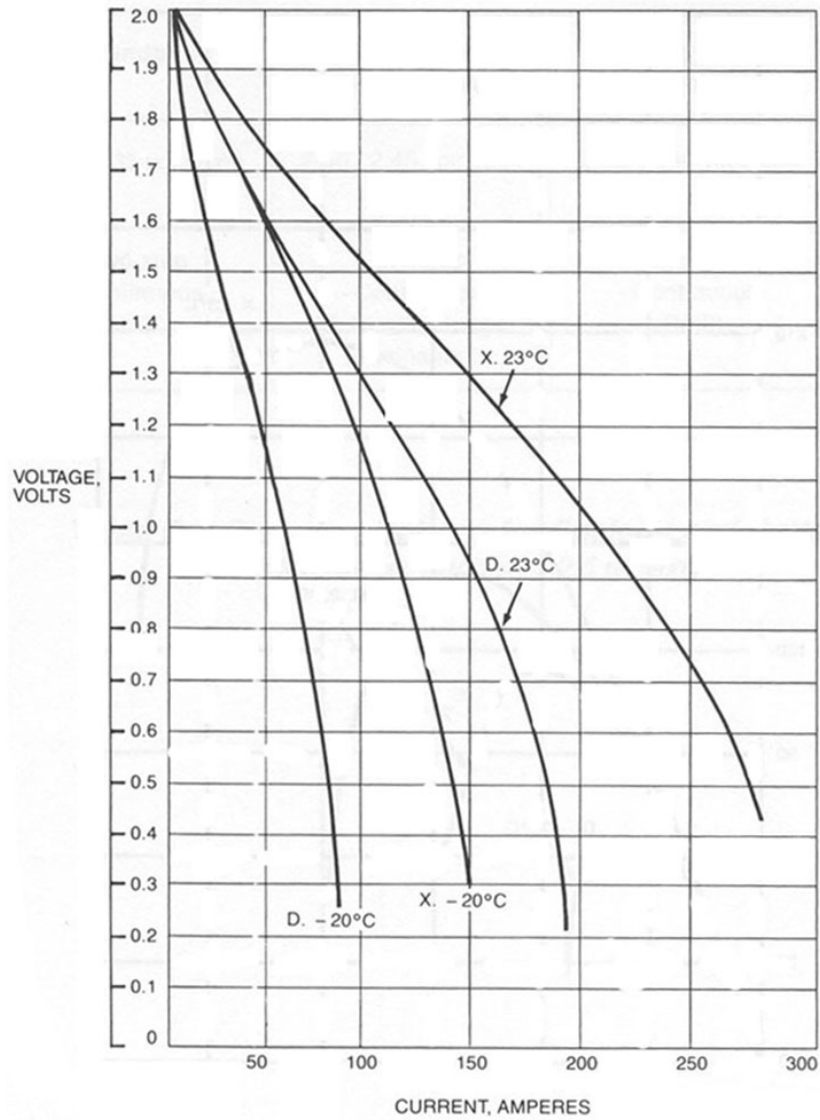


Figure 10: Peak current and voltage per cell of a lead-acid battery for a high-rate discharge [8]

A Thevenin's equivalent circuit (Figure 11) of the battery supplying power to a load can be drawn from the data represented in Figure 10. The negative slope of the curves in Figure 10 gives the Thevenin resistance (R_{th}) of the battery. Using the maximum power transfer theorem, we can deduce that, when the load equivalent resistance equals R_{th} , maximum instantaneous power gets transmitted. Because R_{th} corresponds to the battery's internal resistance, we observe that at this operating point, losses in the battery internal resistance are equal to the power transferred to load. Hence, at the maximum power transfer operating point, the power dissipated in the battery would be enormous. To avoid losses in the battery and subsequent deterioration in its operation, it is necessary for us to select a battery whose internal resistance is very small compared with the equivalent resistance of the load during the transient.

The variation of output power delivered by the batteries as a function of current drawn for 'X' and 'D' is shown in Figure 12. From the figure, it is clearly evident that the battery has a limit on the maximum instantaneous power that it can support, which is dependent on factors such as temperature and capacity.

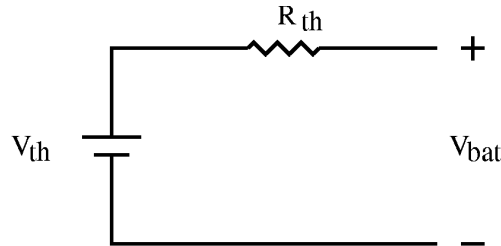


Figure 11: Thevenin equivalent circuit of the battery

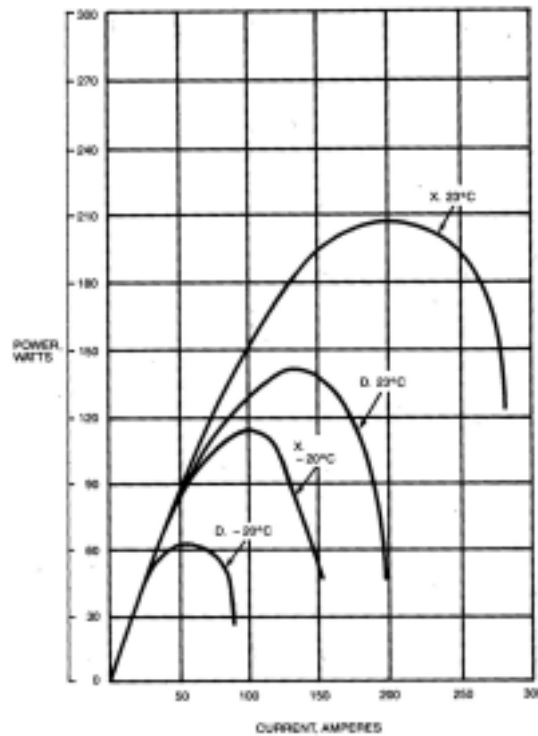


Figure 12: Instantaneous power curves of a lead-acid battery for a high-rate discharge [8]

In an MSDG system, the battery is also subjected to high-rate charging. This occurs when the load is suddenly removed and the micro-source continues to supply power until it is able to respond to the new power set point. The battery has to be capable of accepting this difference in power for a short duration. Thus, it must have a high charge acceptance.

Similar battery demands occur in their application in hybrid electric vehicles (HEVs). In this application, batteries are primarily used during starting, accelerating and braking of the vehicle, and no net power is drawn from the battery in normal running mode of the vehicle. Therefore, desirable attributes of high-power batteries for HEV applications are high-peak power handling capability during starting and acceleration and high charge acceptance to maximize regenerative braking utilization. The basic requirements for a power buffering battery in a HEV are defined by the Partnership for a New Generation of Vehicles (PNGV) work group as shown in Table 2 [11].

Table 2: PNGV charge sustaining HEV, battery specification [11]

Description	Requirement (Slow Response Engine)
Energy Cycle Efficiency	90 – 95 %
Power Processing	+65 – +80 kW (18 s) -70 – -150 kW (10 s)
Voltage Variation	+/- 15% from nominal
Battery System Mass	< 65 kg (> 1,000 W/kg)
Temperature Range	-40 °C – 52 °C
Minimum Energy Storage	> 0.54 MJ (150 Wh)

Various research activities continue to be conducted for meeting these requirements by optimal control of battery state using battery management systems [12]. In the near term, the general solution for most recently developed HEVs has been to oversize the battery capacity.

In summary, battery sizing for an MSDG system depends on the magnitude and duration of the mismatch between the real power demand of the load and the power delivered by the micro-source. Because power drawn from the battery is for a short duration in this application, lead-acid batteries of high-rate discharge and charge-acceptance capability are suitable. The main property of batteries for high-discharge applications is their peak power capability, which in itself is a strong function of its capacity and internal resistance. The construction of these batteries is optimized for peak power, i.e., high capacity along with ultra-low internal resistance. The batteries must also have a good charge acceptance to accommodate the high-rate charging upon removal of load. Most state-of-the-art batteries are hard pressed to meet these stringent requirements. Hence, the overcapacity of cells through parallel connection reduces the equivalent internal resistance, thereby allowing them to be applied appropriately for MSDG applications.

3.2 Battery Bank Design Strategy

Design considerations of batteries for a typical MSDG system begin with characterization of the cell, which is the basic unit of a battery. Cells are specified with a nominal cell voltage (V_{cn}). It is equal to the open-circuit voltage of a cell at 100% state of charge and is the recommended float voltage of the cell. The cell voltage at the completion of discharge is denoted by final volts per cell (FVpC). As was observed in Figures 9 and 10, maintaining FVpC at or above 1.5 V will generally maintain the operating conditions in the linear range of the instantaneous power curve at a temperature of 23°C. However, battery losses will be high for such low FVpC values because the instantaneous power curves begin to approach their maximum. Hence, FVpC of the battery should be selected as high as possible, at the expense of overcapacity. It may be selected within the 80% to 90% range of V_{cn} .

$$FVpC = 0.8 V_{cn} \quad (1)$$

For a high-rate discharge application, typical FVpCs specified in the battery manufacturers' data sheets are 1.75 V, 1.78 V and 1.81 V. The nearest value available in the data sheets to that calculated from (1) may be selected as FVpC.

Let V_{batf} represent the terminal voltage of the battery (consisting of a series string of N_c cells) after discharge. Then, the number of cells is given by:

$$N_c = \frac{V_{batf}}{FVpC} \quad (2)$$

If N_c is not an integer, the next higher integer is chosen. For a battery connection in unregulated dc bus configuration, V_{batf} is equal to the minimum dc bus voltage of the inverter. Besides, the inverter dc bus voltage is in turn dependent on its ac voltage constraints. Likewise, in the regulated dc bus configuration, V_{batf} is decided by the dc/dc converter switching scheme.

The battery must be designed to provide power for a brief period, during a change in load demand. If the maximum change in real power demand of the load is known beforehand, it is possible to select a battery. It may be assumed that this condition occurs when switching from the no-load to the full-load. This has been found to be true in practical test results on micro-turbine generators [4]. The ramping period is the highest for load change from no-load condition to full-load condition for a 75-kW Honeywell generator and a 28-kW Capstone generator. If $P_{b, \max}(t)$ is the maximum power drawn from the battery in $T_{r, \max}$ seconds, it is dependent on the full-load power (P_{fl}) as follows:

$$P_{b, \max}(t) = P_{fl} g(t) \quad (3)$$

where $g(t)$ is an increasing function beginning at zero and reaches a peak value of unity at a time $T_{r, \max}$. The function $g(t)$ is dependent on the type of response of the micro-source. Typically, $g(t)$ may describe an exponential function or a ramp function.

The maximum energy storage required in the battery ($E_{b, \max}$) may be determined by:

$$E_{b, \max} = \int_0^{T_{r, \max}} P_{b, \max}(t) dt \quad (4)$$

The integral can be evaluated as:

$$E_{b, \max} = \kappa P_{fl} T_{r, \max} \quad (5)$$

where:

$$\kappa = \int_0^{T_{r, \max}} g(t) dt \quad (6)$$

The value of κ is evaluated to be 0.5 and 0.2 when $g(t)$ is a ramp function and an exponential function, respectively.

The full-load power (P_{fl}) can be obtained as:

$$P_{fl} = \frac{kVA_{fl} pf \times 10^5}{\eta} \quad (7)$$

where kVA_{fl} is the full-load kVA of the inverter, pf is the power factor of the load connected to the inverter and η is the inverter efficiency in percent.

Combining the Equations 5 and 7:

$$E_{b, \max} = \frac{\kappa kVA_{fl} pf T_{r, \max} \times 10^5}{\eta} \quad (8)$$

An expression for the ampere-hour per cell (Ah) of the battery in terms of FVpC and N_c is given by:

$$Ah = \frac{E_{b, \max}}{N_c FVpC \times 3600} \quad (9)$$

Substituting Equation 8 into Equation 9:

$$Ah = \frac{\kappa kVA_{fl} pf T_{r, \max} \times 10^5}{N_c FVpC \eta \times 3600} \quad (10)$$

The C rate of the battery is numerically equal to the Ah value obtained above. The discharge rate of the battery is specified in multiples of C rate. If d is the multiplier that determines the discharge rate of the battery, then:

$$d = \frac{3600}{T_{r, \max}} \quad (11)$$

and the discharge rate of the battery may be expressed as dC .

The dc amperes drawn from each cell of the battery is the amperes per cell (ApC). It is obtained as:

$$\text{ApC} = d \text{ Ah} \quad (12)$$

for a duration of $T_{r, \max}$. It is to be noted that ApC is the average current drawn from the battery during discharge. In a high-rate discharge application, peak current may be one order of magnitude higher than ApC.

A micro-turbine has a start-up time to reach full-load power from its cold start. For example, the start-up time for the 28-kW Capstone Micro-Turbine is approximately 2 minutes [12]. If it is desired to accommodate a cold start of the micro-turbine, the expression for $E_{b, \max}$ in Equation 5 has to be modified to include the power drawn by the battery during start-up. The modified equation will be:

$$E_{b, \max} = \kappa P_{fl} T_{r, \max} + P_{cs} T_{cs} \quad (13)$$

where P_{cs} is the power drawn (in watts) during a cold start of the micro-turbine for a period of T_{cs} seconds. And the subsequent equations can be reformulated.

These design guidelines for sizing batteries are given in Figure 13 in the form of a flow chart. The flow chart also includes the modifications necessary to rate the batteries to provide UPS functionality. If UPS functionality is also desired in an MSDG system, a battery that can provide a high-rate discharge current for the response time of the micro-source as well as a low-rate discharge current for UPS operation is required.

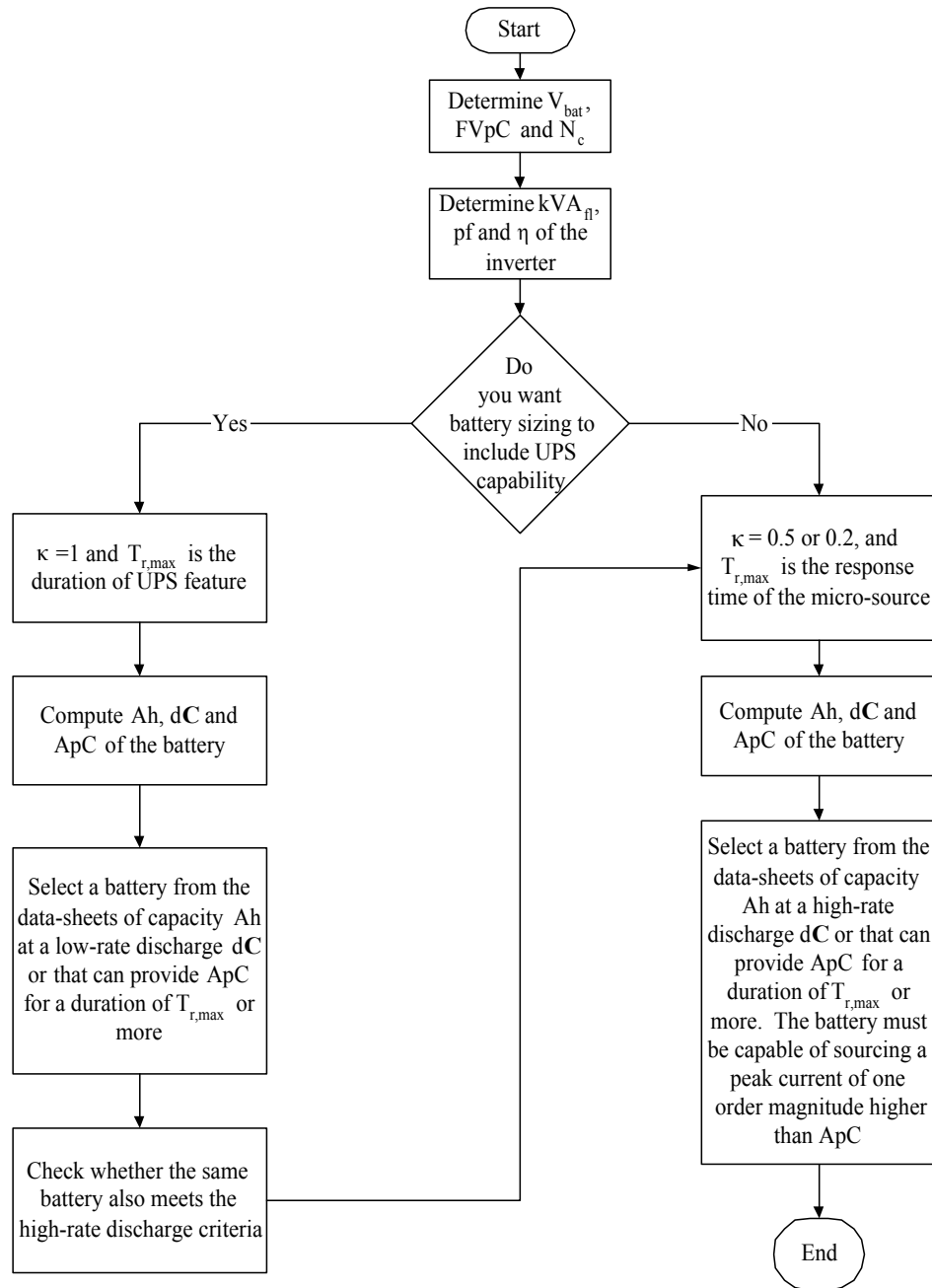


Figure 13: A flowchart describing the design approach

4 Battery Modeling and Simulation

In this chapter, a simplified model of the MSDG system along with battery storage is developed. The micro-source power supply and load power demand are modeled by mathematical functions to represent a typical micro-source and load. The battery is modeled by a simplified equivalent circuit whose elements are dependent on its design parameters.

Also in this chapter, the design procedure given in Chapter 3 is used to obtain the required capacity of battery storage and the required number of cells for a typical MSDG system. Then the system model parameters are determined from the design variables. A digital computer simulation of the system model is performed by MATLAB/Simulink™ software.

4.1 Modeling Approach

To model a micro-source, results of tests conducted by Southern California Edison on micro-turbine generators (MTGs) [4] were used. The test results on 75-kW Honeywell MTGs and 28-kW Capstone MTGs for step changes in load are reproduced from [4] in Tables 3 and 4, respectively. Portions of these results are plotted and curve-fitted in Figures 14(a) and 14(b) for Honeywell and Capstone MTGs respectively.

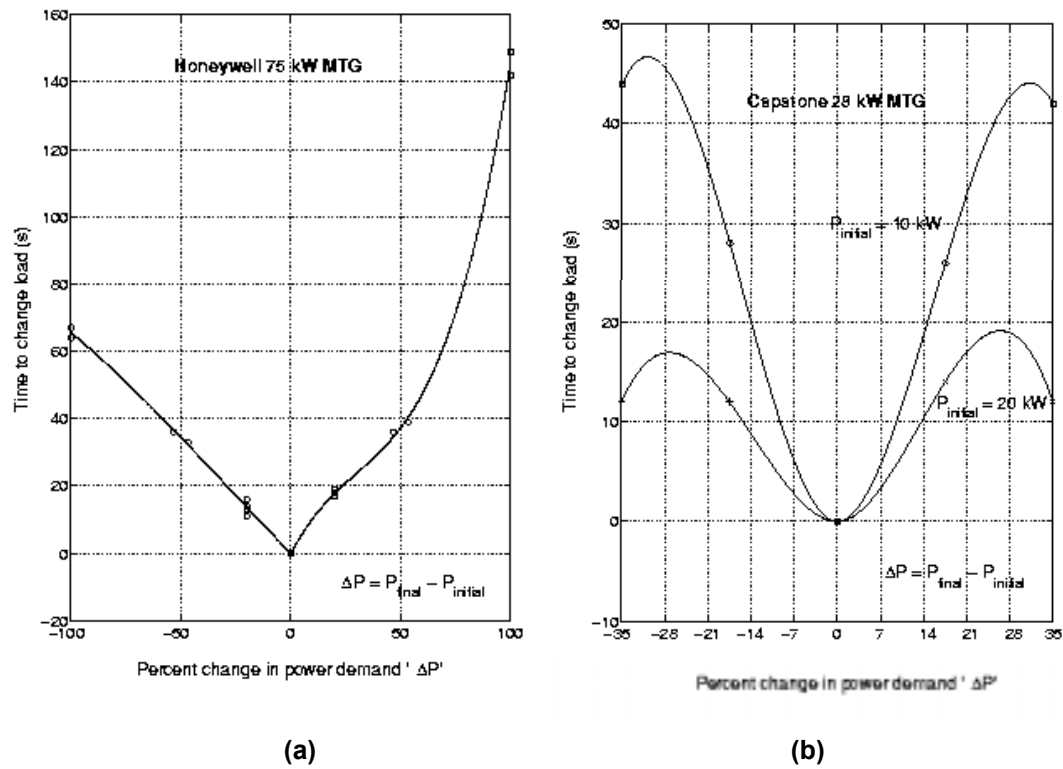


Figure 14: MTG response for step change in load

The plots give the variation of time of response of the turbine as a function of percent change in power demand. It should be noted that the results reported in [4] are for MTGs in grid-connected mode only and that battery storage is not critical in this case because the grid responds faster to any step changes in load demand. And in the island mode, battery storage becomes critical for meeting the transient power demands of the load.

From the Honeywell MTG characteristics illustrated in Figure 14(a), it may be observed that response time is almost proportional to the change in the power demand (ΔP) of the load. In addition, it may be seen that the MTG responds at a different rate for positive ΔP than for a negative ΔP . The response time is same for a fixed ΔP , independent of the initial power level of the MTG.

On the other hand, the Capstone MTG graph displayed in Figure 14(b) shows different response curves as compared with the Honeywell MTG. The Capstone turbine's time of response, unlike that of Honeywell, is not proportional to ΔP and is dependent on the initial operating power level of the MTG. It may be because these MTGs make use of different control schemes or hardware configurations.

For the purpose of study on battery storage, an MTG that responds for step changes in load power similar to the Honeywell MTG is considered. The digital simulation of the DG system is conducted using MATLAB Simulink™ software. A simple mathematical model of the MTG and the load is devised for the simulation. The load power demand is simulated using a step function, and the MTG response is simulated as an exponential/ramp function of time.

Several models of lead-acid batteries are available in literature. A simplified model is used herein, whose equivalent circuit is shown in Figure 15 [14]. This model gives a good representation of the self-discharge, storage capacity and internal resistance.

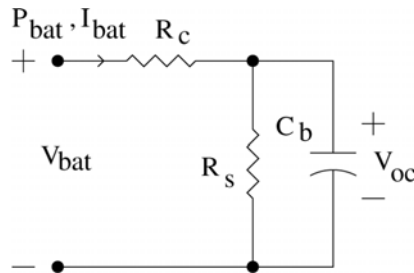


Figure 15: Equivalent circuit of a lead-acid battery

P_{bat} , V_{bat} and I_{bat} denote the power, voltage and current of the battery. Battery open-circuit voltage (V_{oc}) is a function of the average specific gravity and temperature of the sulfuric acid electrolyte in the cell. Battery equivalent capacitance (C_b) is estimated from the maximum energy that it has to supply. Energy capacity (in J) of a battery is defined as:

$$E_{\text{bat}} = \frac{C_b V_{\text{oc}}^2}{2} \quad (14)$$

Also:

$$E_{\text{bat}} = V_{\text{oc}} \text{ Ah} \times 3600 \quad (15)$$

Solving Equations 14 and 15, an expression for battery equivalent capacitance C_b may be obtained as:

$$C_b = \frac{2 \text{ Ah} \times 3600}{V_{\text{oc}}} \quad (16)$$

The series charging/discharging resistance (R_c) is the effective internal resistance that can be obtained from the battery manufacturers' data sheets. R_c includes the effects of the resistivity of the plate grids, the lead posts, the terminals and the interface contact resistance between these parts of the battery. The self-discharging resistance (R_s) is a function of its self-discharge characteristics. It can be obtained from the battery manufacturers' data sheets.

Thus, a simplified model of the MSDG system along with battery storage was developed. Although a micro-turbine represented the micro-source here, techniques developed here may be used to model other micro-sources, too. The battery is modeled by an equivalent circuit whose quantities depend on the battery design parameters.

4.2 Simulation Results

As a case study, battery storage is designed for an MSDG system whose specifications are as follows:

$$V_{\text{batf}} = 450 \text{ V}$$

$$\text{kVA}_{\text{fl}} = 60 \text{ kVA}$$

$$\text{pf} = 1.0$$

$$\eta = 80\%$$

$$T_{r, \text{max}} = 150 \text{ s}$$

$$k = 0.2$$

(Assuming an exponential response of the micro-source to a step change in power demand,) UPS and cold start functionality is not included in the MSDG system here. Various design variables are computed as follows:

From the data sheets, cell nominal voltage is typically:

$$V_{\text{cn}} = 2.28 \text{ V}$$

Final volts per cell (FVpC) is calculated using Equation 1 as:

$$FVpC = 0.8 V_{cn} \approx 1.81 \text{ V}$$

Using Equation 2, the number of cells required for the battery will be:

$$N_c = \frac{V_{batf}}{FVpC} \approx 249$$

Battery self-discharging resistance (R_s) and internal resistance (R_c) are obtained from the data-sheets for N_c cells as:

$$R_c = 1.49 \Omega \text{ (for } N_c \text{ cells)}$$

$$R_s = 25 \Omega$$

For providing a full-load demand of 100 kW, ampere-hour per cell of the battery is computed using Equations 10 and 11 as:

$$Ah = \frac{k \text{ kVA}_{fl} \text{ pf } T_{r, \max} \times 10^5}{N_c FVpC \eta \times 3600} = 1.4$$

$$d = \frac{3600}{T_{r, \max}} = 24$$

The equivalent capacitance of the battery is determined using Equation 16 as:

$$C_b = \frac{2 Ah \times 3600}{V_{oc}} = 22.4 \text{ F}$$

where V_{oc} is the open-circuit voltage at the end of discharge and is equal to 450 V. The amperes per cell (ApC) of the battery is computed from Equation 12 to be:

$$ApC = d Ah = 33.6 \text{ A}$$

The parameters of the example case study described above were simulated using MATLAB/SimulinkTM. Figure 16 illustrates the results from the simulation. It gives the load power demand (P_L), power supplied by the micro-source (P_s), battery power (P_{bat}), battery current (I_{bat}) and battery terminal voltage (V_{bat}). The figure demonstrates battery response to a step change in load power demand under the following conditions: from full load to no load at $t = 20$ s and from no load to full load at $t = 200$ s. The amperes per cell (ApC) value computed above is the average current during discharge. It is observed that the peak battery current is about one order of magnitude higher than ApC. The terminal voltage (V_{bat}) waveform shows a sudden change at the instant of the high-rate charge and discharge. This is due to the internal resistance of the battery during a high-rate charge and discharge. A higher capacity battery would reduce the voltage ripple.

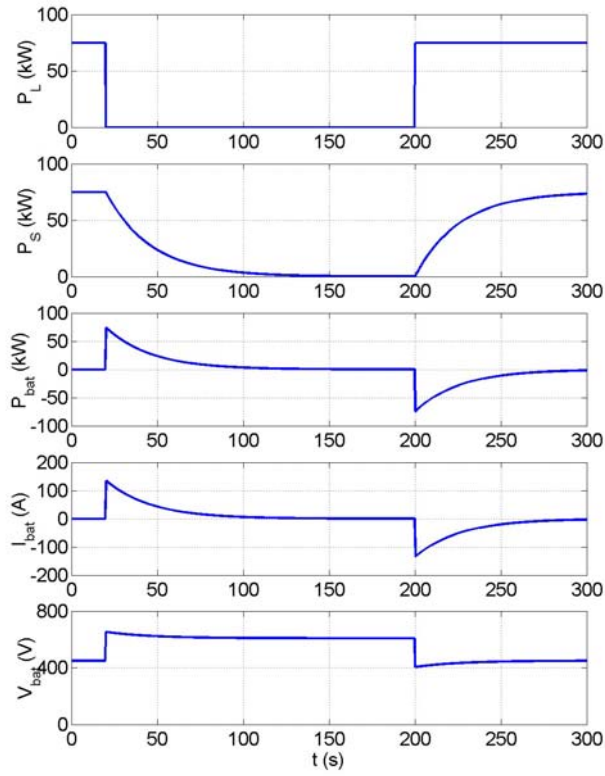


Figure 16: Step response of a battery-based MSDG system

An important assumption made in the simulation is that the values of the equivalent circuit parameters are not varying. In reality, these parameters are affected by temperature, state of charge, rate of discharge, etc. However, the results indicate the overall behavior of the battery system in a typical MSDG application. The battery models can be made more complicated to faithfully reproduce more complex behavior. However, for the purpose of studying the general behavior of the battery from a systems viewpoint, the present models are deemed adequate.

5 Micro-Turbine Modeling and Emulation

One of the preferred forms of next generation distributed generation options is the micro-turbine, supplied from a natural gas pipeline. These units are designed for continuous operation and represent a core technology for MSDG systems. The purpose of this section is to develop models for the micro-turbine generators for distributed power.

The manufacturers of these micro-turbines have spent a lot of money to investigate their physical implementation. This funding and research has driven the price of these units down to a competitive rate. However, the actual implementation of these micro-turbines has not been given the same attention. Issues such as the control and protection of these devices need to be addressed before their large-scale acceptance is seen. Specifically, the response of micro-turbines to load changes and their ability to effectively interact with one another in an island environment needs to be addressed.

It is therefore the goal of this section to investigate the response of micro-turbines to load changes under a variety of loading profiles. This understanding will lead to better control methodologies and protection schemes.

5.1 Turbine-Generator Basics

Regardless of the size of a micro-turbine, the same basic operating principle applies: convert one form of mechanical energy to electrical energy. However, the details behind this conversion vary greatly among the different types and sizes of turbines and generators, and therefore, the exact behavior for each type and size are different.

Because large steam turbines and large synchronous generators have dominated power generation, the steady state and dynamic behavior for these systems is well understood. The basic operation and control principles are summarized below.

- At steady state, the power of the steam rate into the turbine is equal to the electrical power removed from the generator. The speed of the generator and turbine is considered to be synchronous, implying that output electrical sinusoids are in phase with the grid. This operation requires good speed control of the turbine.
- During a load transient, the change in power is taken from the speed of the rotor of the large turbine and generator. Because these devices are enormous, there is considerable stored energy in the rotating masses. The speed control of the turbines sees this speed change and corrects the rate at which the steam is supplied to the turbine, correcting the speed until the set point is achieved. In this manner, the turbine generator set is capable of nearly instantaneous load tracking.

The same base of knowledge is not available for micro-turbines and generators. However, the same basic principles apply and are summarized below.

- At steady state, the power of the natural gas combustion and air into the turbine is equal to the electrical power removed from the generator. The speed of the generator and turbine is not critical, as the output sinusoids from the generator are rectified. The dc link voltage needs to be supported to ensure that conservation of power requirements are met. This operation requires good speed control of the turbine.
- During a load transient, the change in power is taken from the speed of the rotor of the micro-turbine. However, because these devices are small, there is very little stored energy in the rotating masses and the speed of the rotor changes very quickly. The speed control of the micro-turbines sees this speed change and corrects the rate at which the fuel is supplied to the micro-turbine, correcting the speed until the set point is achieved. The speed of micro-turbine needs to be changed quickly to ensure that the generator does not stall. In this manner, the turbine generator set is capable of load tracking.

Different control methodologies are investigated later in this section. First, a mathematical model is required to predict the steady state and dynamic behavior of a micro-turbine.

5.2 Micro-Turbine System Construction

The block diagram below shows the basic functional units of a micro-turbine.

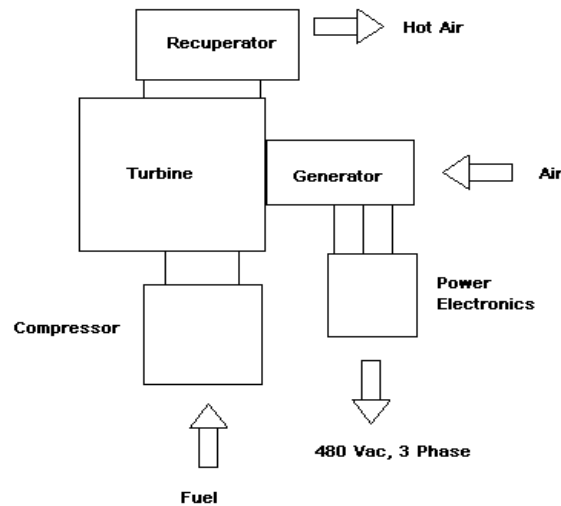


Figure 17: Micro-turbine block diagram

The largest difference between the micro-turbine and a conventional unit is that the combustion occurs at the unit. The recuperator increases the efficiency of the system by using the exhaust gas in the process.

From a modeling standpoint, this analysis will view the mechanical system, including the turbine, as a lumped moment of inertia, J . The mechanical system will control the torque applied to the generator. This will be discussed in detail in the next sections.

The generator is a permanent magnet type, which feeds a passive rectifier. The rectifier supports a dc link, which is the input to the voltage source inverter. The block diagram of the generator and power electronics is expanded in Figure 18.

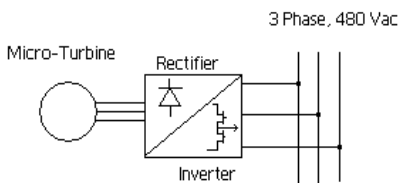


Figure 18: Block diagram of micro-turbine generator connection to utility/load

The rectifier and dc link above are shown in one of several possible configurations. The rectifier could be an active one, or there could be a chopper used to regulate the bus voltage. However, Figure 17 is the basic configuration used, and it is the one from which the mathematical models will be generated.

The inverter is a voltage source inverter that could be pulse width modulation (PWM), space vector, or any other choice. For the sake of this analysis, it will be modeled as a current source. The next section deals with the inverter model in more detail.

The generator needs to be capable of very fast operation, with speeds greater than 50,000 rpm. The dc link voltage needs to be large enough such that the inverter can synthesize the desired voltage. For the Honeywell™ micro-turbine, the output ac voltage is 120 Vrms, or 169 Vpeak. Therefore, the dc bus voltage must be at least 170 Vdc.

5.3 Honeywell 75-kW Micro-Turbine Test Results

Before any modeling can be done, it is necessary to detail the system that is to be modeled and identify the desired response of the model. To ensure that the model created is as accurate as possible, test results will be used as a desired goal. This implies that if the model matches these testing results under the same loading conditions, the model is a success.

The turbine generator tested was a 75-kW Parallon micro-turbine made by Honeywell. The testing was done at the University of California, Irvine, on Dec. 20, 2000, and prepared by Southern California Edison for CERTS.

The Honeywell™ micro-turbine has several modes of operation, consisting of island and grid-connected operation. However, the test data were taken for the grid-connected mode only. There is a large difference in these two modes, as any power difference between that developed by the micro-turbine and that required by the load is supplied by the grid. However, the data that is presented in this paper focuses only upon the power produced by the Honeywell micro-turbine.

The micro-turbine takes some time to get to steady state operation and for general warm-up. The testing results presented here were collected after the system achieved a steady state and do not include start-up transients.

Two loading sequences are considered. The first is power steps of 15 kW starting from 75 kW, stepping to 0 kW and then stepping back to 75 kW. The second loading sequence contains power steps of 30 kW. The waveforms from the 15 kW step commands are presented first.

The power command for the 15-kW step load case is presented in Figure 19.

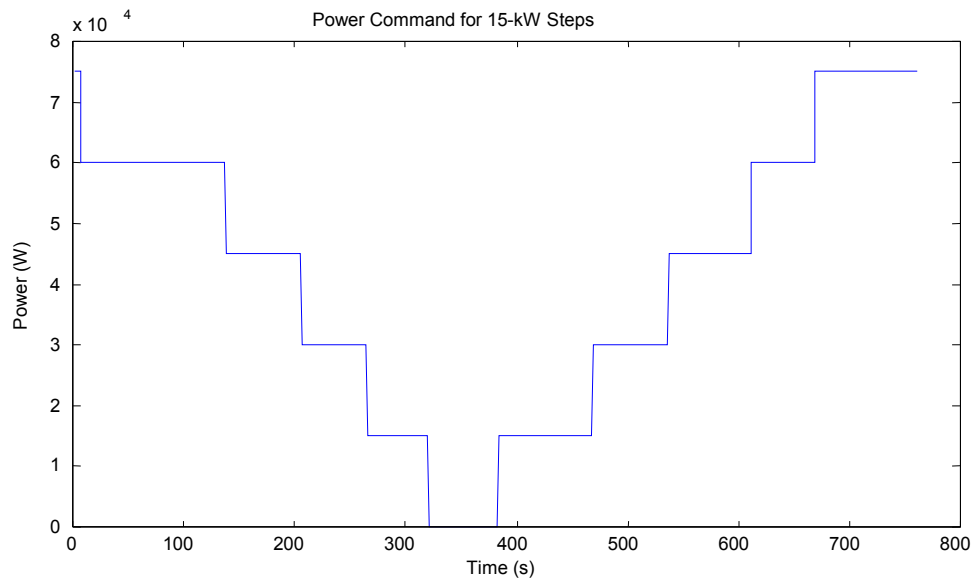


Figure 19: Power command to the micro-turbine for load change in 15-kW steps

The Honeywell system response to this loading profile will now be presented. Figure 20 shows the output power of the system. Note that the ramp time required to increase and to decrease power output.

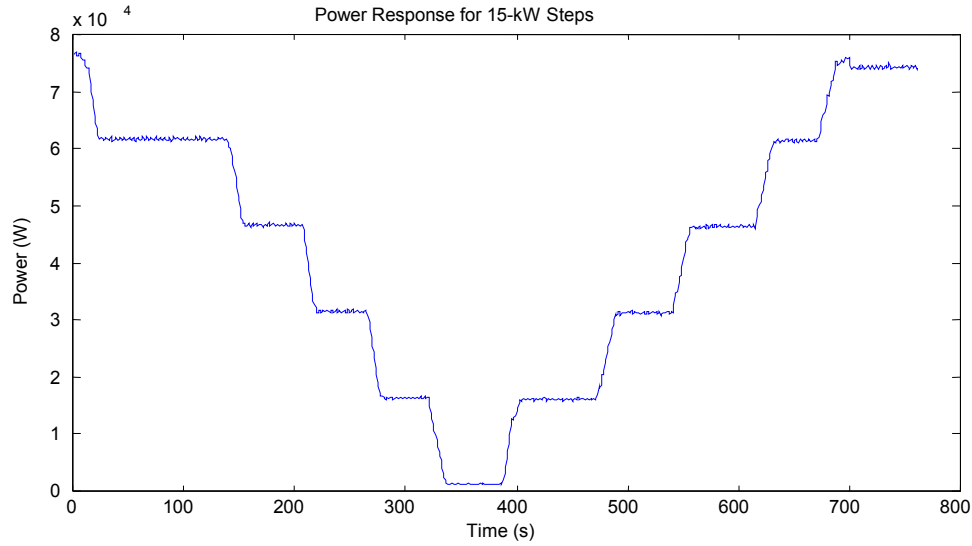


Figure 20: Output power of micro-turbine for load change in 15-kW steps

The shaft speed that results from the 15-kW step changes in load is shown in Figure 21. Note the speed overshoot in both the positive and negative load change directions.

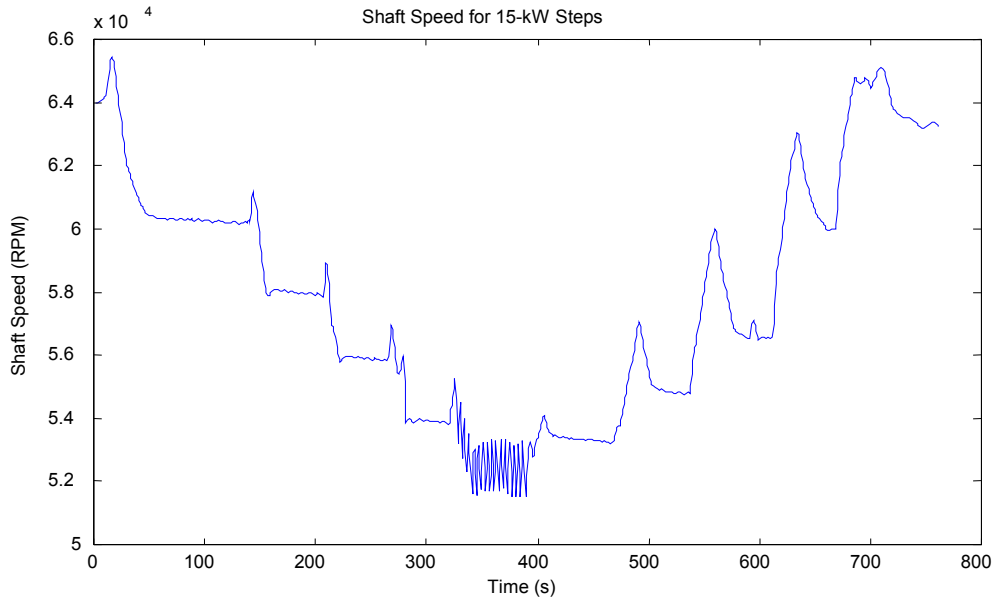


Figure 21: Shaft speed of micro-turbine for load change in 15-kW steps

The dc link voltage response to 15-kW step changes in load is shown in Figure 22. Note how the voltage does not appear to be regulated and follows the shaft speed curve.

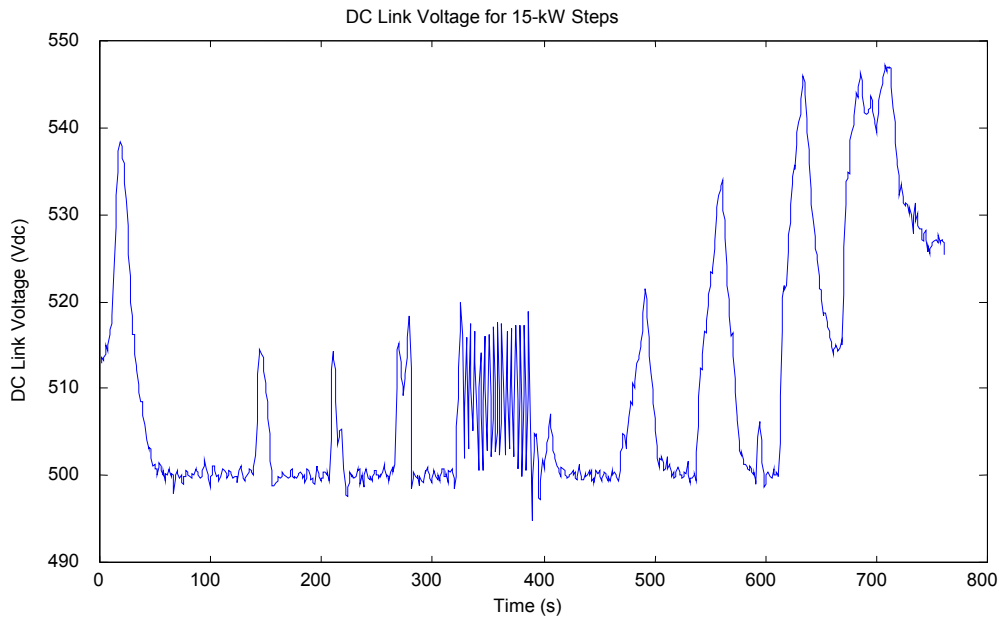


Figure 22: Dc link voltage of micro-turbine for load change in 15-kW steps

Other quantities such as dc link current and exhaust temperature have been collected but are not presented here. For a full overview of the test data, please refer to [4].

The same curves are now presented for the 30-kW step changes in load. Figures 23, 24, 25 and 26 show the power command, output power, shaft speed and dc voltage, respectively.

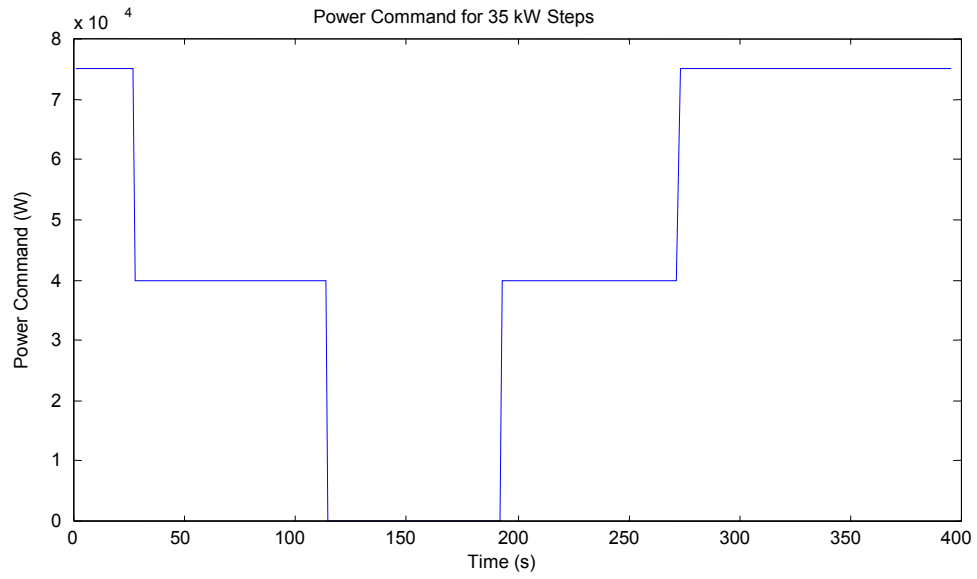


Figure 23: Power command of micro-turbine for load change in 30-kW steps

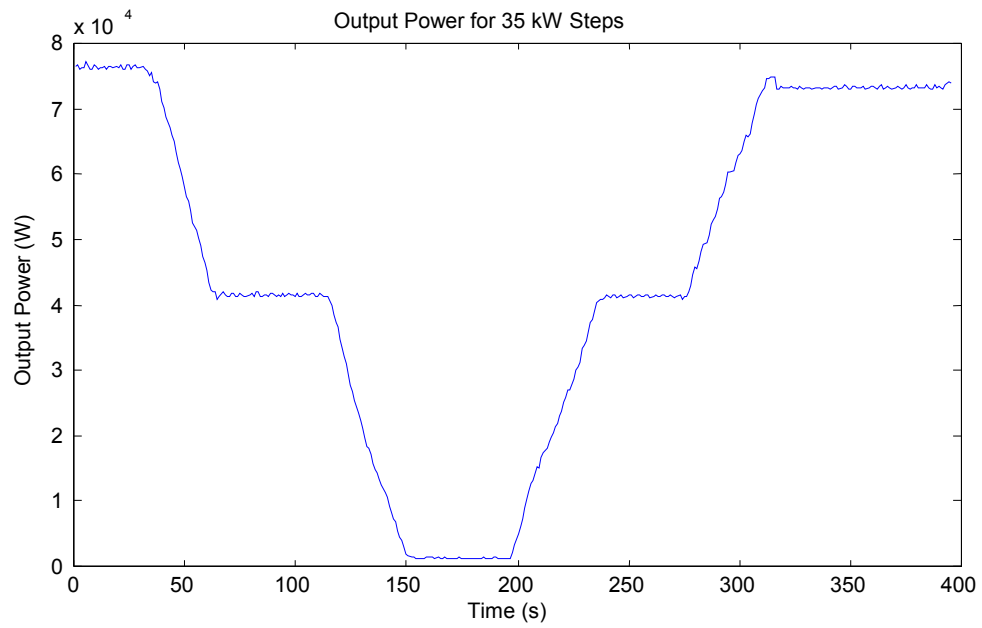


Figure 24: Output power of micro-turbine for load change in 30-kW steps

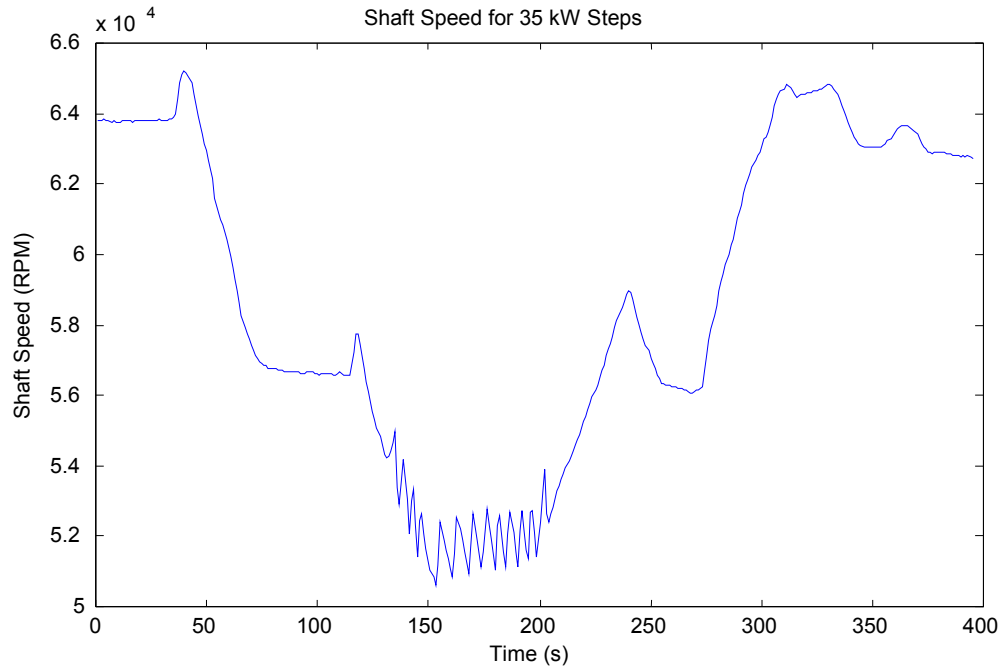


Figure 25: Shaft speed of micro-turbine for load change in 30-kW steps

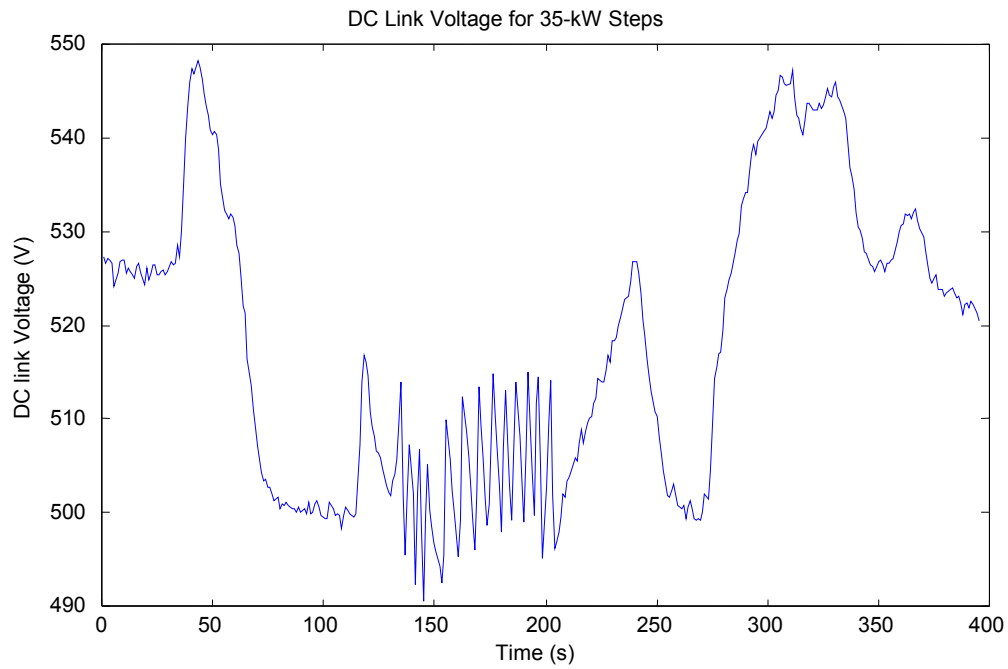


Figure 26: DC link voltage of micro-turbine for load change in 30-kW steps

A model can now be created, with the goal of obtaining similar responses for the same type of load changes.

5.4 Mathematical Model for the Micro-Turbine

Reference [15] contains a full development of the general approach used to create a mathematical model for the micro-turbine. The key equations are summarized here for completeness.

The circuit model used to describe the behavior of the turbine generator is shown below in Figure 27. This diagram shows a permanent magnet three-phase machine, with a passive diode bridge.

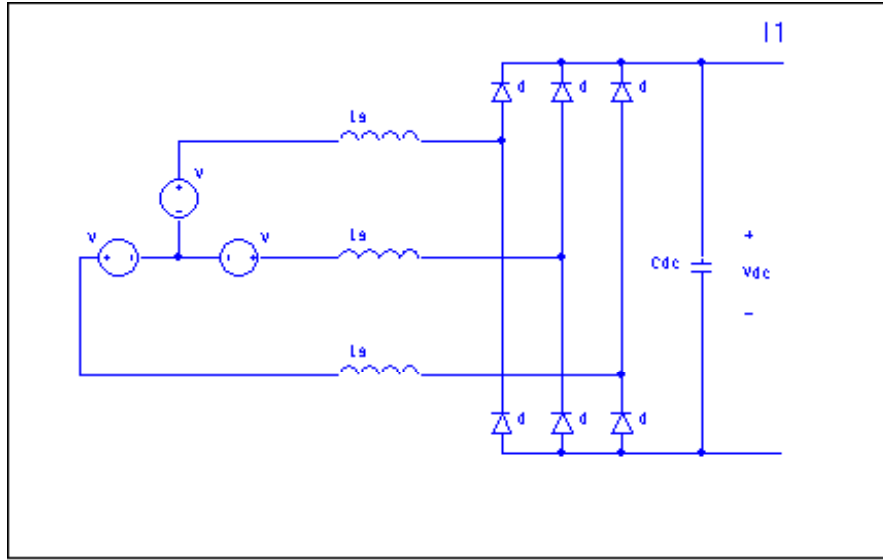


Figure 27: Circuit model of micro-turbine with passive rectifier

It should be noted that this model utilizes a diode bridge with a constant voltage source output. However, as noted in [15], this modeling problem is much more difficult than a diode bridge with constant current output. At first, this difference is troubling. However, the authors in [15] claim that experimental proof has shown that the two models are nearly equivalent, and for power delivery systems modeling purposes, this constant voltage output model can be substituted for a constant current output model if the correct value for L_s is chosen. This substitution is what will be done in the developments to follow.

The following mathematical expressions describe the quantities of interest for this system:

$$V_{11} = K_v \cdot \omega_e \cdot \sin(\omega_e \cdot t) \quad (17)$$

$$\omega_e = \omega_m \cdot \frac{P}{2} \quad (18)$$

$$V_{dc} = \frac{3 \cdot \sqrt{2}}{\pi} \cdot V_{ll} - \frac{3 \cdot w_e \cdot L_s}{\pi} \cdot I_{dc} \quad (19)$$

$$V_{dc} = K_e \cdot w_m - K_x \cdot w_m \cdot I_{dc} \quad (20)$$

$$K_e = \frac{3 \cdot P \cdot K_v}{2 \cdot \pi} \quad (21)$$

$$K_x = \frac{3 \cdot P \cdot L_s}{2 \cdot \pi} \quad (22)$$

The model parameters that need to be determined are the constants K_v , K_e and K_x . To determine these constants, test data will be used for the Honeywell micro-turbine.

The first constant that will be determined is K_e . This constant is found from Equation 20, by setting the current, $I_{dc} = 0$. This is the no-load operating point, and from the test data, the dc bus voltage during this condition is 500 Vdc. The mechanical speed of the rotor for no load is 52,000 rpm. Using this data, the constant K_e can be determined. It should be noted that the current into the dc link is not exactly 0 for no load but rather must keep the capacitor charged. However, $I_{dc} = 0$ is a good approximation to no load, assuming the capacitors do not leak tremendously.

$$K_e = \frac{500}{2 \cdot \pi \cdot \frac{52000}{60}} = 0.092 \quad (23)$$

The constant K_v can be determined using this result for K_e :

$$K_v = \frac{K_e \cdot \pi}{3} = 0.096 \quad (24)$$

A second operating condition is required to determine the final constant, K_x . It can be seen from the test data that when the Honeywell™ is producing 60 kW of output power, the rotor speed is 60,000 rpm, and the dc bus voltage is 515 Vdc. Using this information, and manipulating Equation 20, K_x can be determined.

$$K_x = \frac{\frac{515}{2 \cdot \pi \cdot \frac{60000}{60}} - K_e}{\frac{-60000}{515}} = 8.459 \cdot 10^{-5} \quad (25)$$

Now that the constants are determined, expressions for power and torque can be developed.

$$P_{dc} = K_e \cdot \omega_m \cdot I_{dc} - K_x \cdot \omega_m \cdot I_{dc}^2 \quad (26)$$

$$\tau_m = K_e \cdot I_{dc} - K_x \cdot I_{dc}^2 \quad (27)$$

We now have a manner in which to relate physical, controllable quantities, such as the torque of the prime mover or the shaft speed, to the dc link quantities. This is desirable because we want our model to apply to all types of micro-turbines, not just the 75-kW Honeywell™ micro-turbine.

Several approaches to a mathematical model are presented in [15]. The first, and the simplest, use the speed of the rotor as the input into the system. The dynamics, governed by the constants just calculated, determine the dc link quantities. A block diagram of this model is shown in Figure 28.

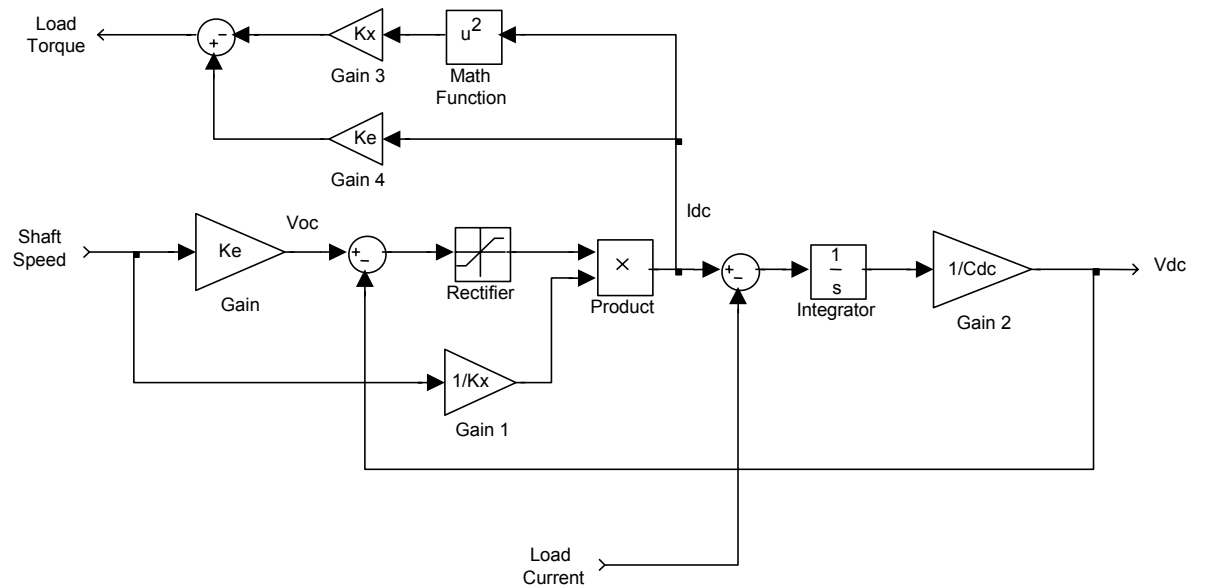


Figure 28:

Shaft speed model of a micro-turbine

This model has some very positive attributes, as well as some serious drawbacks. Positively speaking, it is a simple way to determine if a permanent magnet generator behind an inductance is an appropriate starting point. As a check, this model was simulated in SimulinkTM, with a few modifications.

The first modification that was made was to add a second order controller to the shaft speed input. This can conceptually be viewed, although poorly, as the dynamics of the fuel command and governor.

Several runs were made with this new model, and unsatisfactory results were obtained. To force the results to respond more like the data obtained for the Honeywell™ 75-kW generator, a curve-fitting routine was employed to create a parabolic relationship between the shaft speed and the power command. The model used to implement this strategy is shown in Figure 29.

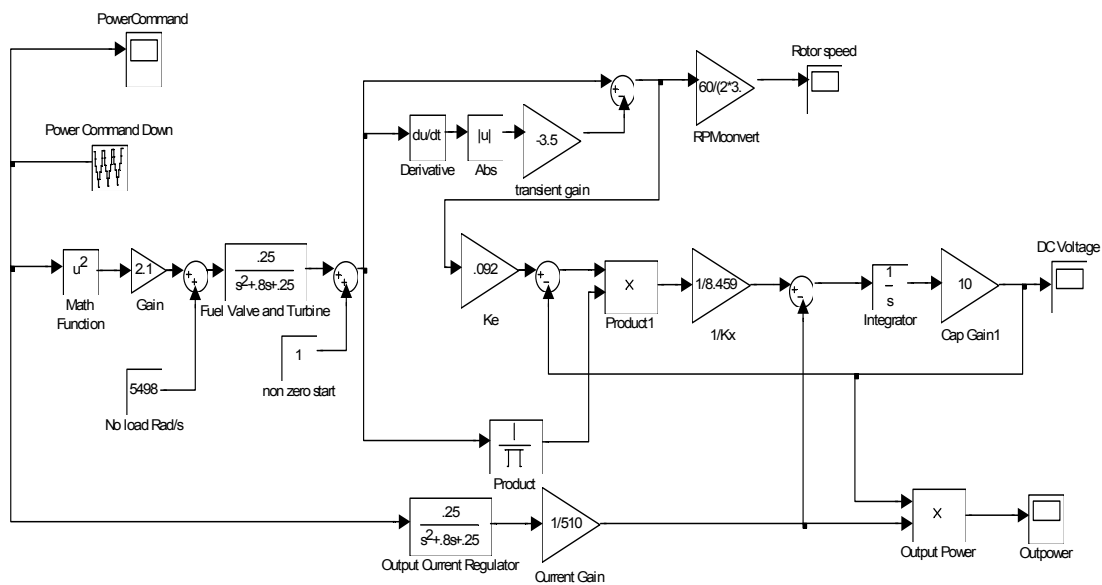


Figure 29: Curve-fit shaft speed model of a micro-turbine

In addition to the quadratic curve fit and the second order transfer function added at the input, there is a transient gain added to the shaft speed after it is fed forward. This gain, again, has little physical significance other than it creates a better match between the simulated results and the test results.

The power command input into the systems is shown as Figure 30. The time sequence is slightly different from the Honeywell™ test data; however, the step nature and magnitude are the same.

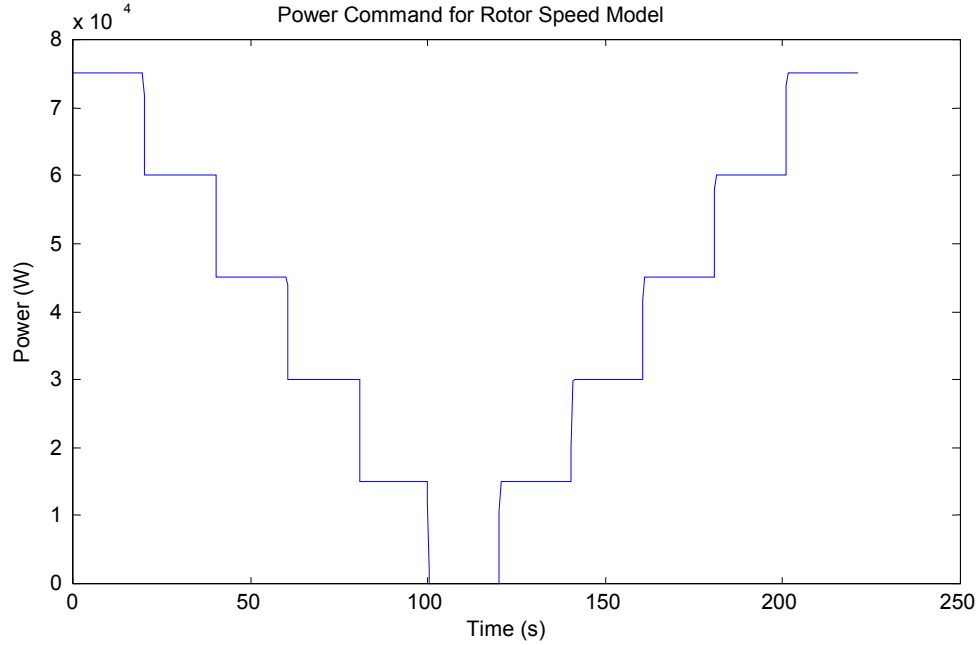


Figure 30: Power command to the curve-fit shaft speed model

The load current has been chosen such that the dynamics are similar to that of the Honeywell's inverter. Consequently, the output power from the model has many similarities to the test data and is shown in Figure 31.

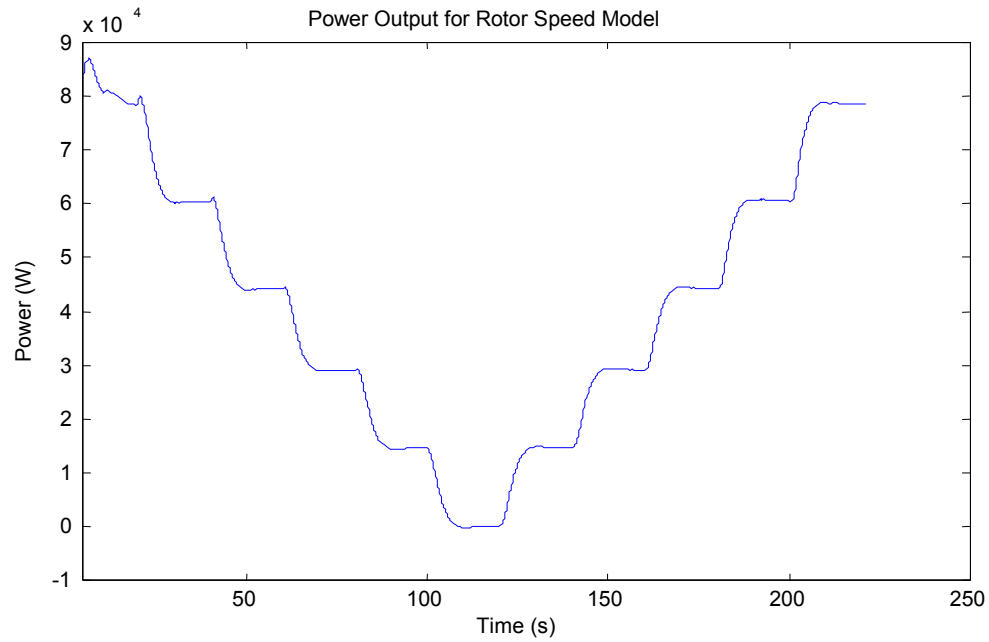


Figure 31: Output power from the curve-fit shaft speed model

The rotor speed from the model has been curve fit such that it is relatively close to the test data. The rotor speed response is shown in Figure 32.

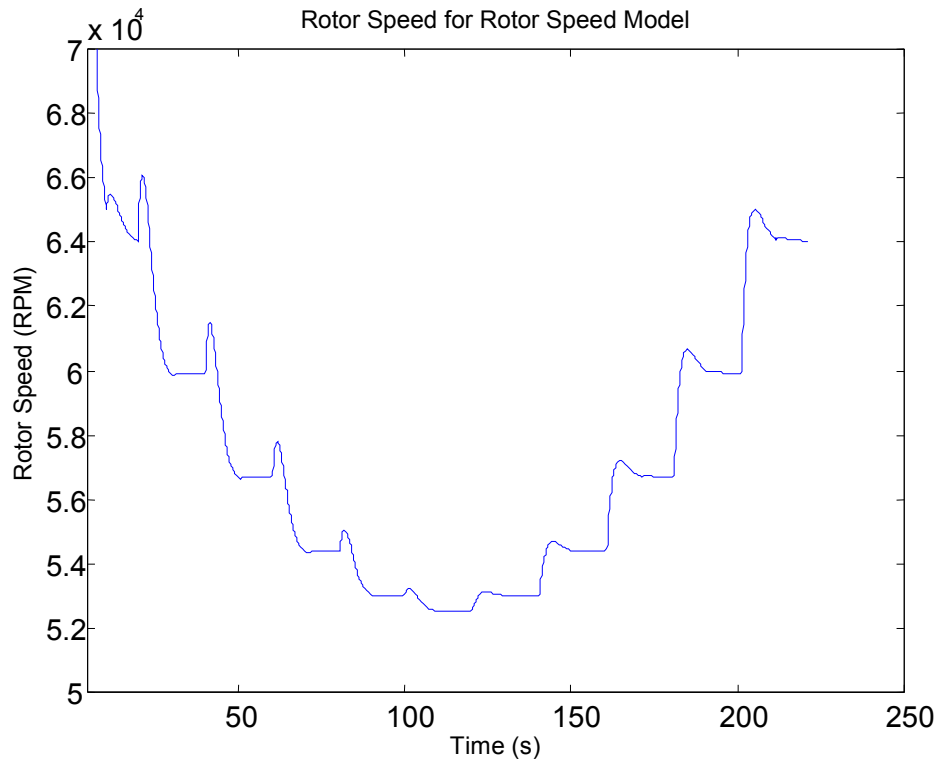


Figure 32: Rotor speed from the curve-fit shaft speed model

The parabolic curve fit is evident in the rotor speed response. The actual test data do have a parabolic nature but not to this same degree. However, the basic rotor speeds are of the right magnitude once a steady state speed is reached for each power level.

Perhaps the most important response from this model is the dc link voltage. The parameters have been determined such that the proper voltage is obtained for the expected rotor speeds. The dc link voltage response shown in Figure 33 reveals that the parameters are appropriate, as corresponding rotor speeds produce the desired dc link voltages.

The dc link voltage follows the parabolic shape of the rotor speed; however, it does not rise as fast. The ‘K’ parameters determined before control the relationship between a rotor speed, load level and dc link voltage. Some tuning could be done to create a better fit for this model.

An important response to note for both the rotor speed and dc link voltage is that there are over-speeds (over-voltages) for both step up and step down changes in load. This response was forced in this model. An ideal model would be controlled such that these overshoots would result.

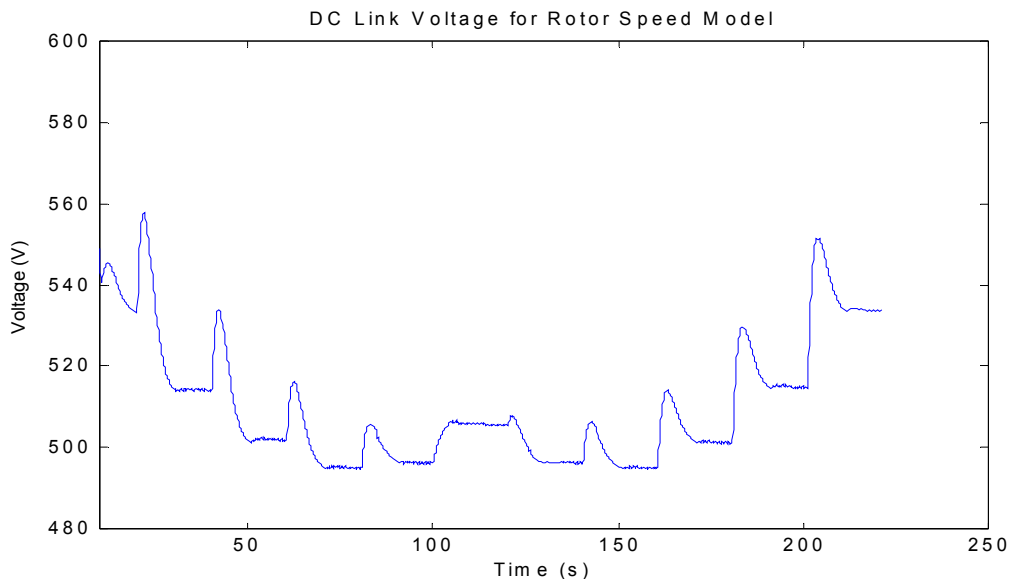


Figure 33: DC link voltage from the curve-fit shaft speed model

In summary, the success of this model requires the following conditions:

1. The rotor speed is curve fit to the test data.
2. The transient pulses are “falsely” amplified by a derivative term that must be tuned for different operating conditions.

3. The load current must be constrained in the same manner as the inverter is limiting output current responses to load change.

The major detriment to this model is that the micro-turbine dynamics are not included. The size of the turbine and generator will, intuitively, affect the rotor's ability to respond to speed change commands. None of these effects is included in the model. However, the parameters are tuned correctly.

5.5 Torque Input Model

A second model was created that incorporates the micro-turbine dynamics, with a torque input command. This model has been developed in [15] and is shown in Figure 34.

This model is very much like the shaft speed model, with the large exception of the developed torque feedback, and a prime mover torque input. In addition, this model contains the micro-turbine dynamics, expressed as the lumped parameter J , that the shaft speed model did not have.

The constants that were calculated for the shaft speed model remain the same; all that is required is to obtain an estimate for the moment of inertia, J , of the generator and micro-turbine. This calculation and result is developed below.

The basic expression for the moment of inertia is:

$$J = \int r^2 \cdot dm \quad (28)$$

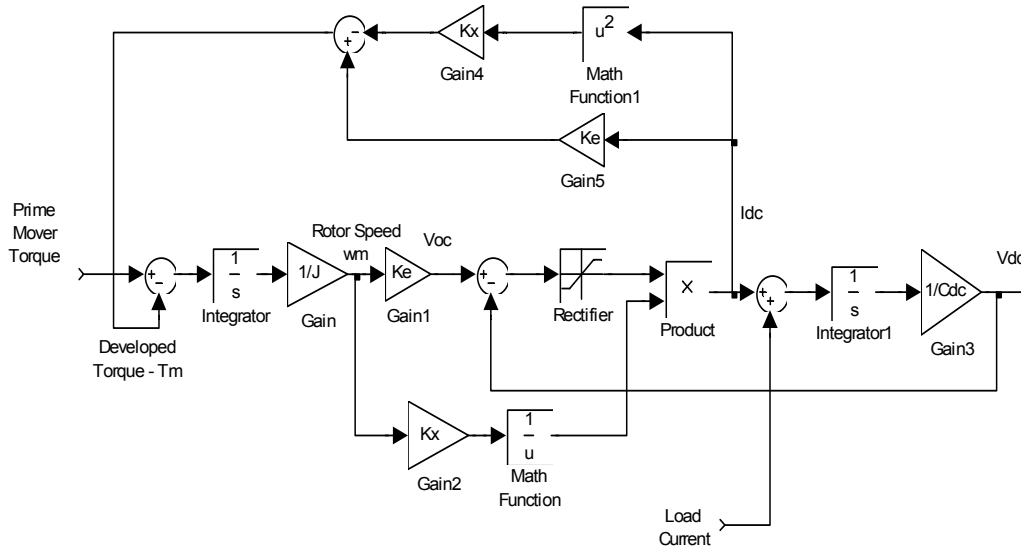


Figure 34: Torque input model of a micro-turbine

However, for simplicity's sake, the rotational system will be modeled as a solid cylinder, for which the moment of inertia is:

$$J = \frac{1}{2} \cdot M \cdot r^2 \quad (29)$$

In photographs of the Honeywell™ micro-turbine, the length of the unit is approximately ½ meter. The shaft radius is approximately 10 cm, which would make the shaft and blades about 17 kg. Using this data, the moment of inertia is determined as 0.085 kg-m². This is a very rough number, but it is a good starting point.

The nature of the feedback makes this model much more difficult to obtain the appropriate prime mover torque and the appropriate load current. To validate this model, and to place bounds on these quantities, the Honeywell test data was used as input. The test data was entered into MATLAB™, and input blocks were created in Simulink™. The entire model, with test data inputs, is shown in Figure 35.

Note that the load current, which is obtained from the test data, has been divided by the input power, which ensures conservation of energy. This is an important part of this model, for the output quantities run away with the slightest imbalance. Only this type of feedback created a solution that converged.

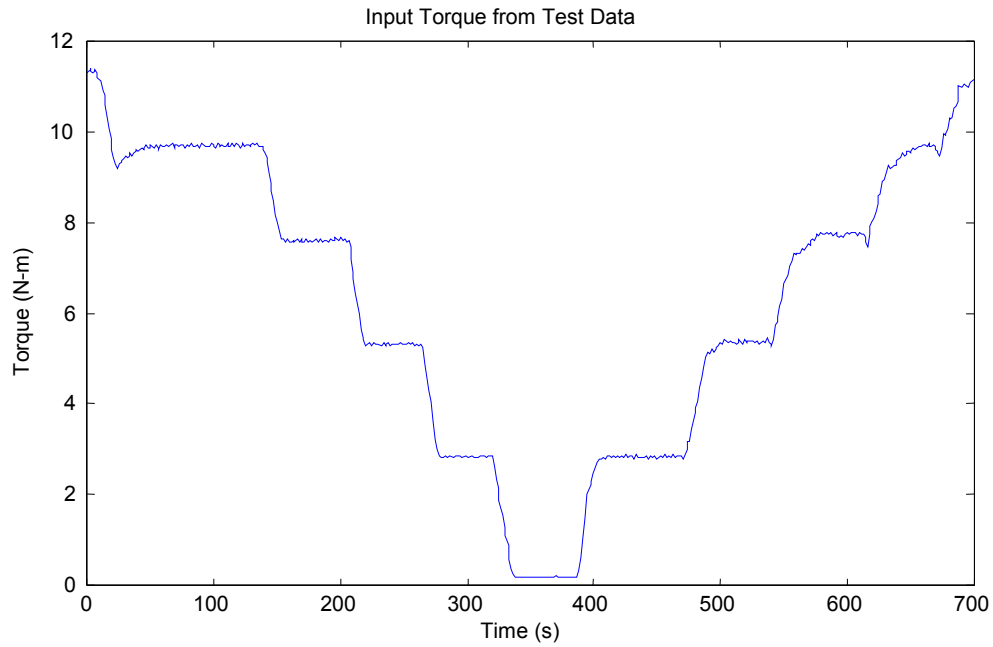


Figure 36: Input torque for the torque input model

The load current from the test data that is input into the system is shown in Figure 37. Note that the same ramp time that was forced in the rotor speed model because of the inverter is seen in this waveform.

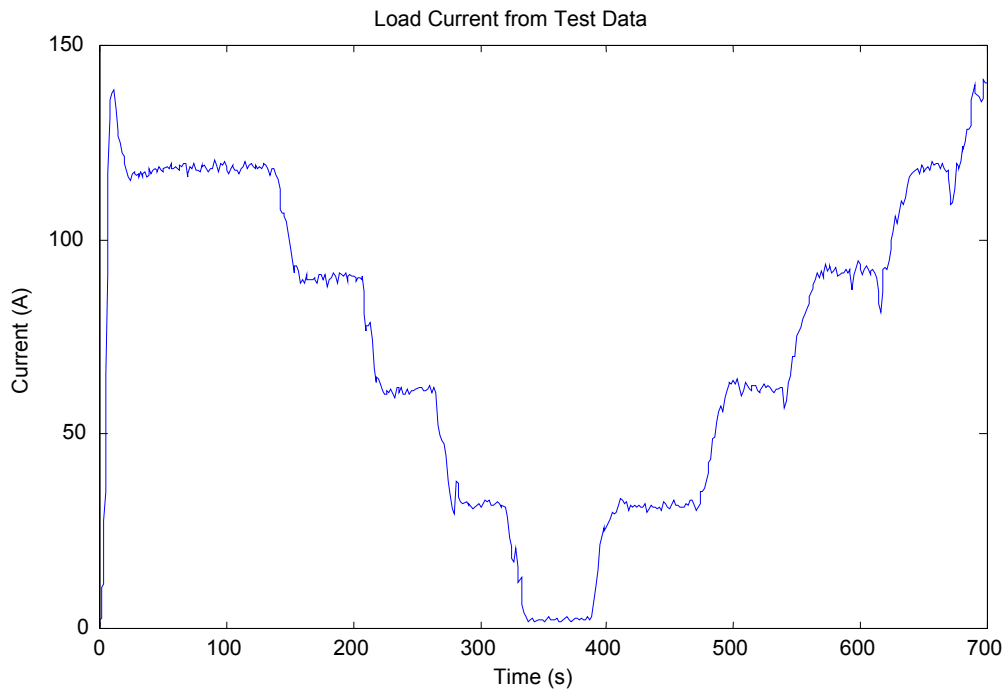


Figure 37: Inverter load current for the torque input model

The resultant output power, rotor speed and dc link voltage are shown in Figures 38, 39 and 40, respectively.

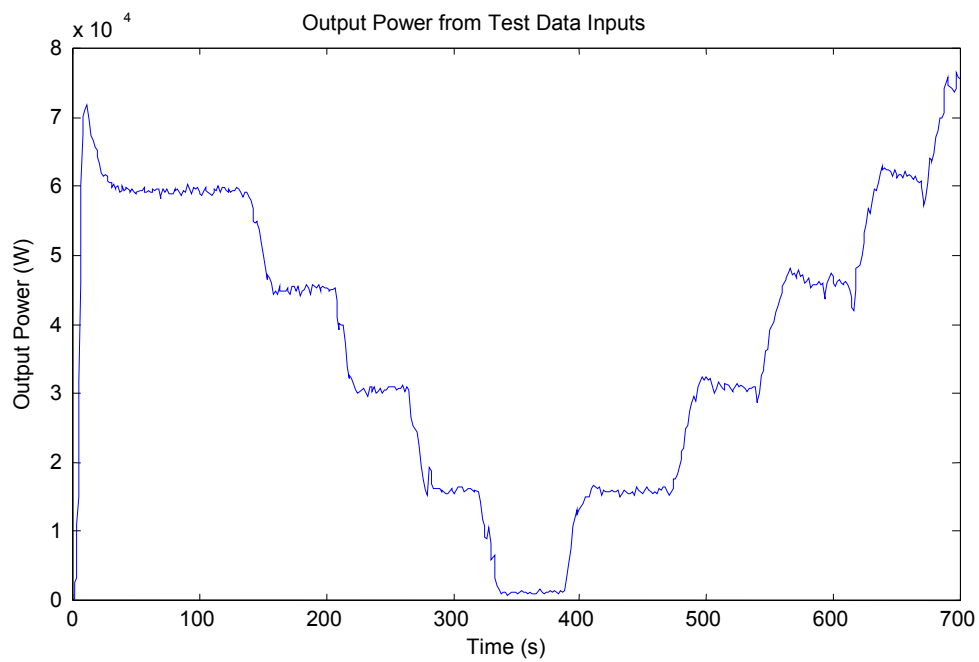


Figure 38: Output power from the torque input model

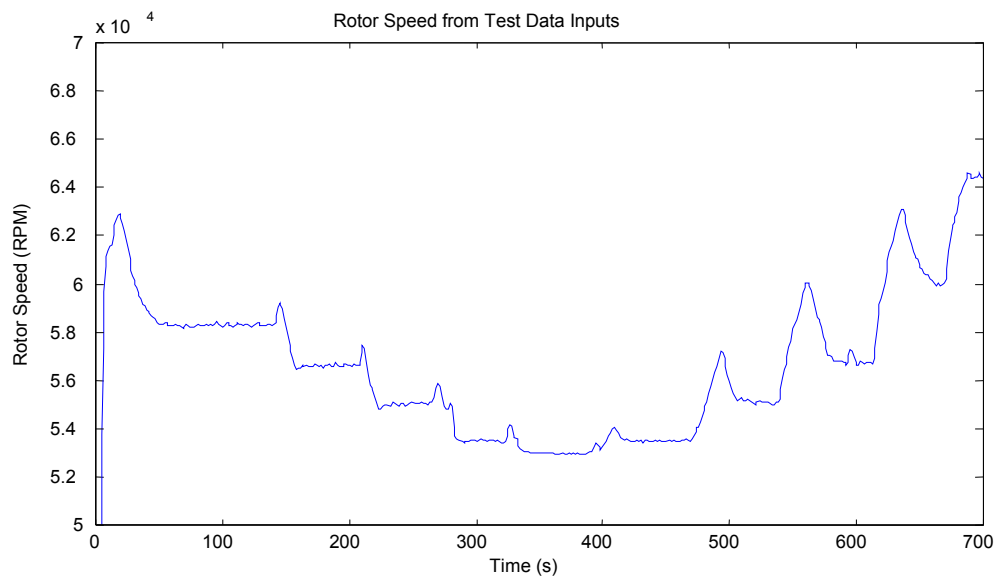


Figure 39: Shaft speed from the torque input model

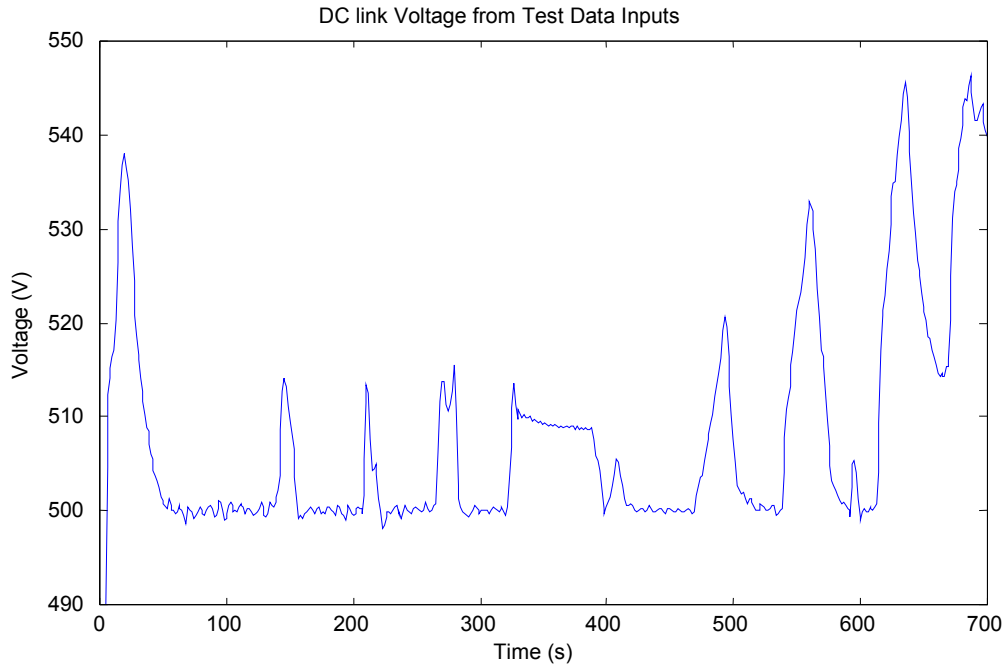


Figure 40: DC link voltage from the torque input model

The output power, rotor speed and dc link voltage responses match the test data closely. The same general behavior is observed, with very few discrepancies.

There are no oscillations of the dc link voltage for no load. This behavior is difficult to explain in the test data, and its absence in the model's response is not surprising.

The same over-voltage and over-speed is seen in the test data and the model response. This is encouraging, as the input signals do not contain these spikes, but rather they are a dynamic reaction to the load step change. Also, the magnitudes of the dc voltage and rotor speed are very similar.

The torque input model is a good model for the Honeywell micro-turbine. These results are general enough to be applied to many different manufacturers and micro-turbine models.

The inputs into this system were from test results, which are difficult to reproduce. An attempt will now be made at creating a more closed system, with a guess at the type of controller used in the Honeywell micro-turbine.

5.6 Honeywell™ Model with “Bang-Bang” Controller

As mentioned previously, the test results of the Honeywell™ micro-turbine were for a grid-connected mode. This implies that the inverter feeding the loads did not have to act instantaneously but rather could ramp loads in an arbitrary manner. The loading profiles could maintain optimum efficiency of the unit, but regardless of the reason, the system’s response to load changes is relatively slow (5-20 s).

A controller was then created to give a prime mover torque command. This controller replaced the test data that was used previously. However, the load current remained an input from the test data. This was done so that the system’s response under test was still applicable for comparison against the model with the controller’s response. When island data is obtained, this loading profile can be changed.

Upon examination of the Honeywell’s response to step changes in the load, the following conclusions were made regarding the nature of the controller:

1. The dc bus voltage is *not* a controlled variable and is allowed to float.
2. The load tracking capability is controlled by the inverter, which draws current from the dc bus.
3. Any agitation, either positive or negative, of the dc load current results in an increase in rotor speed.
4. The torque is used as the primary control of power input into the system, rather than the rotor speed. The rotor speed does not drop below 52,000 rpm; however, the torque fluctuates greatly with load.

Upon evaluating the criteria listed above, the controller in Figure 41 was created. It will be referred to as a “Bang-Bang” controller because of its over-reaction to load changes.

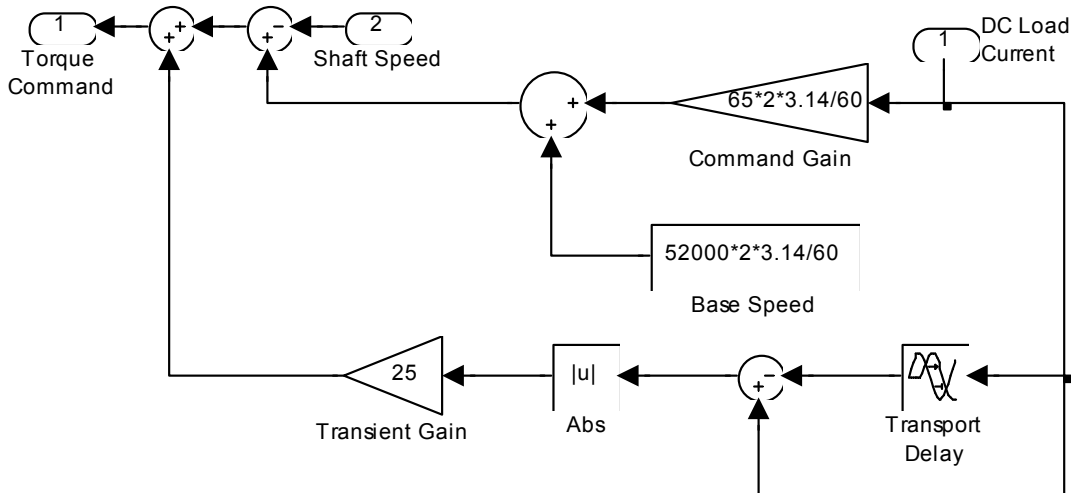


Figure 41: Block diagram of the “Bang-Bang” controller

The “Bang-Bang” controller compares the shaft speed to a reference speed created by the summation of a minimum speed, 52,000 rpm, and a load current dependant term. The difference in the shaft speed and the calculated reference is the torque command. The torque command is modified when there is a change in the load current. Twenty-five is multiplied by the magnitude of the change in the load current to create the additional term to the torque command. This outer loop is what is responsible for the over-speed and over-voltage seen on load transients.

The entire system, with controller, is shown in Figure 42. The Honeywell™ micro-turbine model, which is represented as a block in Figure 42, is shown in Figure 43. The micro-turbine model is the same as the torque input model.

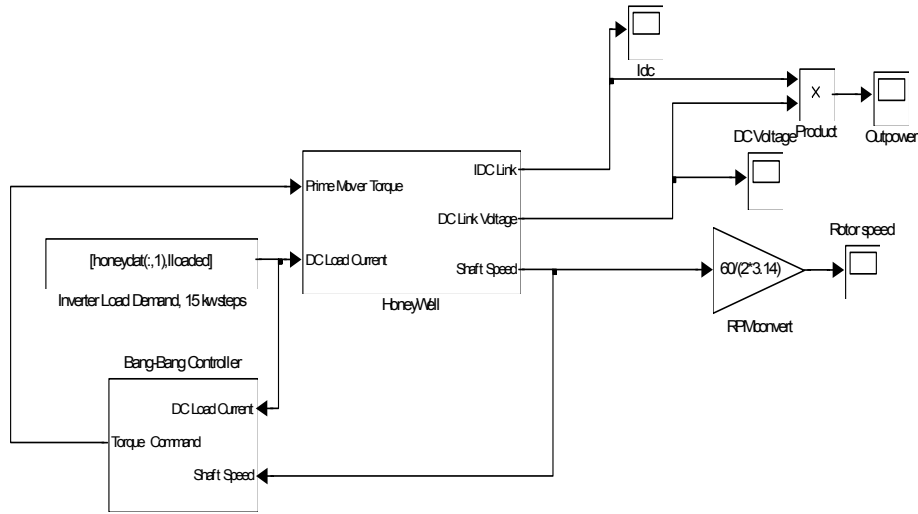


Figure 42: “Bang-Bang” controller and Honeywell™ micro-turbine model

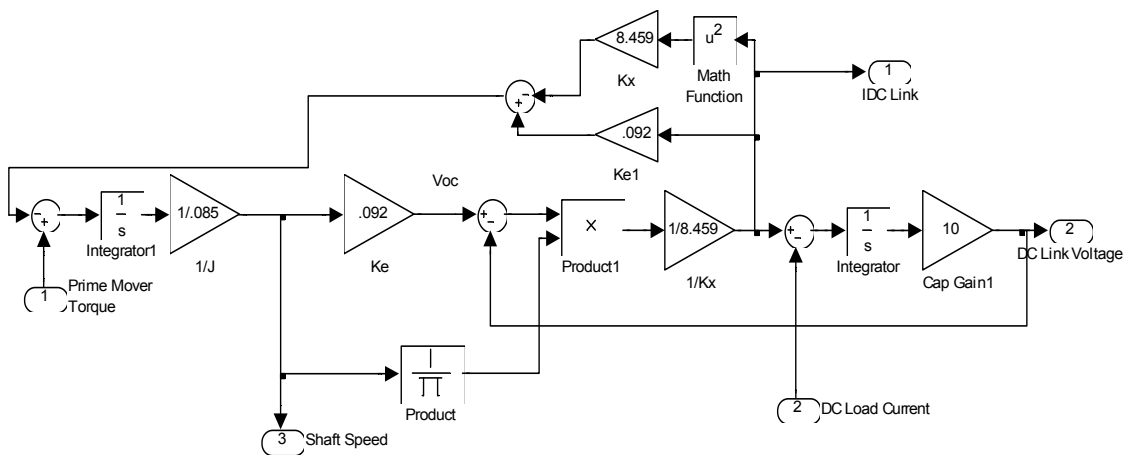


Figure 43: Honeywell™ micro-turbine model

As mentioned previously, the load current input into the system is supplied by the test results. However, the torque command to the prime mover is developed from other model quantities, as was desired.

The systems response with this controller to the 15-kW test load steps is shown in several figures. Figure 44 shows the torque input into the system from the controller, Figure 45 shows the shaft speed, Figure 46 shows the DC link voltage, and Figure 47 shows the output power from the system. A comparison between the test results and the model's response with the “Bang-Bang” controller reveals that this system is a decent approximation to the Honeywell™ micro-turbine.

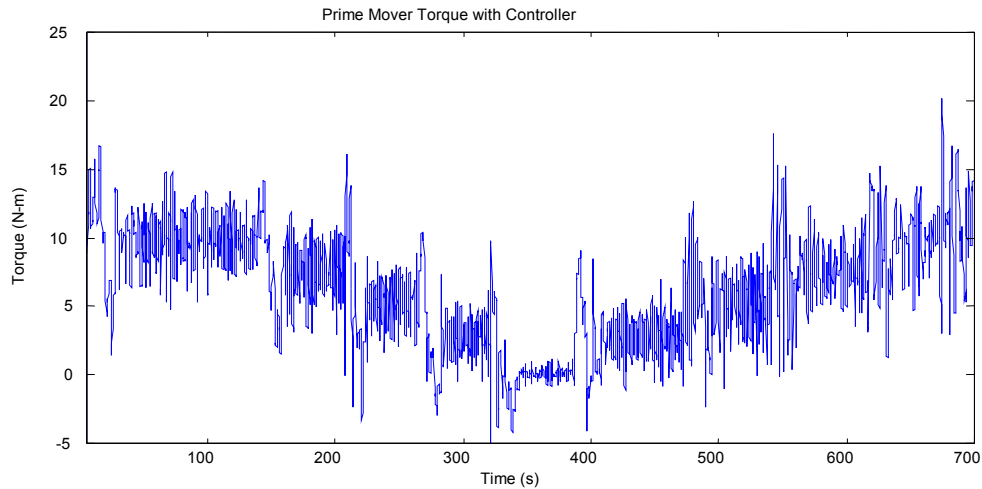


Figure 44: Torque input provided by the “Bang-Bang” controller

However, there are some discrepancies, such as the rotor speed at higher power levels and the dc link voltage steady state value for mid-level output power. It is believed that the controller could be better tuned, and perhaps more complexity could be added to improve the response.

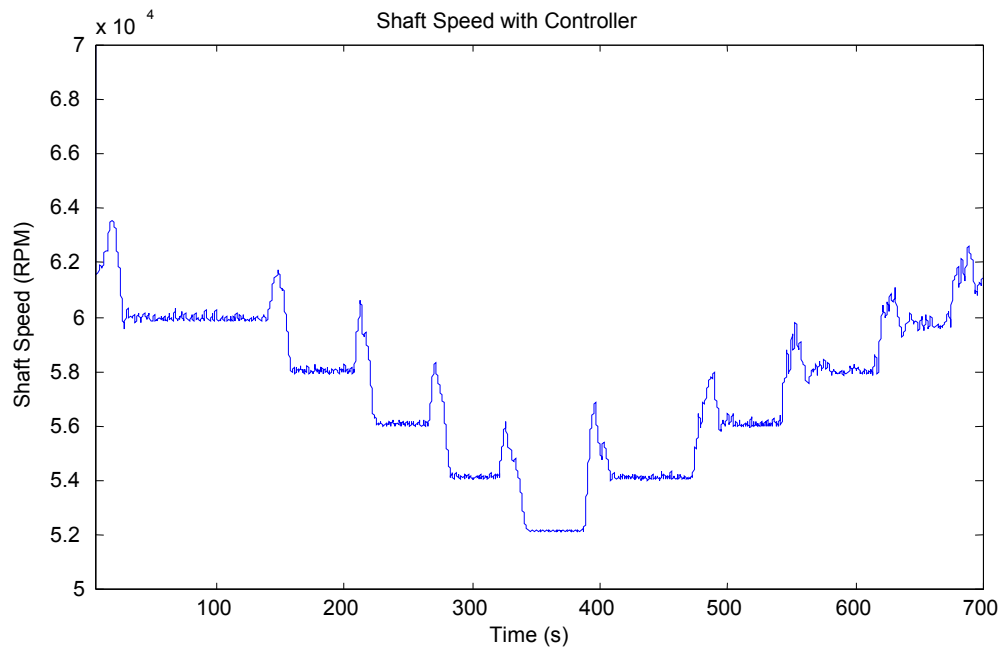


Figure 45: Shaft speed from Honeywell™ micro-turbine model with the controller

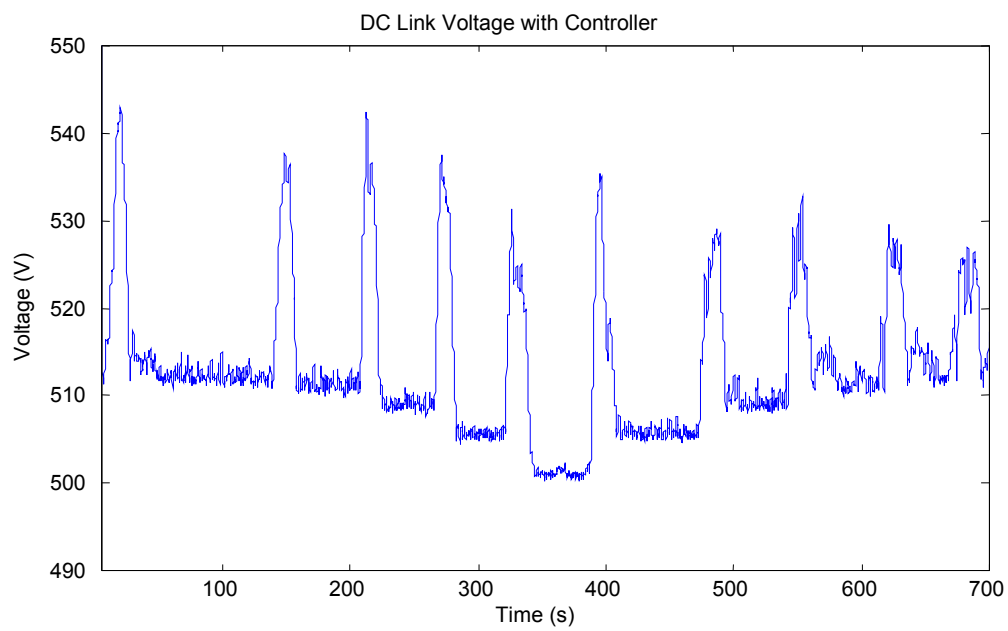


Figure 46: Dc link voltage from Honeywell™ micro-turbine model with the controller

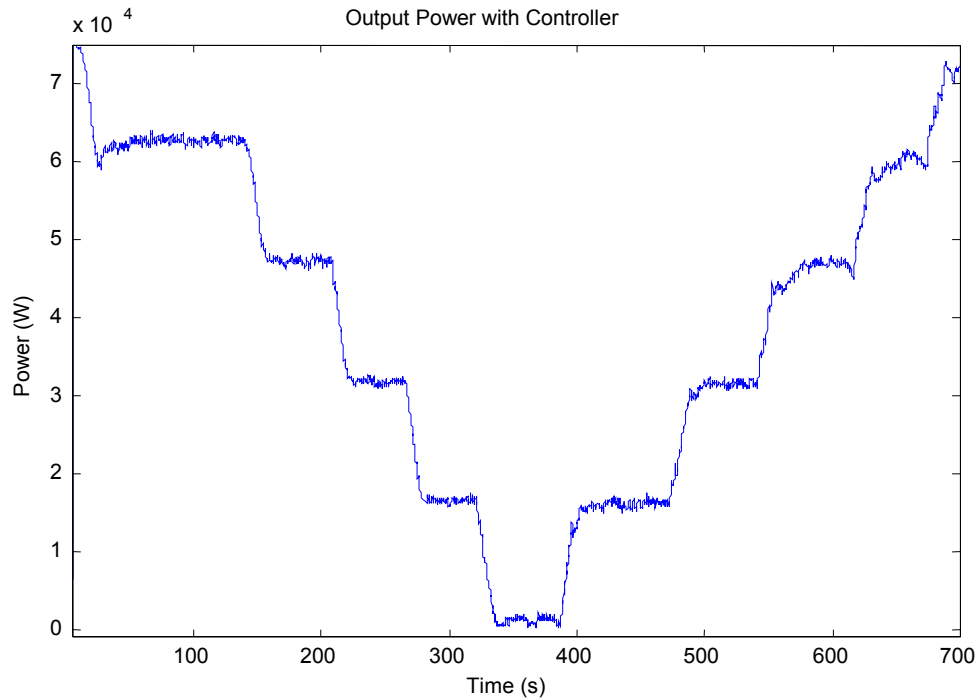


Figure 47: Output power from Honeywell™ micro-turbine model with the controller

A second set of test data for larger power steps was taken. Just as was done before, the load current was determined from the test data. The systems response to these larger steps in power are shown in three figures. Figure 48 shows the rotor speed, Figure 49 shows the dc link voltage, and Figure 50 shows the output power.

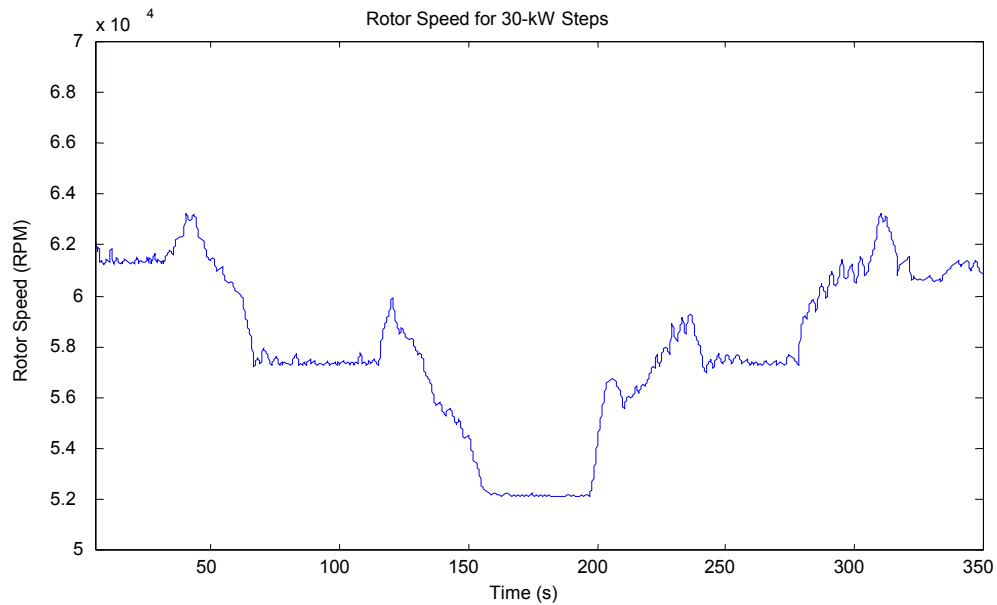


Figure 48: Rotor speed from Honeywell™ micro-turbine model with the controller

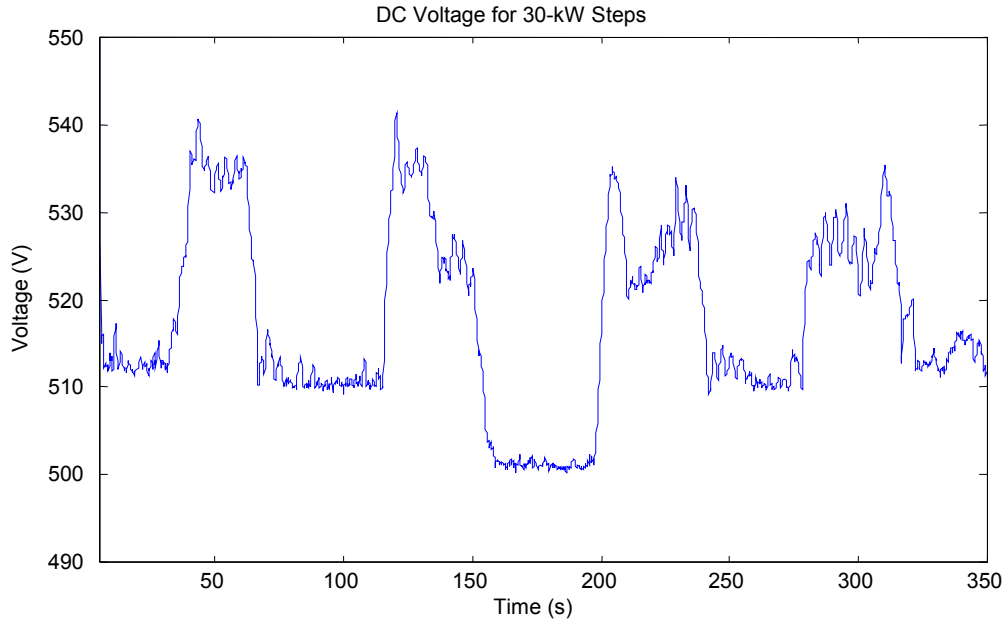


Figure 49: Dc voltage from Honeywell™ micro-turbine model with the controller

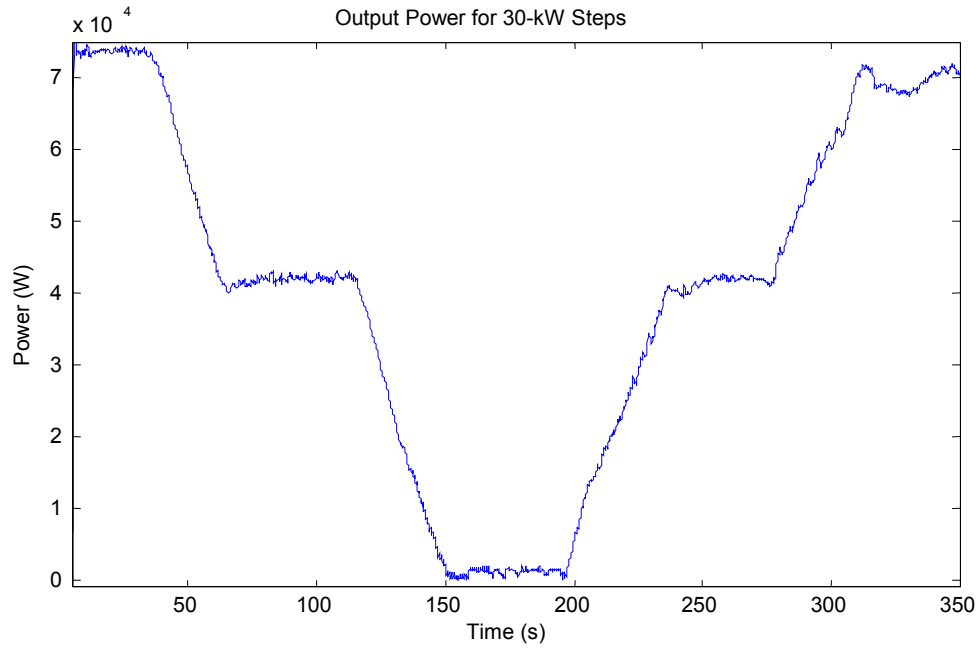


Figure 50: Output power from Honeywell™ micro-turbine model with the controller

The model behaves in a similar manner for the 30-kW steps. However, the rise times, voltage magnitudes and rotor speed responses do not match the test data as well as they did for the 15-kW steps.

The model, with controller, is accurate enough to be used in simulations for load flows and transient studies. In addition, the model could be used to determine a more efficient control strategy, such as dc link voltage control or output current control.

Because the inverter determines the rate at which the load is tracked, there is currently no evidence to determine the maximum rate the micro-turbine itself responds to load. In an attempt to predict this, a change to the load current was used as input into the model. This time, a step change in load current was input as opposed to the ramp level set by the inverter. In this manner, the micro-turbine's predicted response in an island mode could be predicted.

Figure 51 shows the output power of the model to a step change in load current. Note the rate of response and the overshoot.

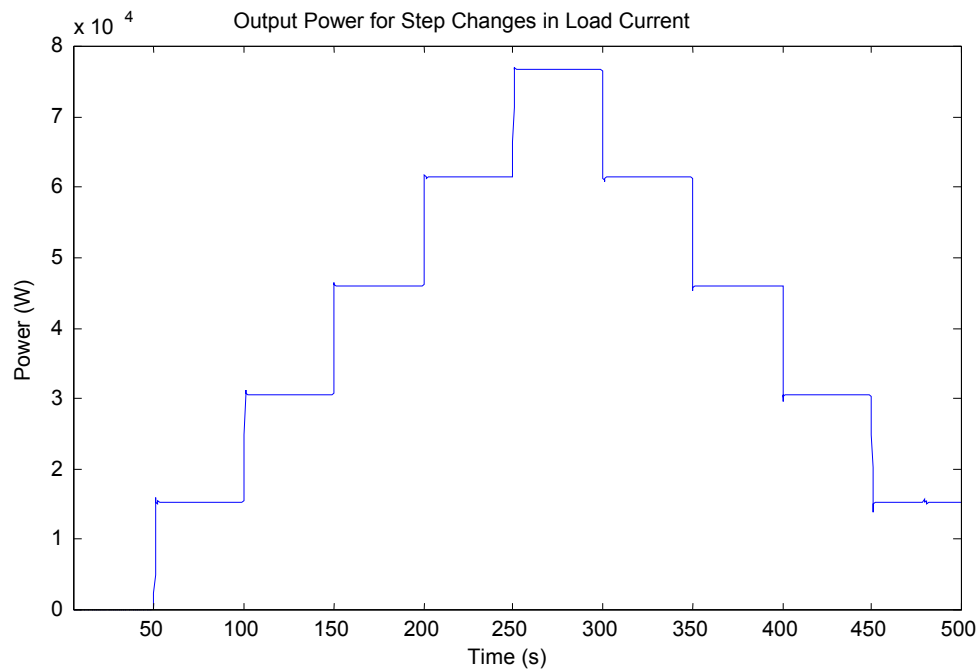


Figure 51: Output power from step changes in load

The response rate to the step changes is a near perfect step output. There is a slight overshoot, but the controller could be tuned to reduce this part of the response.

The “Bang-Bang” controller was changed to allow the simulation to converge. This was needed because the step change in the load current could not be tracked by the outer loop of the controller.

The output power response's deviation from a perfect step is a strong function of the moment of inertia, J , of the turbine and rotor. This value sets a response speed limit that is yet to be determined. The “island” mode data will increase the understanding of this limit.

5.7 DC-DC Converter Emulation of a Micro-Turbine

The Honeywell's response to load in a grid-connected mode is dominated by the inverter that supplies the load from the dc bus. However, the micro-turbine has an inherent capability to respond to load changes in a very fast manner.

Inverter control methodologies have been improved greatly in the past decade, aided by the improvements in power semi-conductors. As the switching frequencies of inverters increase, their ability to respond to load changes also increases. Considering the time requirements of the micro-turbine and the inverter, it is probable that the micro-turbine is the limiting factor in load tracking issues.

The remainder of this paper will investigate the ability of a dc-dc converter to emulate the response of a micro-turbine.

5.8 DC-DC Converter Topology

Many circuit topologies could be used for dc-dc conversion. Of the options available, a half bridge converter is the easiest to simulate. However, regardless of the topology, the same basic principle applies: the longer the duty cycle, the larger the output voltage.

The converter to be simulated is shown in Figure 52. This converter has two transistors, which when on, place either V_+ or V_- across the primary of the transformer. The output voltage is a function of the input voltage, the duty cycle of the transistors and the turns ratio of the transformer.

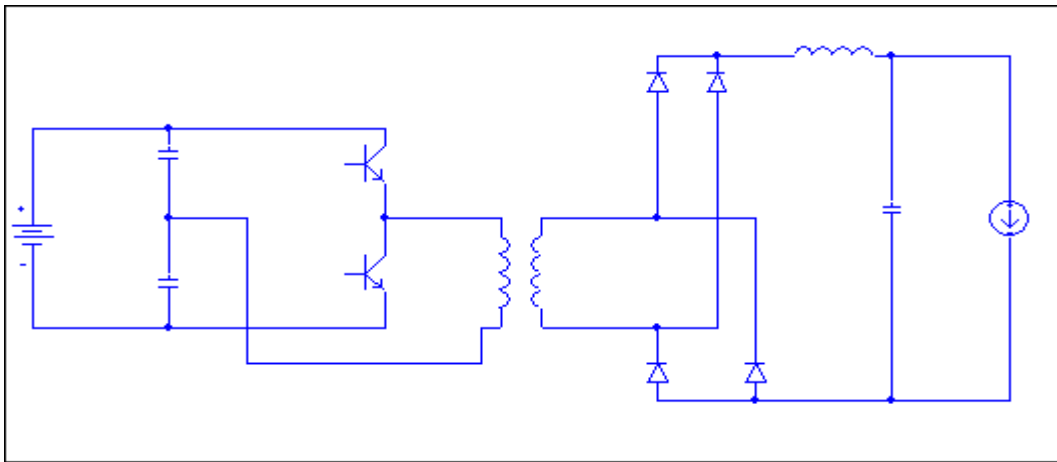


Figure 52: Half-bridge dc-dc converter topology

The output of the converter is a full bridge rectifier, feeding a filter inductor and dc link capacitor. A change in the duty cycle of the transistors equates to a nearly instantaneous change in the voltage across the transformer (one cycle). However, the dynamics of the dc link quantities are not nearly that fast. Time is required to charge the capacitor and to increase or decrease the current in the inductor. Therefore, the dynamics of this dc-dc converter are dominated by the dc link quantities.

A simplified circuit diagram of the dc link and the output inverter is shown in Figure 53. Note that the inverter is modeled as a current source, which changes magnitude with the load.

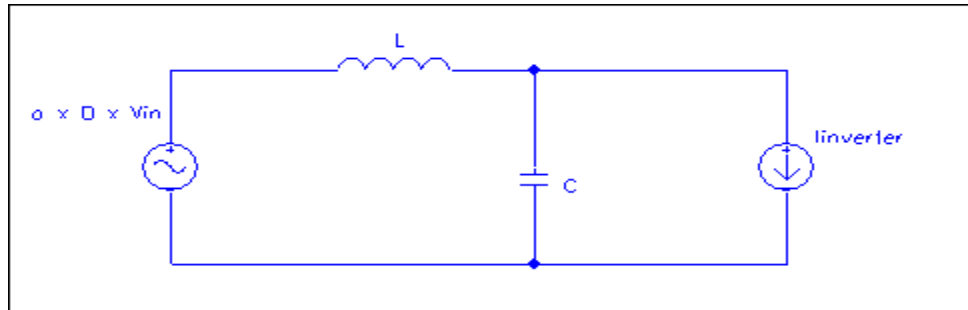


Figure 53: Simplified dynamic model of half-bridge converter

The nodal equations are written for this model, and the Simulink™ model shown in Figure 54 is obtained. Note that the current source is determined by a power command.

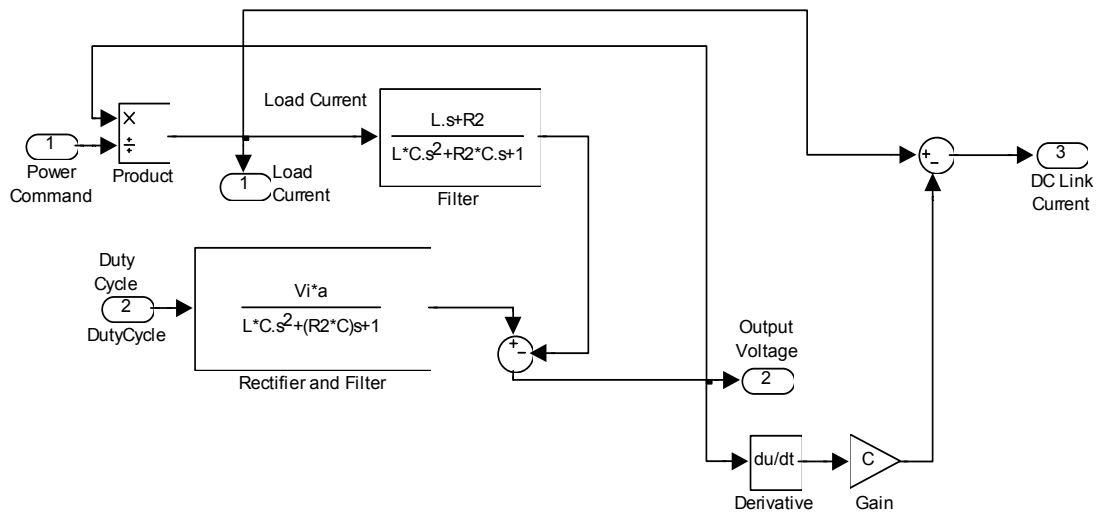


Figure 54: Simulink™ model of dynamic model of dc-dc converter

In the model in Figure 54, the output voltage is a function of the duty cycle and the load current (these two relationships have been expressed in two different transfer functions, which are summed to produce the output).

The first control strategy investigated was to maintain the dc bus voltage at a fixed set point. The load current makes instantaneous jumps in value, and the controller must track these and adjust the duty cycle appropriately.

The system, with voltage controller, is shown in Figure 55. Figure 56 shows the details of the voltage controller.

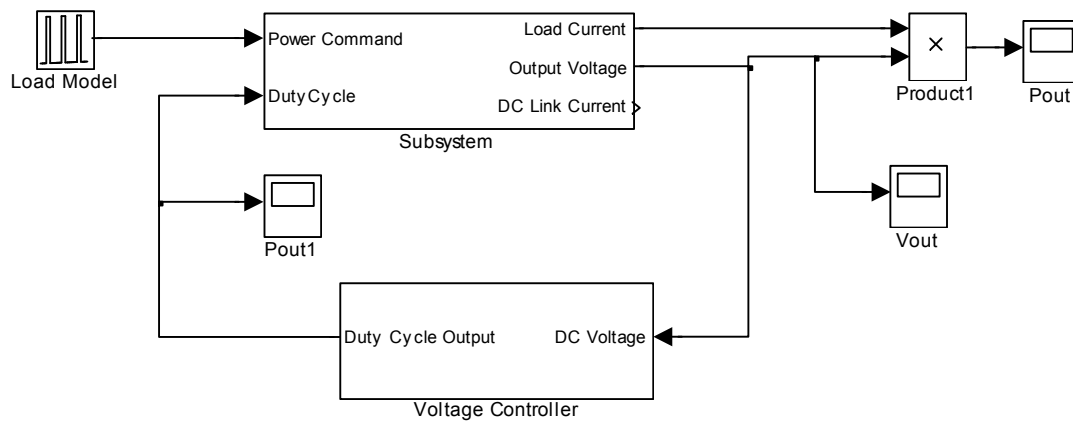


Figure 55: Dc-dc converter system with voltage controller

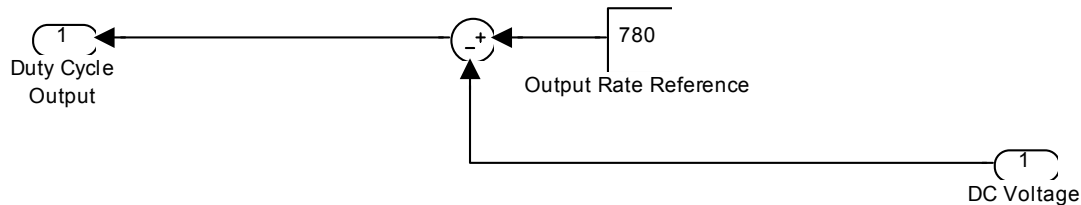


Figure 56: Proportional control of dc bus voltage

The output voltage and power responses to step changes in load are shown in Figures 57 and 58, respectively. Note that the dc voltage remains fixed, at the 780 V set-point, less the error. Note also that the output power changes nearly instantaneously.

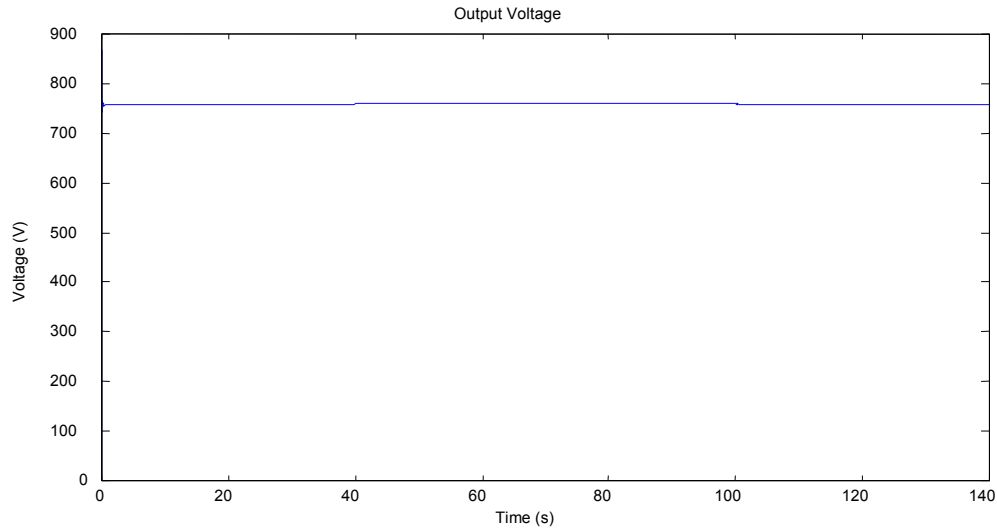


Figure 57: Dc output voltage for step changes in load

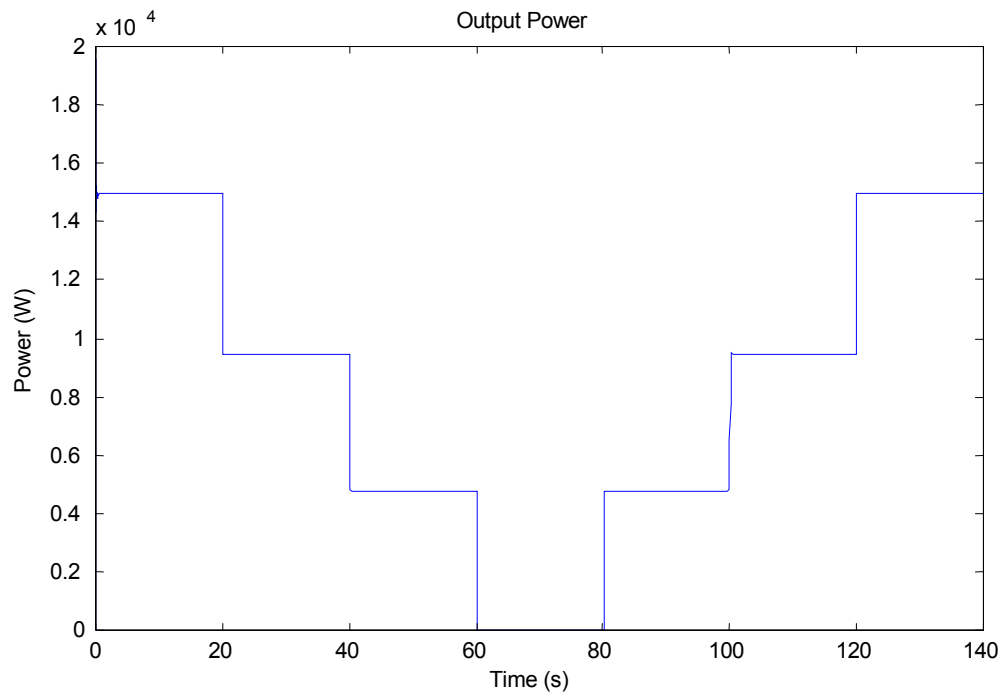


Figure 58: Output power for step changes in load

The dc voltage remains nearly fixed, with the exception of the steady state error in the controller. As the power level increases, the voltage set-point drops several volts. This drop can be controlled by the gain in the control loop. This is a desirable quantity, as the dc-dc controller is emulating a battery attached to the dc bus. This ‘droop’ is characteristic of the internal drop within the battery.

The output power appears as a near perfect step. This is required if the dc converter is to supply load in an island setting. If there was much delay in the input power/output power ratio, the loads would be inadequately supplied and any motors would stall.

A second control strategy was then investigated. This strategy allowed for a second order response to load changes. It is believed that the turbine generator will require a non-trivial amount of time to load track in island mode, and this second control scheme tried to emulate this response with enough flexibility to change the time of response.

An important point to note is that there is an allowable voltage range the dc bus may assume before the inverter will not operate properly or equipment is damaged. Either the dc bus capacitors or the input silicon to the inverter set the upper limit for voltage. The probable value is around 850 Vdc. The output voltage of the inverter determines the lower limit for the dc bus voltage. Because, in this case, 480 VRMS are required at the output, at least 680 Vdc are required. However, if vars are to be supplied by the inverter, an over-voltage of at least 5% is required. Consequently, 715 Vdc are required at the dc link. There is not a lot of tolerance, either high or low, for voltage variations on the dc bus.

Any control strategy that does not feed the dc link voltage back as a controlled quantity, subjects the dc bus to voltage variations. However, this does not imply that a conservation of energy approach could not keep the dc voltage within its allowable range. Importantly, any conservation of energy approach requires that the inverter be the master, dictating the rate of load change, and the dc-dc converter be the slave. If this is not done, whenever the dc-dc converter outputs more power than what the inverter is requiring, the dc bus voltage will increase and vice-versa. Therefore, the inverter and the dc-dc converter must communicate, probably through the dc bus voltage, the rate at which load is tracked.

The following control topology creates a master-slave relationship between the inverter and the dc-dc converter. The inverter sets the rate at which the load is tracked, and the dc-dc converter ensures that the dc bus voltage remains within tolerances, thus tracking the load at the rate set by the inverter. Figure 59 shows the controller required, with an arbitrary delay time that would be set by the Honeywell's response times in island mode. Figure 60 shows the dc bus voltage, and Figure 61 shows the output power from the dc-dc converter. Note the rise times in the power response.

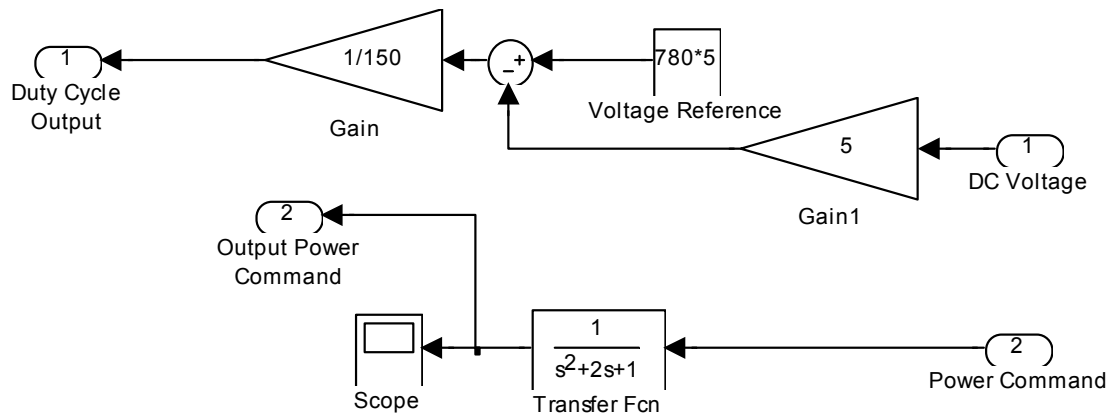


Figure 59: Augmented controller with inverter response

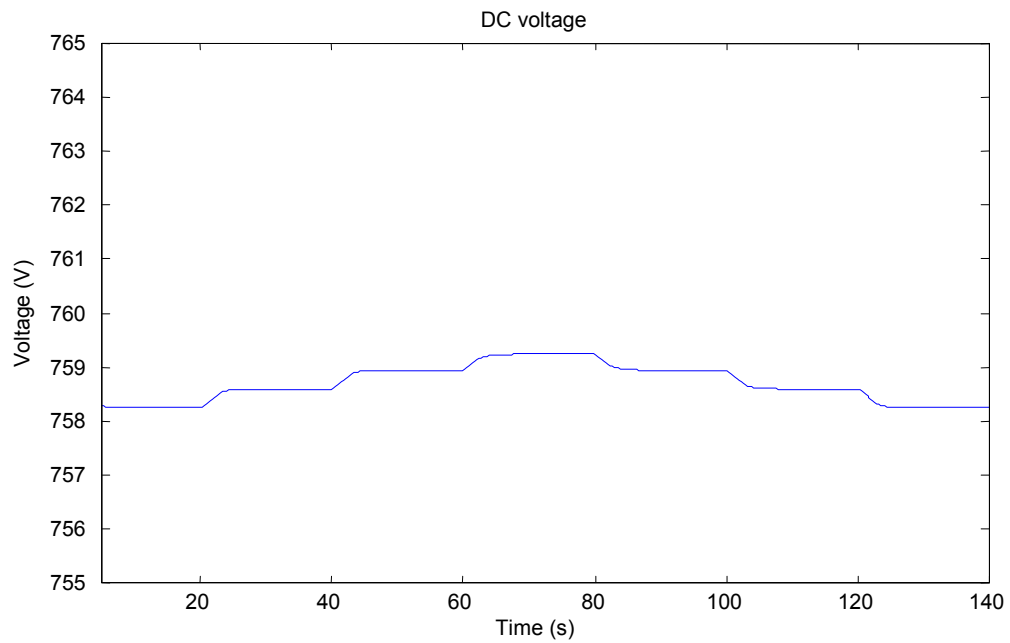


Figure 60: DC voltage of model with the augmented controller

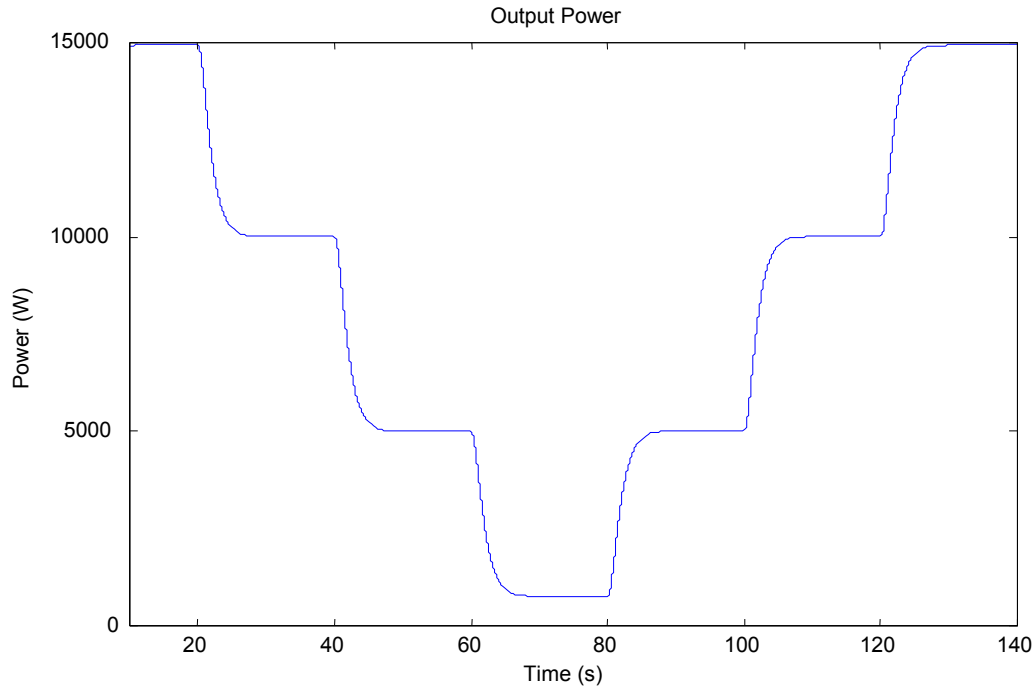


Figure 61: Output power of converter with the augmented controller

5.9 Conclusions

This section investigated the dynamic response of a Honeywell™ micro-turbine. Test data were analyzed, and the system's response to step changes in load were investigated.

Two analytic models were created in an attempt to better understand the micro-turbine response. The first model, the rotor frequency model, takes the shaft speed as input and outputs a dc link voltage. The test data obtained for the Honeywell™ micro-turbine was used to determine constants required for the model. The rotor frequency model was simulated, and responses to step changes were obtained. This model is too inhibited and neglects the rotor and turbine dynamics.

A second model was constructed, the torque input model, and responses to step changes in load were obtained. The Honeywell™ test data was used as input to ensure the tuning of the model was correct.

A controller was constructed and used in simulation as an attempt to guess what method of control is used in the Honeywell™ micro-turbine. Simulations were conducted, and responses were obtained. The overshoot in the Honeywell's response was investigated and mimicked.

A dc-dc controller was proposed to emulate the response of the Honeywell™ micro-turbine. Different control algorithms were discussed, as was as the converter's relationship with the inverter.

6 Motor Drive Inverter into MSDG Inverter Conversion

The ultimate objective of this work is to develop and verify the application of a cluster of micro-source distributed generation systems to realize industrial power distribution systems with a premium level of power quality indices. A laboratory scale-microgrid was developed for this purpose. The building block of such a laboratory-scale microgrid consists of inverters. The purpose of the proposed task is to modify a low-cost, off-the-shelf inverter designed for driving induction motors into an inverter that provides utility-grade three-phase ac voltage.

This approach aimed to save engineering effort by using commercial off-the-shelf components with minimal modifications to realize the proposed objectives. The approach was realized by a suitable design of filter elements and transformer to convert the raw inverter into utility-grade ac voltage. The design approach is presented in Section 6.1 of the report. The modified hardware design was verified using computer simulations modeling the detailed dynamic equations of the inverter. Typical results from computer simulations are presented in Section 6.2. Once the modifications were verified using computer simulations, they were implemented in the hardware and tested. The test results are shown in Section 6.3. The concluding chapter provides a summary of the results of the task.

A one-line diagram of the MSDG system is shown in Figure 62. As seen in the figure, energy storage in the form of batteries is included in the system to facilitate sourcing and sinking of power for brief periods during load transients in the network. Although electrical energy is generated from a fuel cell system in this figure, the operation of the inverter covered in this report is applicable for other micro-sources such as micro-turbines and photovoltaics. A three-phase pulse-width modulated (PWM) inverter converts electric power from dc to ac. An LC filter circuit attenuates the PWM switching ripples in the inverter output voltage. The filtered three-phase ac voltage is fed to several three-phase and single-phase loads through a Δ -Y transformer, which facilitates interface with a four-wire system.

The PWM inverter was manufactured by Allen-Bradley for motor drive application and operates on V/f control. This inverter can be utilized for distributed generation application under open-loop control by setting the reference voltage and frequency to the system requirements of 480 V and 60 Hz, respectively. The motor drive inverter is rated at 37 kW (50 hp) and operates at a switching frequency of 4 kHz. The power rating of the inverter is higher than the total demand of the loads. The inverter and LC filter together constitute a three-phase three-wire system. The LC filter output is connected to a three-phase Δ -Y (grounded) transformer to obtain a three-phase four-wire distribution system. To facilitate power distribution to loads at 208 V, the transformer is selected with a voltage ratio of 480 V/208 Y (120 V), which is a standard rating available commercially. A distribution and protection unit consisting of a thermal-magnetic circuit breaker and a three-phase ac load center is utilized to ensure the safety of the electrical equipment

under various fault conditions. Power is distributed to different classes of loads by the load center.

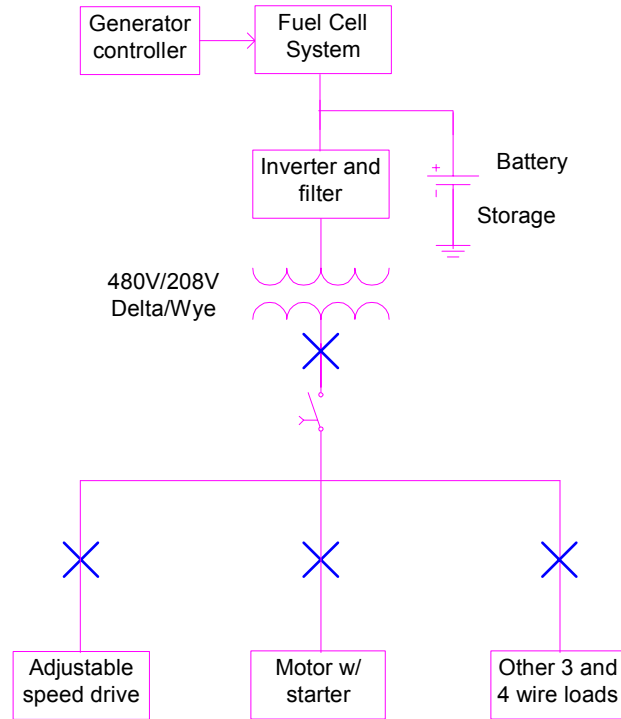


Figure 62: Block diagram of the island distributed generation system

6.1 Design of the Modified Inverter

The circuit schematic of an inverter-based island MSDG system supplying power to a three-phase four-wire load is illustrated in Figure 63. The MSDG system is rated for supplying three-phase 208 V at 60 Hz with a generation capacity of 15 kW real power and an equal amount of reactive power. As seen in the figure, the inverter is powered by a dc source that represents the whole system on the dc side including micro-source and energy storage. The important components of the island distributed generation system shown in the figure are the inverter, LC filter and Δ -Y transformer. This chapter discusses the features of the inverter, the design of the LC filter and the transformer.

6.1.1 Inverter Features

The MSDG system is designed for a maximum generation capacity of 15 kW real power and an equal amount of reactive power. The devices of the inverter have to be rated for this power level. Also, because it is a utility application, the motor-drive inverter was overrated for 37 kW (i.e., 50 hp) to withstand possible over-voltages and over-currents that occur under fault conditions. A common dc-bus configuration model of Allen-Bradley drives was chosen for this purpose.

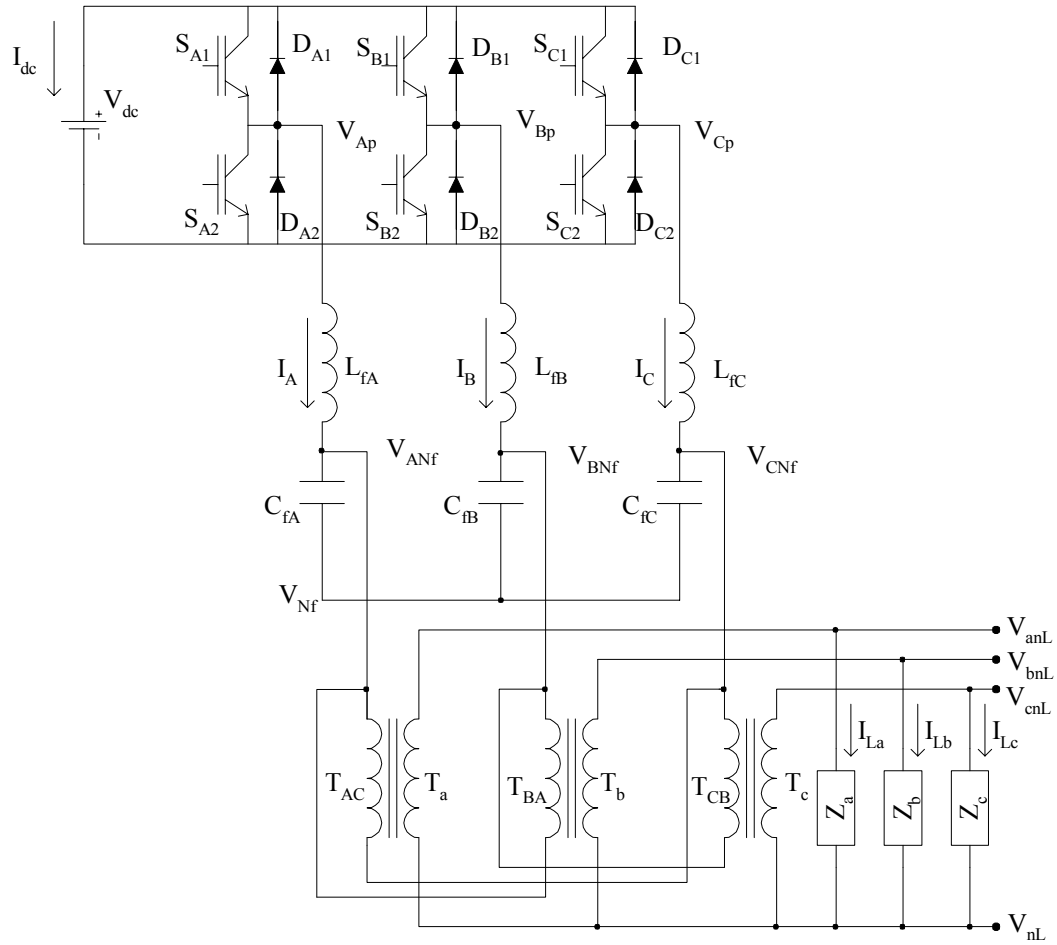


Figure 63: Circuit schematic of the inverter-based island micro-source distributed generation system

The desired output ac voltage of the inverter is 480 V (RMS). The nameplate details of the motor drive inverter are [22]:

Manufacturer:	Allen-Bradley (Division of Rockwell Automation)
Catalog #:	1336S-W050-AN-EN-HA2-L6
Serial #:	1JAN5RL9
Series:	B
DC Input:	Common bus configuration
Voltage:	675 – 800 A
Current:	63 A
AC Output:	3-phase, 57 kVA
Voltage:	0 – 575 V
Current:	57.2 A
Power Rating:	50 hp, 37 kW

The Allen-Bradley inverter operates on V/f control to drive an induction motor. Voltage and frequency settings of the inverter are made for the system requirements of 480 V and 60 Hz, respectively. However, the inverter works on ramp start as it operates on V/f control. Loads that are sensitive to the frequency are disconnected during this initial ramping phase until the inverter achieves the steady-state values of voltage and frequency. The switching devices used in the inverter are insulated gate bipolar transistors (IGBTs), and they are switched using sine PWM with third harmonic injection. The maximum allowable switching frequency of the inverter is 4 kHz at the rated load. To reduce the size of filter components for the inverter, the switching frequency of the inverter is set to its maximum value. The dc voltage of the inverter is 750 Vdc, which is obtained from two 500-V, 10-kW programmable dc power supplies (Magna-Power Electronics® PQ500-20) connected in series. They will be retrofitted with the power source emulator at a future point when it becomes available.

6.1.2 Filter Selection

The values of LC filter components are selected to attenuate the switching ripples of the PWM inverter. Figure 64 illustrates a single-phase equivalent circuit of the inverter voltage feeding a resistive load through an LC filter and transformer. The load terminal voltage to inverter voltage transfer function of the filter is:

$$\frac{V_L(s)}{V_{inv}(s)} = \frac{R_L}{(L_f s + R_f) + [L_t s + (R_t + R_L)] (L_f C_f s^2 + R_f C_f s + 1)} \quad (30)$$

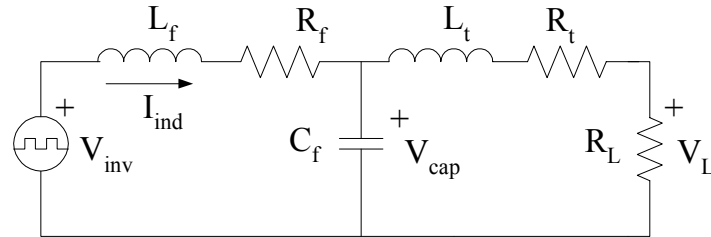


Figure 64: Single-phase equivalent circuit of the LC filter for the PWM inverter

Figure 65 gives bode magnitude plot of the transfer function in Equation 29 for typical values of circuit components. The corner frequency of the LC filter has to be chosen to filter the PWM switching ripples of the inverter and pass the fundamental frequency component without attenuation. The expression for corner frequency (f_c) is:

$$f_c = \frac{1}{2\pi\sqrt{L_f C_f}} \quad (31)$$

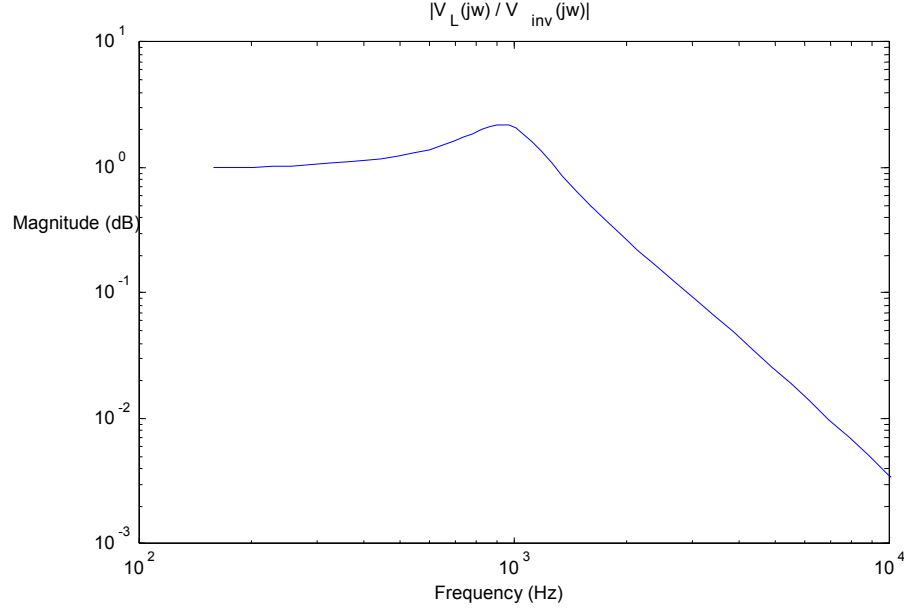


Figure 65: Bode plot of $\left| \frac{V_L(s)}{V_{inv}(s)} \right|$

Considerations in the design of an LC filter also include the loads connected across the filter capacitor. The circuit schematic of an LC filter connected to a nonlinear current source at the capacitor terminals is shown in Figure 66. The effect of the nonlinear load current on the filter inductor current and the filter capacitor voltage are given by the transfer functions:

$$\frac{I_{ind}(s)}{I_L(s)} = \frac{1}{L_f C_f s^2 + R_f C_f s + 1} \quad (32)$$

$$\frac{V_{cap}(s)}{I_L(s)} = \frac{L_f s + R_f}{L_f C_f s^2 + R_f C_f s + 1} \quad (33)$$

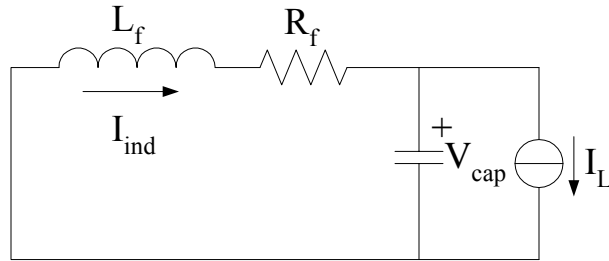


Figure 66: Single-phase equivalent circuit of the LC filter for a nonlinear load that is represented as a current source

The bode magnitude plots of transfer functions given in Equations 31 and 32 are plotted in Figure 67. As seen in the figure, there exists parallel resonance at the corner frequency of the LC filter. At this frequency, the inductor current and the capacitor voltage get amplified. Hence, the corner frequency of the LC filter is to be designed such that it is not near the dominant harmonics generated by nonlinear loads.

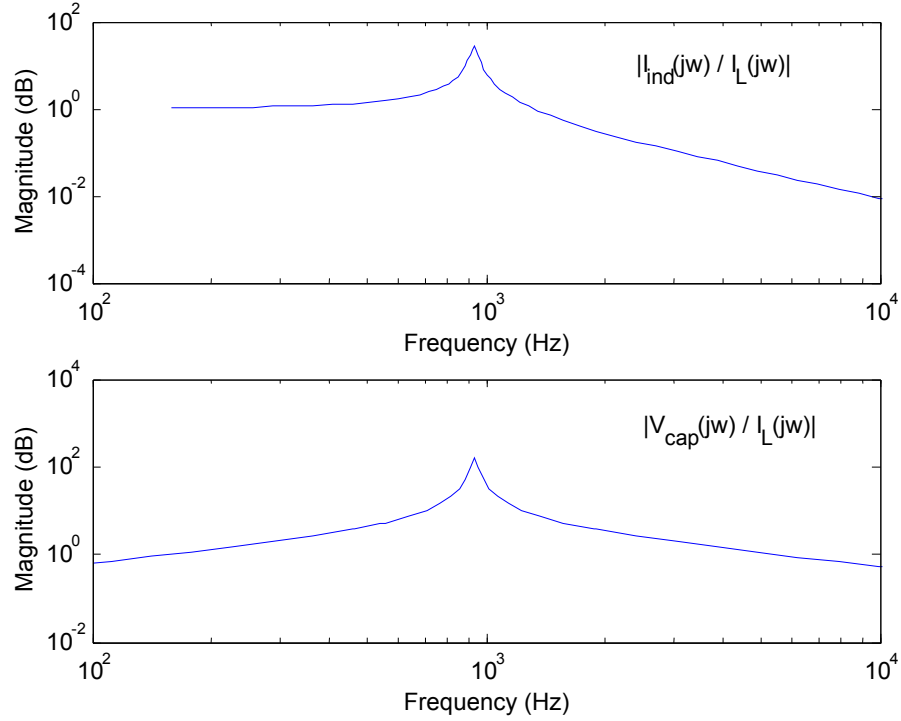


Figure 67: Bode plots of $\left| \frac{I_{ind}(s)}{I_L(s)} \right|$ and $\left| \frac{V_{cap}(s)}{I_L(s)} \right|$

Sources of nonlinear current in the MSDG system include the magnetizing current of the transformer [19] and any nonlinear loads connected to the secondary of the transformer. The dominant harmonics generated by several nonlinear loads as well as the transformer (magnetizing current) are 3rd, 5th and 7th harmonics. Because the transformer is a Δ -Y transformer, it is assumed that the triplen (3rd and its odd multiples) harmonic currents are restricted to its secondary side, i.e., are the circulating currents in the delta winding. Hence the load current harmonics applied across the filter capacitor are 5th, 7th, 11th, 13th etc. ($6n \pm 1$, $n = 1, 2, 3, \dots$). Among these harmonics, the dominant ones are 5th and 7th harmonics.

Thus, it is necessary to design the LC filter with a corner frequency between dominant (5th and 7th) harmonics and the switching frequency (4 kHz). The corner frequency is chosen to be 933 Hz. Several combinations of L_f s and C_f s can achieve this corner

frequency. For a particular load current, a larger value of L_f would require a bulky inductor. Modern compact ac capacitors with relatively high capacitance value are available commercially. Another advantage of the filter capacitors is they will contribute to the reactive power requirements of the inductive loads. The values of L_f and C_f are chosen such that the overall filter size is optimized for a particular corner frequency. The designed values of filter parameters for the MSDG system are tabulated in Table 3.

Table 3: LC circuit parameters

Parameter	Value
f_c	933 Hz
L_f	0.97 mH
R_f	0.21 Ω
C_f	30 μ F

6.1.3 Transformer Selection

The MSDG system is rated to supply 15 kW real power and an equal amount of reactive power to different classes of loads, including linear and nonlinear loads. A Δ -Y transformer is suitable for connecting both single- and three-phase loads to the distribution system. Because different loads may be connected to different phases of the system, the loads can become unbalanced in the three phases. Similarly, imbalance in the system is also observed under fault conditions. The windings of the transformer must be capable of carrying the net current of the loads. Because the neutral current is high for single-phase linear and nonlinear loads, the neutral (ground) wires on the secondary side of the transformer are rated for the full load current. This neutral current gets transformed as the circulating current in the delta (primary) windings of the transformer. Also, the loads are rated for a voltage of 208 Y/120 V. Hence, a Δ -Y transformer rated at 45 kVA and at a voltage ratio of 480 V (Δ) : 208 (Y)/120 V that is commercially available is used for this purpose. The percent impedance is 2.55% at a base power of 21.21 kVA. The transformer windings are connected such that phase 'a' voltage on its secondary side lags phase 'A' voltage on its primary side by 30°. The specifications of the transformer are given below [24]:

Manufacturer:	General Electric Company
Catalog #:	9T23B3873
Rating:	3-phase – 60 Hz – 45 kVA 480 delta +2, -4 (2.4% taps) – 208 Y/120
Temperature Rise:	150°C
Insulation System:	220°C
Sound Level:	Average 45 dB

Dielectric Testing:

A) Induce test at twice the rated voltage at 400 Hz per ANSI C89.2 and NEMA ST-20 standards

B) Highpot tests:

1) High voltage windings to low voltage windings and ground – 4,000 V
60 Hz 60 s

Low voltage windings to high voltage windings and ground – 2,500 V 60 Hz 60 s

Other Production Tests:

A) Open circuit voltage – primary 505/491/480/470/456/445/431 secondary
208Y/120

B) Polarity – tested in accordance with ANSI C89.2 and NEMA ST-20
standards

Loss Data:

No load loss (core losses) 388 W at 100% voltage

Impedance loss (coil loss) 1,744 W at 170°C reference temperature

Total losses 2,132 W at 170°C reference temperature

Efficiency at 1.0 Power Factor, 170 °C Reference Temperature:

<u>Load</u>	<u>% Efficiency</u>
25%	95.7
50%	96.4
75%	96.1
100%	95.6

Impedance at 170°C Reference Temperature:

% R	3.8
% X	3.8
% Z	5.4

Regulation at 170°C Reference Temperature:

<u>Power Factor</u>	<u>% Regulation</u>
1.0	3.8
0.8	5.3

Jumper Tap Connections:

Tap	Volts
1	502
2	491
3	480
4	470
5	456
6	445
7	434

Weight: 365 lbs

The transformer secondary is connected to a three-phase ac load center (Cat. #QO124L100G) that has 24 poles for various three-wire and four-wire loads. A main circuit breaker with shunt trip (Cat. #KAL3G1001021) is provided before the load center for disconnecting the power supply in the event of large unbalance ($> 10\%$) in the terminal voltage, phase-loss, over-voltage or under-voltage.

6.2 Simulation Waveforms for Modified Inverter

Digital simulation of the open-loop control of MSDG system is carried out on MATLAB Simulink™ software. The circuit schematic of the MSDG system that is simulated is illustrated in Figure 68. As seen in the figure, the dc-bus voltage of the inverter is assumed to be constant. This is owing to the presence of energy storage devices such as batteries. The inverter switching is based on space vector pulse width modulation (SVPWM) at a switching frequency of 4 kHz. The MSDG system is divided into several modules called subsystems that denote its major components. These subsystems are space-vector pulse-width modulator, inverter, LC filter, transformer and load. Each subsystem contains linear differential equations that describe its functionality. Each subsystem may be further subdivided into individual phases. Because the inverter here is a three-legged inverter, the circuit on the primary side of the Δ -Y transformer is a three-phase three-wire circuit. A pole-throw model simulates the inverter and the LC filter for each phase [18]. The potential of neutral with respect to the negative dc rail is utilized to obtain the phase-neutral voltages of the filter capacitors on three phases. The equivalent circuit, shown in Figure 69, represents the Δ -Y transformer. The circuit parameters considered for simulation are shown in Table 4.

Table 4: Circuit parameters for simulation studies

Parameter	Value
V_{dc}	750 V
V_{AC} (nominal)	480 V
V_{ac} (nominal)	208 V
L_f	0.97 mH
R_f	0.21 Ω
C_f	30 μ F
L_{tAC}	1.5 mH
R_{tAC}	0.58 Ω

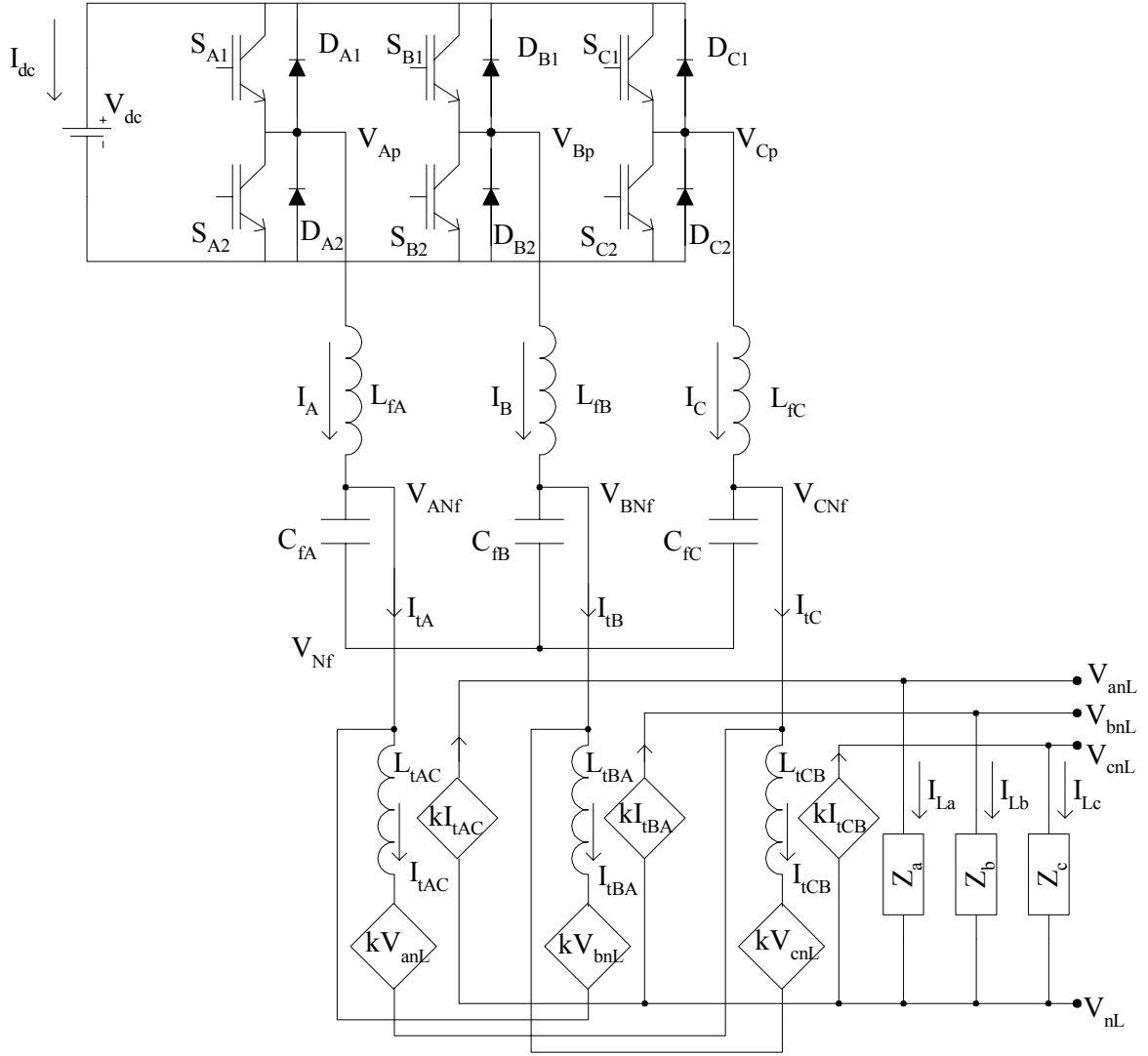


Figure 68: Circuit schematic of the MSDG system for simulation in MATLAB Simulink™

The results of simulation for open-loop control of a three-phase balanced inductive load are shown in Figures 69 through 72. The power factor of the load is 0.93 (lagging). The load parameters (series R_L and L_L) that make up Z_x (x-phase) are given in Table 5.

Table 5: Load parameters for the simulation studies

Parameter	Value
R_L	4 Ω
L_L	4.1 mH

Figure 69 gives the phase-to-neutral voltages (V_{anL} and V_{bnL}) and the load currents (I_{La} and I_{Lb}) for this balanced inductive load. Figures 70 and 71 give the phasor diagrams of the three-phase voltages and currents (in pu) at the load terminals. The filter inductor current in the three phases is shown in Figure 72. As seen in these figures, the magnitude of the load voltage drops as the load is increased. However, the voltages and the currents are balanced in three phases. The voltage at the load terminals drops to 0.98 pu for a current of 0.47 pu at a power factor of 0.93 (lagging). The average three-phase power drawn by the load is 9.04 kW.

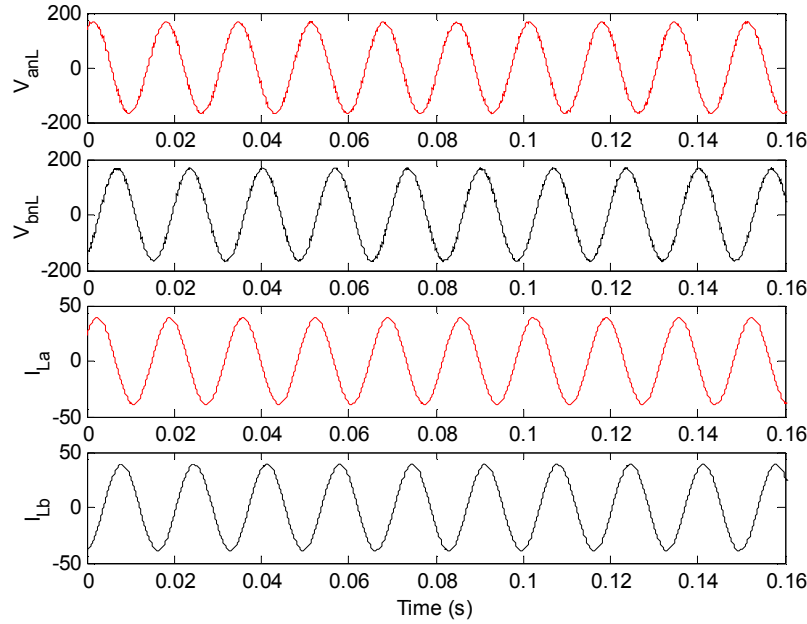


Figure 69: Load terminal voltages (top two) and load currents (bottom two)

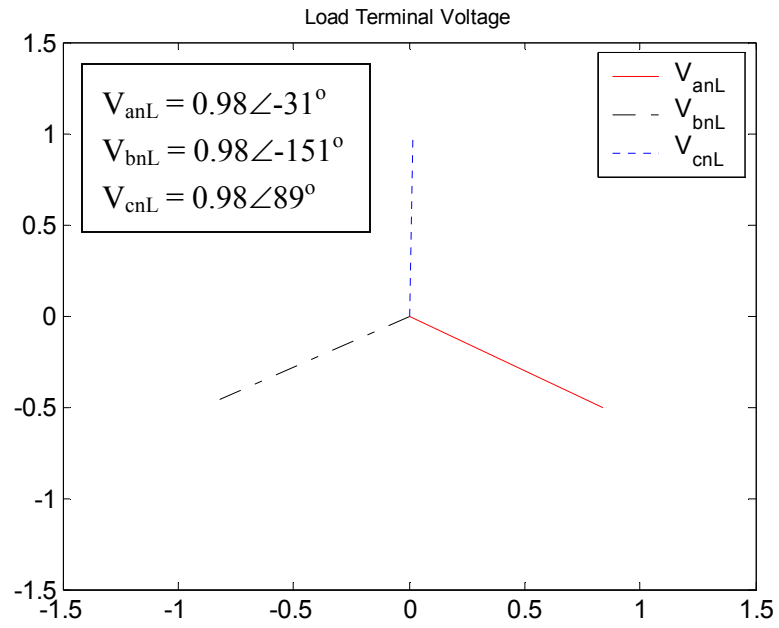


Figure 70: Load terminal voltage phasor diagram (in pu)

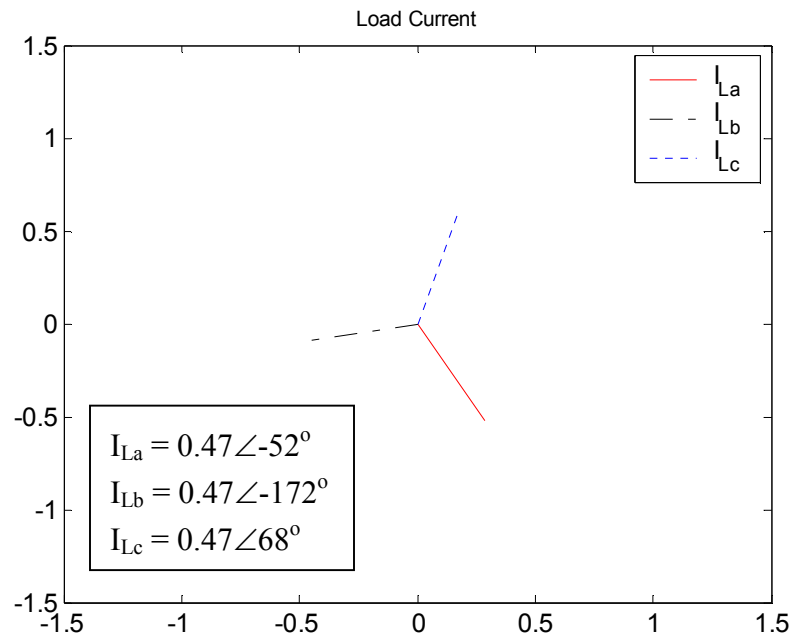


Figure 71: Load current phasor diagram (in pu)

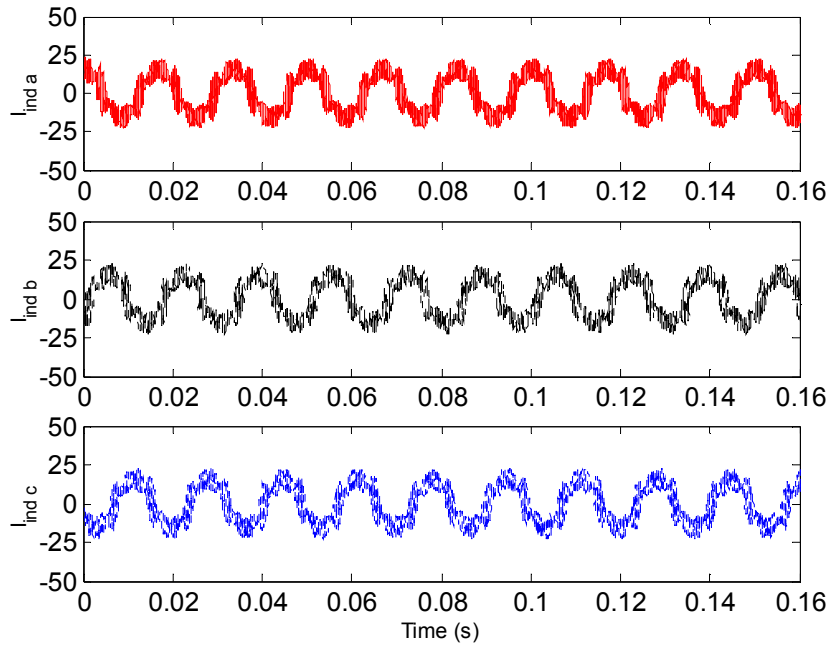
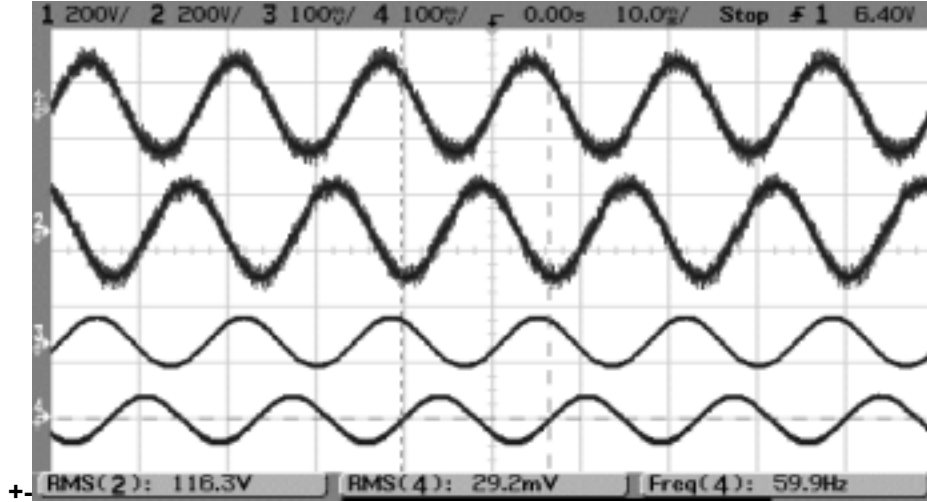


Figure 72: Filter inductor current in three phases

6.3 Testing of the Modified Inverter

The experimental hardware setup is based on an Allen-Bradley motor-drive inverter that is modified for utility application. Dc supply for the inverter is obtained from two Magna-Power Electronics® dc power supplies (PQ 500-20) connected in series. Each of these supplies can provide a maximum of 500 Vdc at 20 A. The inverter-switching scheme is based on Sine PWM with third-harmonic injection. An LC circuit filters the PWM switching ripples in the inverter output voltage. The LC filter output voltage is fed to the primary of a 45-kVA Δ -Y transformer. A series RL load is connected to the secondary of the transformer through an ac load center. The circuit and load parameters are the same as in Tables 4 and 5 respectively.

The snapshots of the waveforms illustrating experimental results for a balanced inductive load are shown in Figures 73 and 74. The voltages and the currents for two phases at the load terminals are given in Figure 73. As seen in the figure, the load terminal voltage drops 114.75 V when loaded to 29.27 A at a power factor of 0.94 (lagging), on open-loop control. Figure 74 shows the filter capacitor voltages and filter inductor currents in two phases.



**Figure 73: Load terminal voltages – V_{anL} & V_{bnL} (top two)
and load currents – I_{La} & I_{Lb} (bottom two)**
Current amplifier gain is 10 A/10 mV.

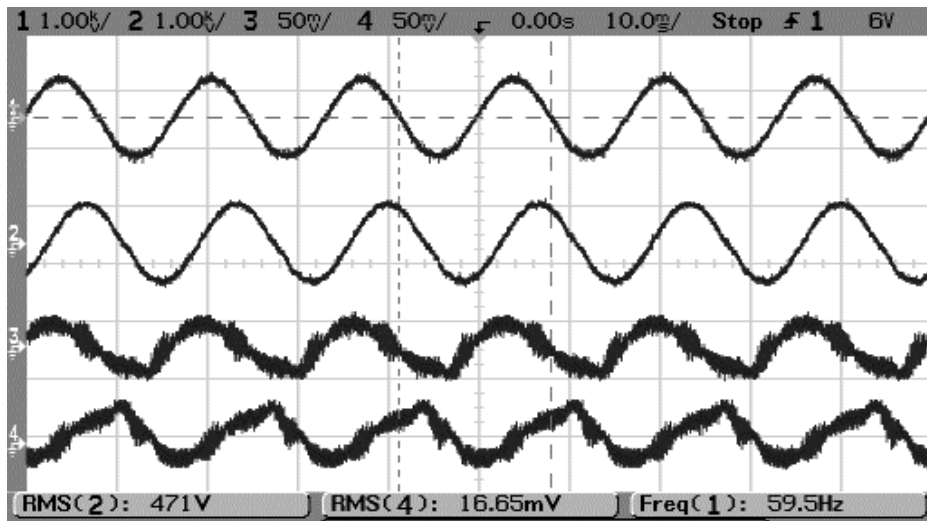


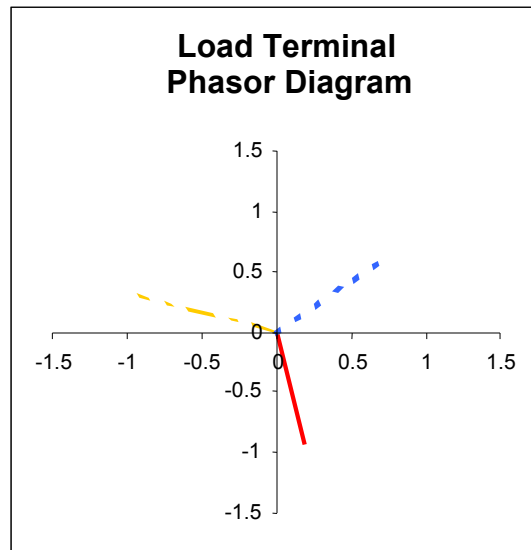
**Figure 74: Filter capacitor voltages – V_{ACf} & V_{BCf} (top two)
and filter inductor currents – $I_{ind a}$ & $I_{ind b}$ (bottom two)**
Current amplifier gain is 10 A/10 mV.

It is observed that the filter inductor current is more distorted in the experiment than in simulation. Although the filter inductor current in simulation contains predominantly the fundamental frequency and the LC corner frequency components, the same quantity in the experiment contains some low frequency harmonics as well. This is because the simulation model does not consider the nonideal effects of the transformer, such as saturation. The average three-phase power output at the load terminals that is measured by a power system analyzer is 8.904 kW.

6.3.1 Measurements from Power Analyzer

R_L	3.9 Ω
L_L	4.1 mH
P_input	9.55 kW (Human Interface Module – AB drive)
P_output	8.904 kW (RisACE2000™ power analyzer)
I_load	26.38 A
V_load	204.8 V
Power factor	0.95 (lagging)

The time-domain waveform information shown above in Figures 73 and 74 is also collected in the form of a Microsoft Excel™ file. This data is processed to obtain the phasor diagrams of the voltage and current. Figures 75 and 76 illustrate the phasor diagrams of the load terminal voltage and the load current respectively. It is observed that the magnitudes of voltage and current phasors at the load terminals are almost equal in three phases owing to the balanced nature of loads. The drop in voltage at the load terminal is about 5% under loaded conditions.

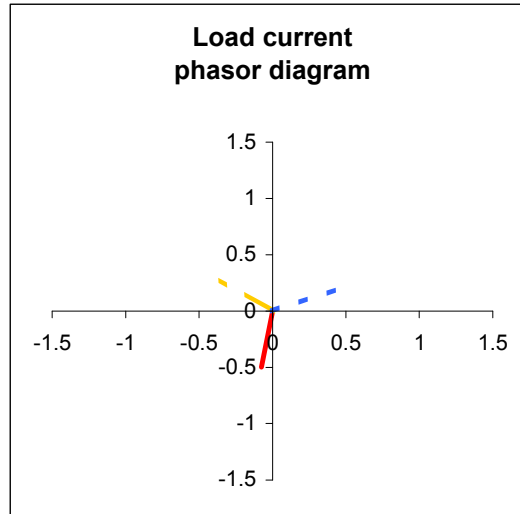


$$V_a = 0.9449 \angle -78.5398^\circ$$

$$V_b = 0.9641 \angle 161.8121^\circ$$

$$V_c = 0.9597 \angle 40.6434^\circ$$

Figure 75: Phasor diagram of the load terminal voltages



$$I_a = .5043 \angle -98.56^\circ$$

$$I_b = .485 \angle 142.22^\circ$$

$$I_c = .5008 \angle 23.745^\circ$$

Figure 76: Phasor diagram of the load currents

A photograph of the modified inverter with the LC filter is shown in Figure 77.



Figure 77: Photograph of inverter incorporating LC filter and transformer

7 Island-Mode Micro-Source Distributed Generation System Studies

Distributed generation involves the allocation of small electrical generation sources at the load centers to optimally utilize resources. It can be used for providing energy stabilization, ride-through and dispatchability [6]. MSDG systems consist of micro-sources such as fuel cells and micro-turbines with power electronic converters to interface with the load [3]. This project is focused on enabling MSDG systems to meet the power quality demands of sensitive loads. MSDG systems can improve the reliability of power supply to sensitive loads by connecting alongside the main grid supply. Project tasks have focused on developing appropriate control technologies and demonstrating them on a laboratory-scale microgrid. In the first phase of the project, activities focused on developing necessary infrastructure for a microgrid, modifications necessary for converting a motor drive inverter into one that can provide utility-grade voltage, development of a power source emulator and study of energy storage systems. Investigation results on battery energy storage and modifications of a motor drive inverter into a MSDG inverter were presented earlier in this report. This chapter presents the results from the benchmark testing of the MSDG inverter developed feeding a complex set of loads.

A one-line diagram of the MSDG system functioning in island mode of operation is shown in Figure 62 (Ref. Chapter 6). As seen in the figure, different classes of single- and three-phase loads are provided with reliable power by the MSDG system. The circuit schematic of an inverter-based island MSDG system, providing power to a three-phase four-wire load, is illustrated in Figure 63 (Ref. Chapter 6). It is assumed that sufficient energy storage is available at the dc bus of the inverter so that there is decoupling between the operation of the inverter and micro-source. From that fact, the dc bus is represented as a simple battery in Figure 63. Under the energy storage availability assumption, the major components of the island distributed generation system as shown in the figure are the inverter, LC filter and Δ -Y transformer. The three-phase PWM inverter converts electric power from dc to ac. The LC filter circuit attenuates the PWM switching ripples in the inverter output voltage. The filtered three-phase ac voltage is fed to several three-phase and single-phase loads through a Δ -Y transformer, which facilitates interface with a four-wire system. Hence, project activities have focused on the development of an inverter hardware platform that can be integrated to form a laboratory-scale microgrid that incorporates the control functions that are being developed under the project.

This chapter deals with the behavior of an island mode MSDG system supplying power to different classes of loads. The circuit parameters of the system are as specified in Table 6 (reproduced from Table 4 in Chapter 6). The various loads dealt include linear passive loads such as resistive, inductive and capacitive loads, as well as nonlinear loads such as rectifiers. Performance of the system under balanced as well as unbalanced load conditions is examined. Section 7.1 describes the analysis of an MSDG system in island

mode for different classes of loads. Results of theoretical analysis made at fundamental frequency are presented. This analysis is conducted in Mathcad™ software. Load regulation characteristics of this analysis are compared with those obtained from detailed time-domain simulation using MATLAB Simulink™ software. In Section 7.2, elaborate simulation waveforms are illustrated under different load conditions. Section 7.3 deals with the experimental results and discussion. Finally, Section 7.4 gives concluding remarks.

Table 6: Circuit parameters for the island-mode MSDG system

Parameter	Value
V_{dc}	750 V
V_{AC} (nominal)	480 V
V_{ac} (nominal)	208 V
L_f	0.97 mH
R_f	0.21 Ω
C_f	30 μ F
L_{tAC}	1.5 mH
R_{tAC}	0.58 Ω

7.1 Analytical Modeling of the Island Mode MSDG System

In this section, an island mode MSDG system is analytically modeled for predicting the performance of the system under various load conditions. Characteristics of the system such as terminal voltage, regulation and load features are investigated. Linear loads at different power levels and power factors are dealt in this analysis. The scope of operation of the system to meet the demands of different classes of loads is determined.

7.1.1 Balanced Three-Phase Analysis

In the circuit schematic of the MSDG system illustrated in Figure 63, the micro-source and the PWM inverter can be replaced by an ideal three-phase voltage source for the purpose of analysis.

A balanced three-phase analysis is conducted using the single-phase equivalent circuit of the island mode distributed generation system as given in Figure 78. In this figure, the leakage impedance Z_t along with a complex gain (\overline{K}) represents single-phase equivalent circuit of the Δ -Y transformer.

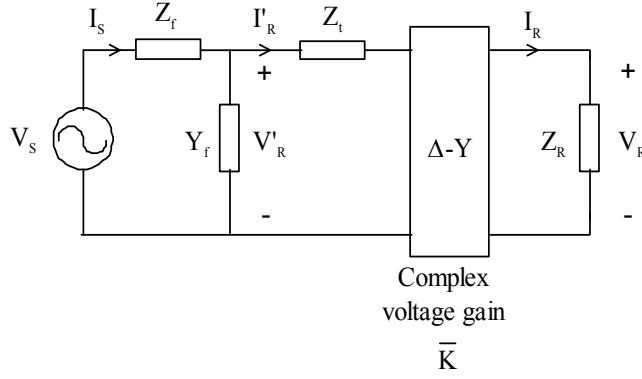


Figure 78: Single-phase equivalent circuit of the MSDG system

Let the inverter voltage and current be represented as V_S and I_S and the filter capacitor voltage and transformer primary current be V_R' and I_R' . Then, the matrix equation for LC filter circuit is given by [16]:

$$\begin{bmatrix} V_S \\ I_S \end{bmatrix} = \begin{bmatrix} (1+Z_f Y_f) & Z_f \\ Y_f & 1 \end{bmatrix} \begin{bmatrix} V_R' \\ I_R' \end{bmatrix} \quad (34)$$

where Z_f and Y_f are the filter inductor impedance and filter capacitor admittance respectively that are determined as:

$$Z_f = R_f + j \omega L_f \quad (35)$$

$$Y_f = j \omega C_f \quad (36)$$

If the transformer secondary voltage and current are represented as V_R and I_R , the matrix equation for the Δ -Y transformer including the effects of the leakage impedance is:

$$\begin{bmatrix} V_R' \\ I_R' \end{bmatrix} = \begin{bmatrix} 1 & Z_t \\ 0 & 1 \end{bmatrix} \begin{bmatrix} \frac{1}{\bar{K}} & 0 \\ 0 & \bar{K}^* \end{bmatrix} \begin{bmatrix} V_R \\ I_R \end{bmatrix} \quad (37)$$

where:

$$Z_t = \frac{R_t + j \omega L_t}{3} \quad (38)$$

$$\bar{K} = \sqrt{3} n e^{-j\pi/6} \quad (39)$$

and 'n' is the transformer turns-ratio and \bar{K}^* is the conjugate of \bar{K} .

Combining Equations 34 and 37, the overall matrix equation can be written as:

$$\begin{bmatrix} V_S \\ I_S \end{bmatrix} = T_1 T_2 \begin{bmatrix} V_R \\ I_R \end{bmatrix} \quad (40)$$

where:

$$T_1 = \begin{bmatrix} (1+Z_f Y_f) & Z_f \\ Y_f & 1 \end{bmatrix} \quad (41)$$

and

$$T_2 = \begin{bmatrix} 1 & Z_t \\ 0 & 1 \end{bmatrix} \begin{bmatrix} \frac{1}{K} & 0 \\ 0 & \overline{K}^* \end{bmatrix} \quad (42)$$

The matrix equation in Equation 40 can also be written as:

$$\begin{bmatrix} V_R \\ I_R \end{bmatrix} = T_2^{-1} T_1^{-1} \begin{bmatrix} V_S \\ I_S \end{bmatrix} \quad (43)$$

If the load at the receiving end is a passive load of impedance, $Z_R = R_R + j X_R$, then:

$$V_R = Z_R I_R \quad (44)$$

The voltage and current at the receiving end can be determined if the sending end voltage is known by solving Equations 43 and 44.

The complex power delivered to the load is determined by:

$$S_R = 3 V_R I_R^* \quad (45)$$

The real and reactive powers (i.e., P_R and Q_R) delivered to the load are determined as:

$$P_R = 3 \operatorname{Re} \{ V_R I_R^* \} \quad (46)$$

$$Q_R = 3 \operatorname{Im} \{ V_R I_R^* \} \quad (47)$$

From Equations 44, 46 and 47, the expressions for P_R and Q_R can be simplified to:

$$P_R = 3 |I_R|^2 R_R \quad (48)$$

$$Q_R = 3 |I_R|^2 X_R \quad (49)$$

Assuming the sending end to be at nominal voltage, the real and reactive powers delivered to the receiving end at full-load are plotted in Figures 79 and 80, respectively, as a function of the power factor. As seen in Figure 79, the real power drawn at full load is maximum for unity power factor, and it decreases to zero gradationally as the power factor is reduced. From Figure 80, it is observed that the reactive power drawn at full-load for different power factors follows a sinusoidal curve. The MSDG system is designed to deliver the required real and reactive power. Because the real and reactive

power curves are sinusoidal in nature, it can be derived that circle diagrams characterize the complex power curves. It must be noted that the negative offset in the reactive power curve is due to additional reactive var generation by the filter capacitor.

The real power capacity of the MSDG system is limited by the capacity of the micro-source employed, such as a micro-turbine or a fuel cell. The kVA rating of the inverter is at least equal to this real power rating. That being the case, the inverter would not be able to supply any reactive power when providing peak real power. Notwithstanding, a fixed reactive power generation capability under all load conditions is possible by rating the inverter on the higher side. To be able to supply real and reactive power of 15 kW and 15 kVAr simultaneously, the MSDG system is rated at 22.5 kVA. However, it is to be noted that a real power capacity of more than 15 kW is unachievable because of the limitations of the capacity micro-source.

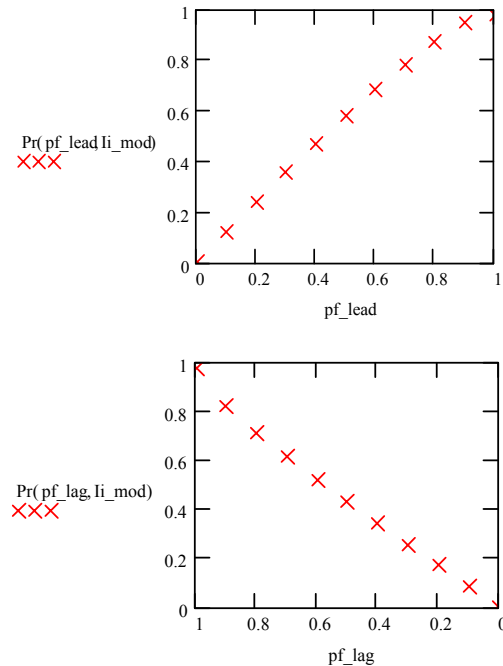


Figure 79: Real power (in pu) delivered at full load as a function of power factor

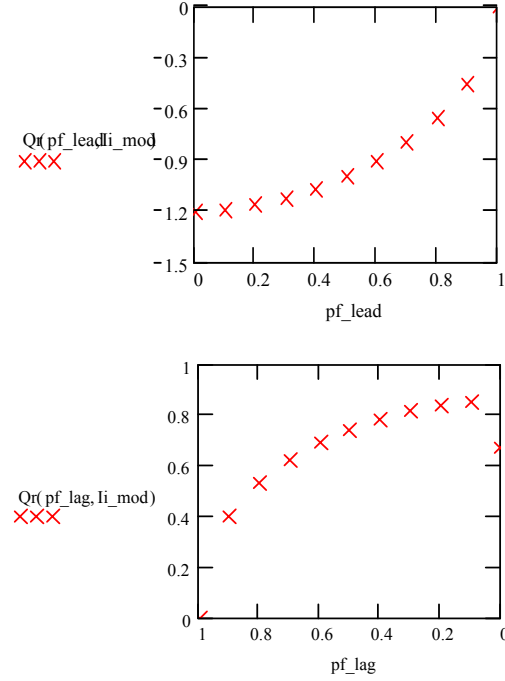


Figure 80: Reactive power (in pu) delivered at full load as a function of power factor

The voltage at the transformer secondary terminals experiences variation with changes in load. Voltage regulation is the change in the transformer secondary voltage between no-load and full-load conditions. It varies with power factor and so is quoted as a percent or per-unit of rated voltage at a given power factor. Expressed as a fraction, the regulation is

$$\varepsilon = \frac{E_{tR} - V_R}{V_R} \quad (50)$$

Voltage regulation has been dealt with in literature with reference to transformers and generators [17]. It is strongly influenced by the load power factor. For a given load level and power factor, the regulation of a transformer depends on its resistance and leakage reactance. In the case of a generator also, regulation is caused by the voltage drop across resistance and leakage reactance and, more particularly, its armature reaction. In the case of an MSDG system, the resistance and reactance of the LC filter plus transformer are the factors that influence the regulation at a particular load power factor. The regulation curves for the island mode MSDG system for leading and lagging power factor loads are displayed in Figures 81 and 82, respectively.

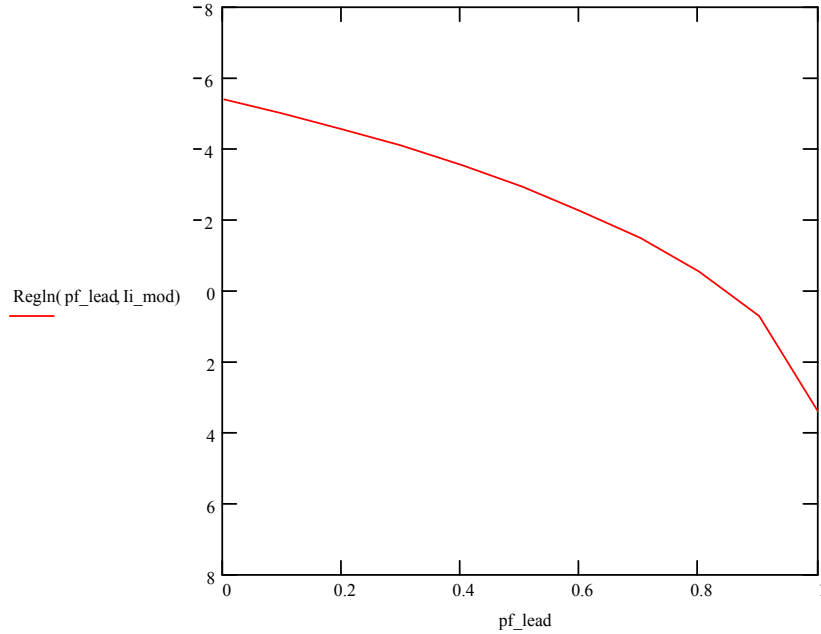


Figure 81: Voltage regulation curve for leading power factor loads for an island mode MSDG system

These curves represent the percentage full-load regulation at the secondary terminals of the Δ -Y transformer at different power factors. In Figures 81 and 82, power factor of the load is gradually varied from zero (leading) to unity power factor and then to zero (lagging). For that reason, the range of leading power factors is from 0 to 1 while that of lagging power factors is from 1 to 0. In the figures, a negative regulation indicates that the terminal voltage at full load is greater than that at no load. Similarly, a positive regulation denotes that the terminal voltage falls with increase in load. As seen in Figures 81 and 82, the regulation is negative for loads of power factor less than 0.82 (leading), and it is positive for all other values. Accordingly, for unity and lagging power factors, there is always a voltage drop with load, but for certain leading power factor loads, the full-load regulation is zero, i.e., the terminal voltage is the same for full- and no-load conditions. The difference between the regulation curves of a transformer and an MSDG system is due to the additional LC filter circuit in the MSDG system. Because regulation is a numeric quantity, the regulation produced by two impedances connected in series can be combined algebraically [17].

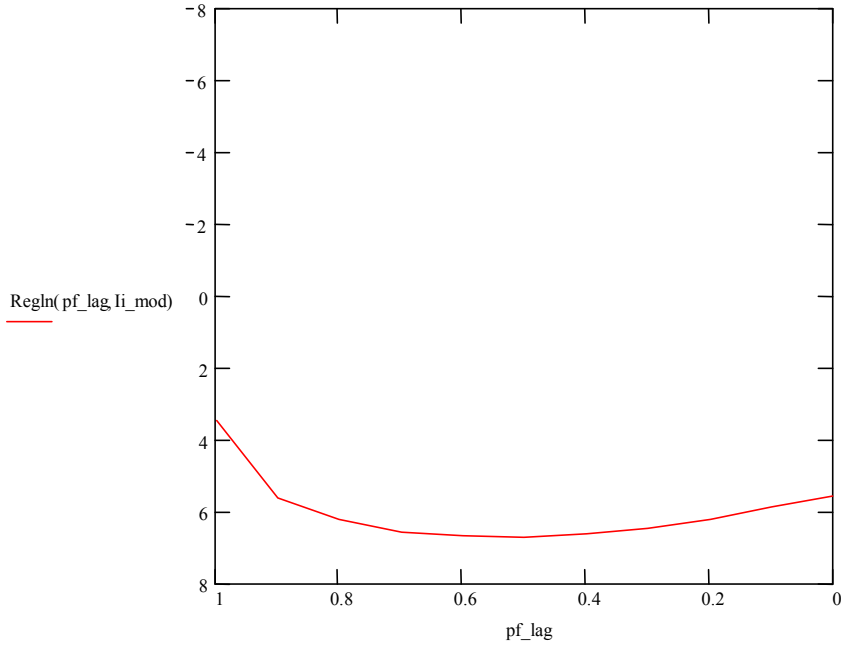


Figure 82: Voltage regulation curve for leading power factor loads for an island mode MSDG system

The load characteristics of the MSDG system are shown in Figures 83 and 84 for leading and lagging power factors, respectively. These curves indicate the terminal voltage of the transformer (expressed in percent of the no-load voltage) as a function of the full-load current (expressed in pu). It is assumed that the inverter outputs a voltage of constant magnitude of 1.0 pu. As seen in Figures 83 and 84, the terminal voltage curves for zero power factor (both leading and lagging) are almost straight lines. This is because of the low resistance of the LC filter and transformer as compared with its reactance. In this case, the slope of the straight line is equal in magnitude to the reactance of the filter and transformer at the fundamental frequency. The load curves for all other power factors have an elliptic solution for the terminal voltage because of the quadratic nature of the system equations. Another observation made from these curves is the short-circuit condition of the system. A zero terminal voltage represents this state, and the load current at this condition is called short-circuit current. This instance occurs when the load impedance is zero. From Figures 83 and 84, it is observed that the short-circuit current of the MSDG system is about 15 pu.

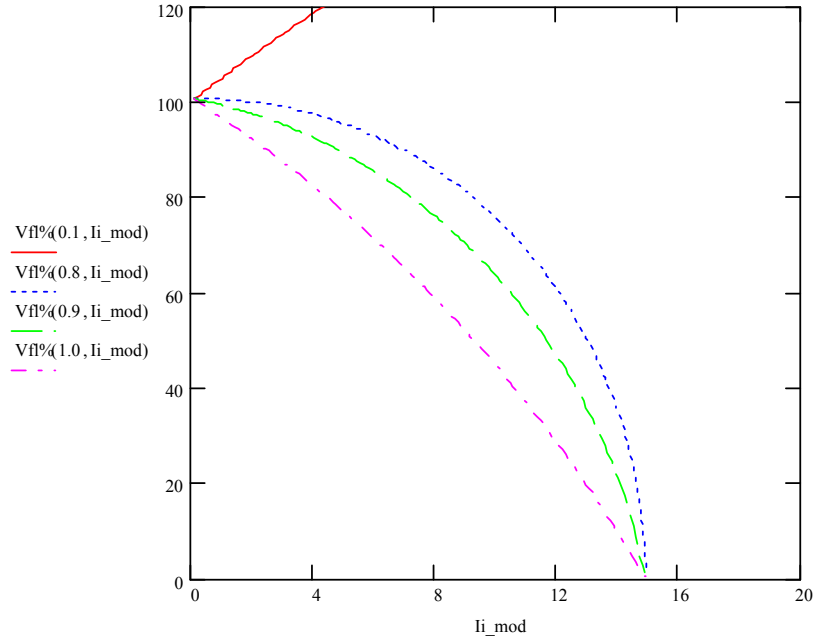


Figure 83: Load characteristics of an MSDG system for leading power factors

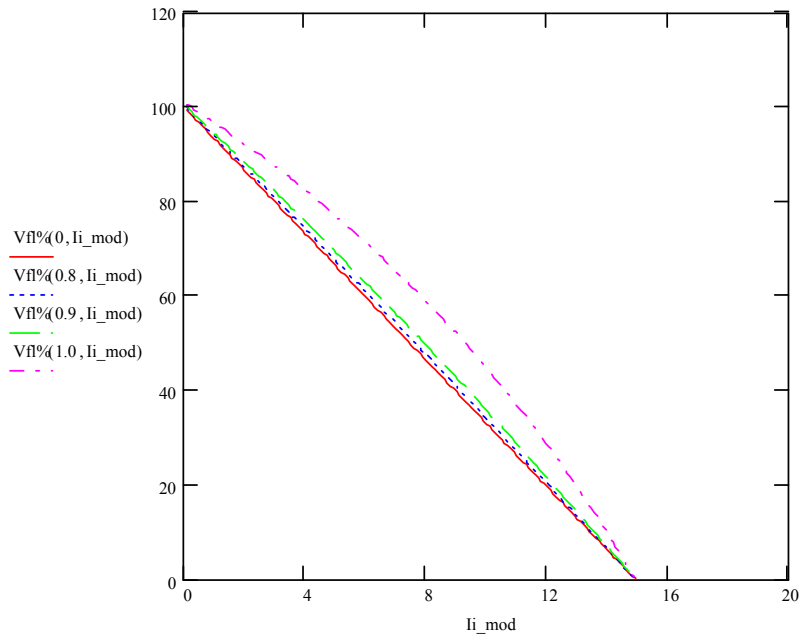
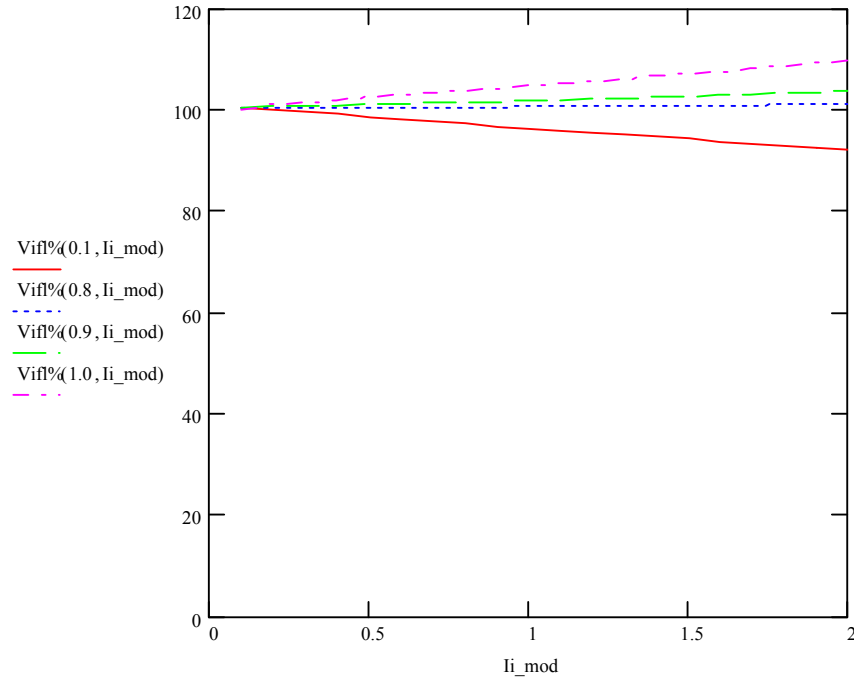


Figure 84: Load characteristics of an MSDG system for lagging power factors

Figures 85 and 86 illustrate the inverter output voltage at different load levels that is necessary to maintain a constant transformer secondary voltage of 1.0 pu. In these figures, the inverter output voltage is represented as a percent of its no-load value, and the load current is in pu. As seen in Figures 85 and 86, the inverter output voltage has to be lesser in magnitude for leading power factor as compared with the lagging power factor loads necessary to maintain a constant terminal voltage. The curves corresponding

to the unity power factor lie between that of the leading and lagging power factors. At low leading power factor, the inverter is required to output a voltage below 1.0 pu. Likewise, at low lagging power factor, the inverter is required to output a higher voltage to achieve this condition. This is due to the inductive nature of the filter and transformer leakage.



**Figure 85: Inverter output voltage
for constant load terminal voltage
(for leading power factors)**

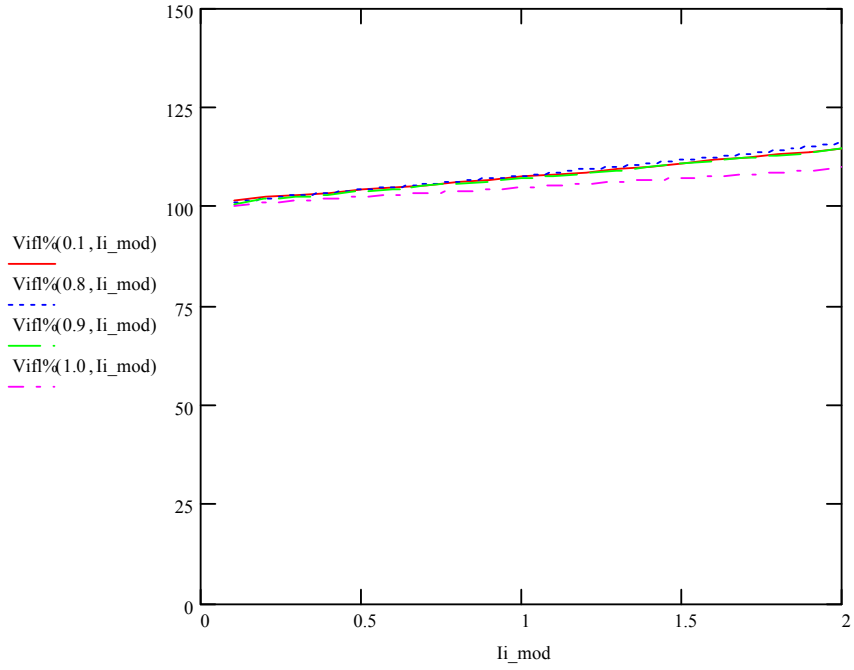


**Figure 86: Inverter output voltage
for constant load terminal voltage
(for lagging power factors)**

Table 7: Filter and transformer impedances in per-unit

Parameter	Value (<i>pu</i>)
Z_f	$0.0137 + j 0.024$
Z_t	$0.038 + j 0.037$

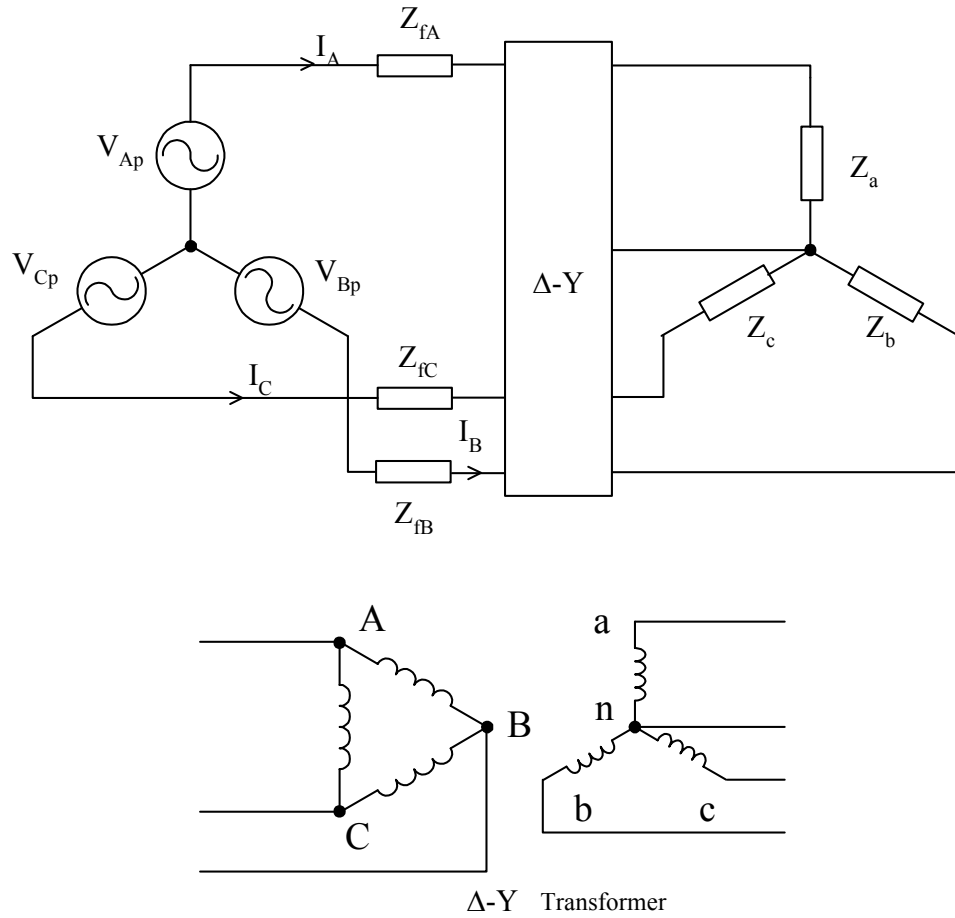


Figure 87: Simplified schematic of the circuit to test the regulation of Δ -Y transformer secondary voltage

At first, theoretical analysis at the fundamental frequency is conducted in Mathcad™ software, and subsequently, simulation of a space vector PWM inverter-based system is made using the MATLAB Simulink™ software package. Their results are presented below for different classes of balanced three-phase/four-wire loads. In the plots presented, the straight lines denote results from theoretical analysis at fundamental frequency, and the points marked 'x' denote simulation results.

Figure 88 gives the regulation of transformer secondary voltage (in pu) for variation in a balanced resistive load. In this figure, the resistive load is varied from zero to 15 kW, and the regulation of the transformer secondary voltage is observed. The simulation results are obtained from digital simulation of the MSDG system and are collected as data points. The fundamental component of simulation results is computed by utilizing MATLAB™ tools on Fast Fourier Transform (FFT). As seen in Figure 88, the regulation

of transformer secondary voltage for a balanced resistive load is 2.6% and is equal for all three phases. It is to be noted that the 'Po' axis contains power expressed in pu with base power as 15 kW. The results obtained from simulation are in agreement with the theoretical analysis results.

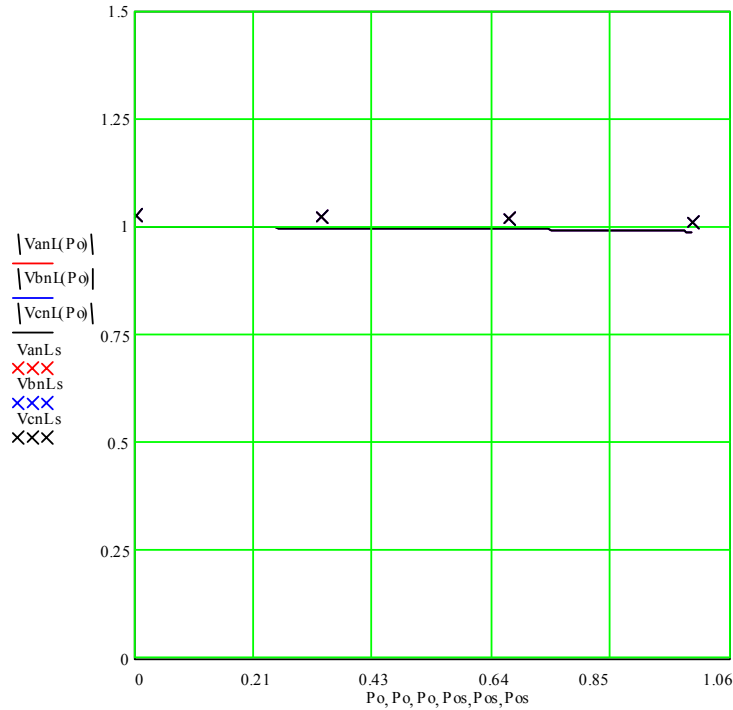


Figure 88: Results of regulation test against variation in balanced resistive load
 $Z_a = Z_b = Z_c = V_{rms}^2 / P_o$, where $V_{rms} = 208$ V and P_o is varied from 0.1 W to 15,000 W.

The regulation of transformer secondary voltage (in pu) for variation in a balanced inductive load is displayed in Figure 89. In this figure, the resistive load is varied from zero to 15 kW, and the load power factor is maintained constant at 0.707 (lagging). As seen in Figure 89, the regulation of transformer secondary voltage for a balanced inductive load of power factor 0.707 (lagging) is 4.2% for all three phases. The regulation for inductive load is more than that for resistive load.

Figure 90 gives the regulation for variation in a balanced capacitive load. In this plot, the resistive load is varied from zero to 15 kW, and the load power factor is maintained constant at 0.707 (leading). As seen in Figure 90, the regulation of transformer secondary voltage for a balanced capacitive load of power factor 0.707 (leading) is -0.6% for all three phases. A negative regulation indicates that the transformer secondary voltage increases for increasing load power.

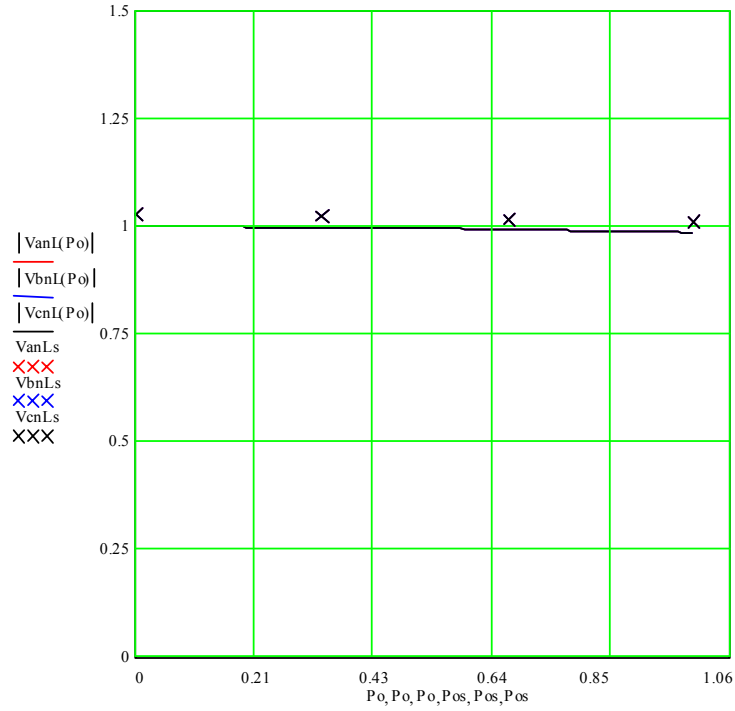


Figure 89: Results of regulation test against variation in balanced inductive load

$$Z_a = Z_b = Z_c = \frac{V_{rms}^2}{\sqrt{2}P_o} (1 + j), \text{ where } V_{rms} = 208 \text{ V and } P_o \text{ is varied from } 0.1 \text{ W to } 15,000 \text{ W.}$$

For all three classes of balanced loads shown in Figures 88-90, the simulation results match closely the results obtained from theoretical analysis. It is observed that the regulation is positive for resistive and inductive loads and is negative for capacitive loads. Among the resistive and inductive loads, regulation is the highest for inductive loads.

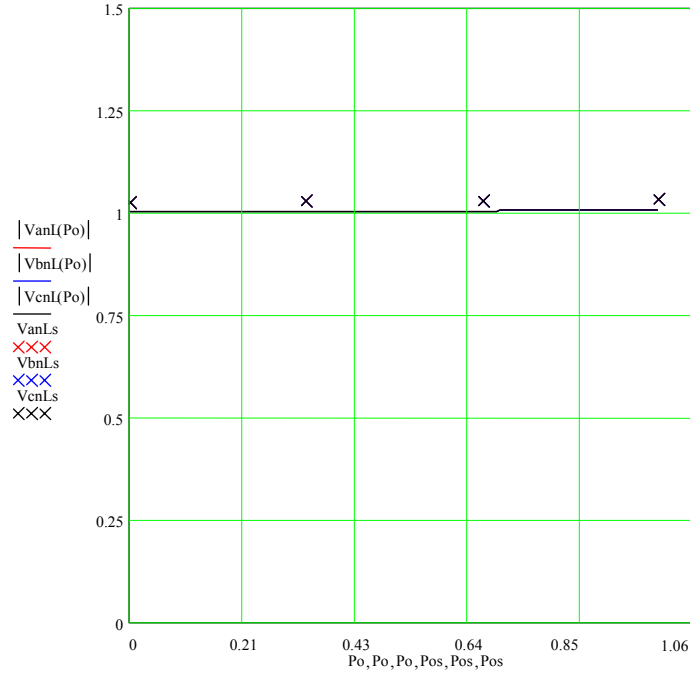


Figure 90: Results of regulation test against variation in balanced capacitive load

$$Z_a = Z_b = Z_c = \frac{1}{\sqrt{2}} \frac{V_{rms}^2}{P_o} (1 - j), \text{ where } V_{rms} = 208 \text{ V and } P_o \text{ is varied from 0.1 W to 15 kW}$$

7.1.2 Unbalanced Three-Phase Analysis

The analysis presented in the previous section is applicable only for balanced three-phase circuits. Nevertheless, solving three-phase equations from circuit theory can make analysis on any generalized three-phase circuit including unbalanced circuits. Modern computational tools such as MATHCAD™ software lighten the labor and give full play in performing the calculations. The theoretical analysis is made after the three-phase/four-wire load, connected on the secondary side of the Δ -Y transformer, is transformed to the primary side. The currents flowing through the branches on the delta side of the transformer are determined. Then, the currents in the wye side of the transformer will be ‘turns ratio’ times that in the corresponding winding on the delta-side. The terminal voltage is the voltage drop across the load because of these wye-side currents.

Figure 91 gives the regulation of transformer secondary voltage (in pu) to variation in unbalanced resistive load for all three phases. In this part of the analysis, the resistive load in phase ‘a’ is varied from zero to 15 kW. In phase ‘b,’ the resistive load is twice that in phase ‘a,’ and in phase ‘c,’ it is 10 times that in phase ‘a.’ The straight lines denote results from theoretical analysis at fundamental frequency, and the points marked ‘x’ indicate simulation results. As seen in Figure 91, the regulation of transformer secondary

voltage for an unbalanced resistive load is different for the three phases. Regulation is observed to be 2% for phase ‘a,’ 1.9% for phase ‘b’ and 0.2% for phase ‘c.’

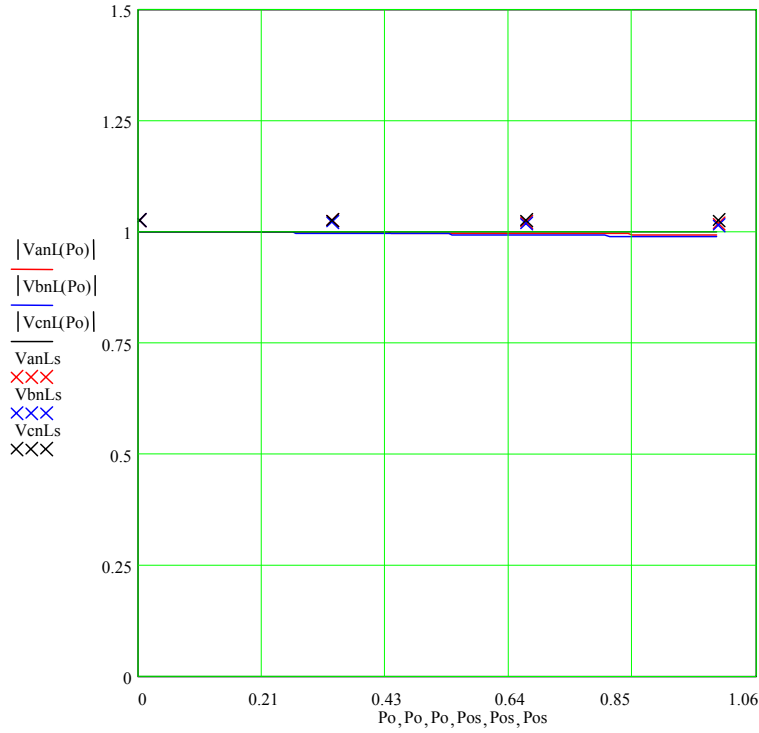


Figure 91: Results of regulation test against variation in unbalanced resistive load

$$Z_a = V_{rms}^2 / P_o, Z_b = 2V_{rms}^2 / P_o, \text{ and } Z_c = 10V_{rms}^2 / P_o,$$

where $V_{rms} = 208 \text{ V}$ and P_o is varied from 0.1 W to 15 kW.

The regulation of transformer secondary voltage (in pu) for the three phases to variation in unbalanced inductive (series R-L) load is shown in Figure 92. The resistive load in phase ‘a’ is varied from zero to 15 kW. In phase ‘b,’ the resistive load is twice that in phase ‘a,’ and in phase ‘c,’ it is 10 times that in phase ‘a.’ In all the three phases, the load power factor is maintained constant at 0.707 (lagging). As seen in Figure 92, the regulation of transformer secondary voltage for an unbalanced inductive load of power factor 0.707 (lagging) is different for the three phases. It is observed to be 3.6% for phase ‘a,’ 2.4% for phase ‘b’ and 0.9% for phase ‘c.’

Figure 93 gives the regulation of transformer secondary voltage (in pu) for the three phases to variation in unbalanced capacitive (parallel R-C) load. The resistive load is varied in phase ‘c’ from zero to 15 kW. In phase ‘b,’ the resistive load is twice that in phase ‘a,’ and in phase ‘c,’ it is 10 times that in phase ‘a.’ In all the three phases, the load power factor is maintained constant at 0.707 (leading). As seen in Figure 93, the regulation of transformer secondary voltage is observed to be -0.8% for phase ‘a,’ 0.4% for phase ‘b’ and -0.6% for phase ‘c.’

The summary of results on regulation of the transformer secondary voltage as a function of the resistive load (with a constant power factor) is tabulated in Table 8. It is observed that regulation is positive for resistive and inductive loads, and it is negative for capacitive loads. Among the resistive and inductive loads, regulation is the highest for inductive loads. Although the regulation is identical for all three phases under balanced load conditions, it is unequal under load imbalance. In particular, it is observed that for an unbalanced capacitive load of power factor 0.707 (leading), regulation is positive (i.e., inductive nature) in one phase and negative in other phases. It is close to the power factor of 0.82 (leading) that was earlier predicted to have a zero regulation at full load. Nevertheless, this is one particular case of unbalanced loads, and in general, unbalanced three-phase/four-wire loads can have loads of different power factors in the three phases. It is to be noted that all cases provided in Table 3 have loads of equal power factor in all three phases.

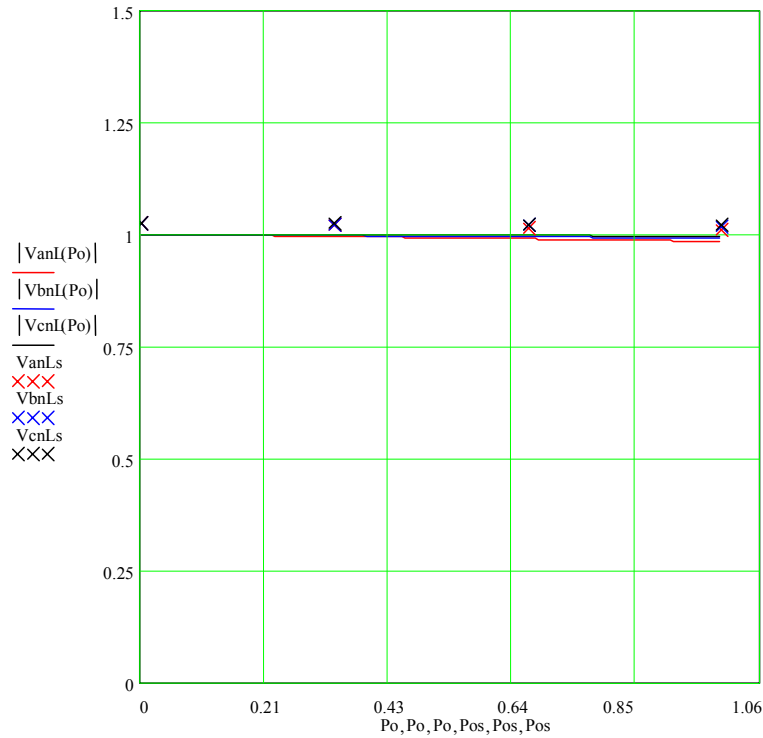


Figure 92: Results of regulation test against variation in unbalanced inductive load

$$Z_a = \frac{V_{rms}^2}{\sqrt{2}P_o} (1 + j), Z_b = \frac{2V_{rms}^2}{\sqrt{2}P_o} (1 + j), \text{ and } Z_c = \frac{10V_{rms}^2}{\sqrt{2}P_o} (1 + j), \text{ where } V_{rms} = 208 \text{ V and } P_o \text{ is varied from 0.1 W to 15 kW.}$$

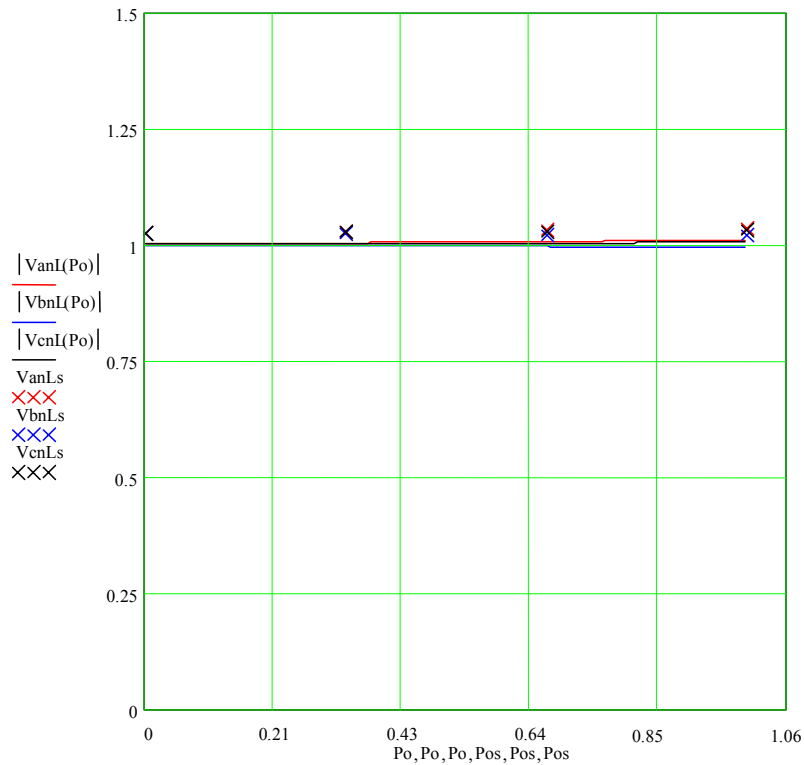


Figure 93: Results of regulation test against variation in unbalanced capacitive load

$Z_a = \frac{V_{rms}^2}{\sqrt{2}P_o} (1 - j)$, $Z_b = \frac{2V_{rms}^2}{\sqrt{2}P_o} (1 - j)$, $Z_c = \frac{10V_{rms}^2}{\sqrt{2}P_o} (1 - j)$, where $V_{rms} = 208$ V and P_o is varied from 0.1 W to 15,000 W.

Table 8: Summary of results on load regulation

Load		% Regulation		
Type	p.f.	Phase 'a'	Phase 'b'	Phase 'c'
Balanced resistive load	1.0	2.6	2.6	2.6
Balanced inductive load	0.7 (lag)	4.2	4.2	4.2
Balanced capacitive load	0.7 (lead)	-0.6	-0.6	-0.6
Unbalanced resistive load	1.0	2.0	1.9	0.2
Unbalanced inductive load	0.7 (lag)	3.6	2.4	0.9
Unbalanced capacitive load	0.7 (lead)	-0.8	0.4	-0.6

7.2 Simulation Modeling of the Island Mode MSDG System

In this section, the waveforms obtained from digital simulation of an island mode MSDG system for different classes of loads, viz., three-phase balanced and unbalanced resistive, inductive and capacitive load,s are presented. Digital simulation of the MSDG system was carried out in MATLAB Simulink™ software. Elaborate results in the form of time-domain waveforms and performance characteristics are illustrated.

The circuit schematic of the MSDG system is given in Figure 63 (Ref. Chapter 6). For simulating the system shown in Figure 63 using MATLAB Simulink™, an equivalent circuit shown in Figure 94 (reproduced from Figure 68 in Chapter 6) is used. In this circuit, the Δ -Y transformer is approximated as a voltage source in series with the leakage reactance on the primary side and a current source on the secondary side. As seen in the figure, the dc-bus voltage of the inverter is assumed constant. This is acceptable if the MSDG system contains energy storage devices such as batteries. The inverter switching is based on space vector pulse-width modulation (SVPWM) at a switching frequency of 4 kHz. The MSDG system is divided into several modules, called subsystems, that denote its major components. These subsystems are space-vector pulse-width modulator, inverter, LC filter, transformer and load. In each subsystem, linear differential equations governing the various circuit components are composed. Each subsystem may be further subdivided into individual phases. Because the inverter here is a three-legged inverter, the circuit on the primary side of the Δ -Y transformer is a three-phase/three-wire circuit. A pole-throw model simulates the inverter and the LC filter for each phase [18]. The potential of neutral with respect to the negative dc rail is utilized to obtain the phase-neutral voltages of the filter capacitors on three phases. The circuit parameters of the system used for simulation are the same as those given in Table 6.

The simulation waveforms for a three-phase balanced resistive load are displayed in Figures 95 through 102. The load consists of a resistance R_x , where subscript 'x' represents any one of three phases.

$$R_x = \frac{V_{rms}^2}{P_o} \quad (51)$$

where $V_{rms} = 208$ V and $P_o = 15000$ W.

The transformer secondary voltage waveforms with respect to the neutral are shown in Figure 95. Subscript 'x' in the label of the figure represents any one of the three phases. The Fast Fourier Transform (FFT) is computed in MATLAB™ and plotted in Figure 96. Figure 97 gives the phasor diagrams of these three phase-neutral voltages. It is observed that the terminal voltages are balanced and the regulation is equal to about 2% in all three phases. Figure 98 gives the filter inductor current waveform. These currents show distortion owing to resonance of the filter inductor with the capacitor. The three-phase load currents drawn by the resistive load are displayed in Figure 99, and their FFT is plotted in Figure 100. The phasor diagram of these load currents is illustrated in Figure

101. As seen in Figure 101, the currents drawn by the balanced resistive load are equal in magnitude in all three phases and equally displaced. Figure 102 gives the instantaneous three phase powers and the total power drawn by the resistive load. The instantaneous powers of the three phases are of double the fundamental frequency i.e., 120 Hz. The sum of the three instantaneous powers is called the three-phase instantaneous power drawn by the resistive load. It is the equal to the sum of the instantaneous real and reactive power drawn in three phases. As seen in Figure 102, the three-phase instantaneous power drawn by the balanced load is more or less constant. This constant average value gives the three-phase real power drawn by the load. It also implies that the sum of the reactive powers drawn by three phases is zero, i.e., the reactive powers in three phases cancel each other.

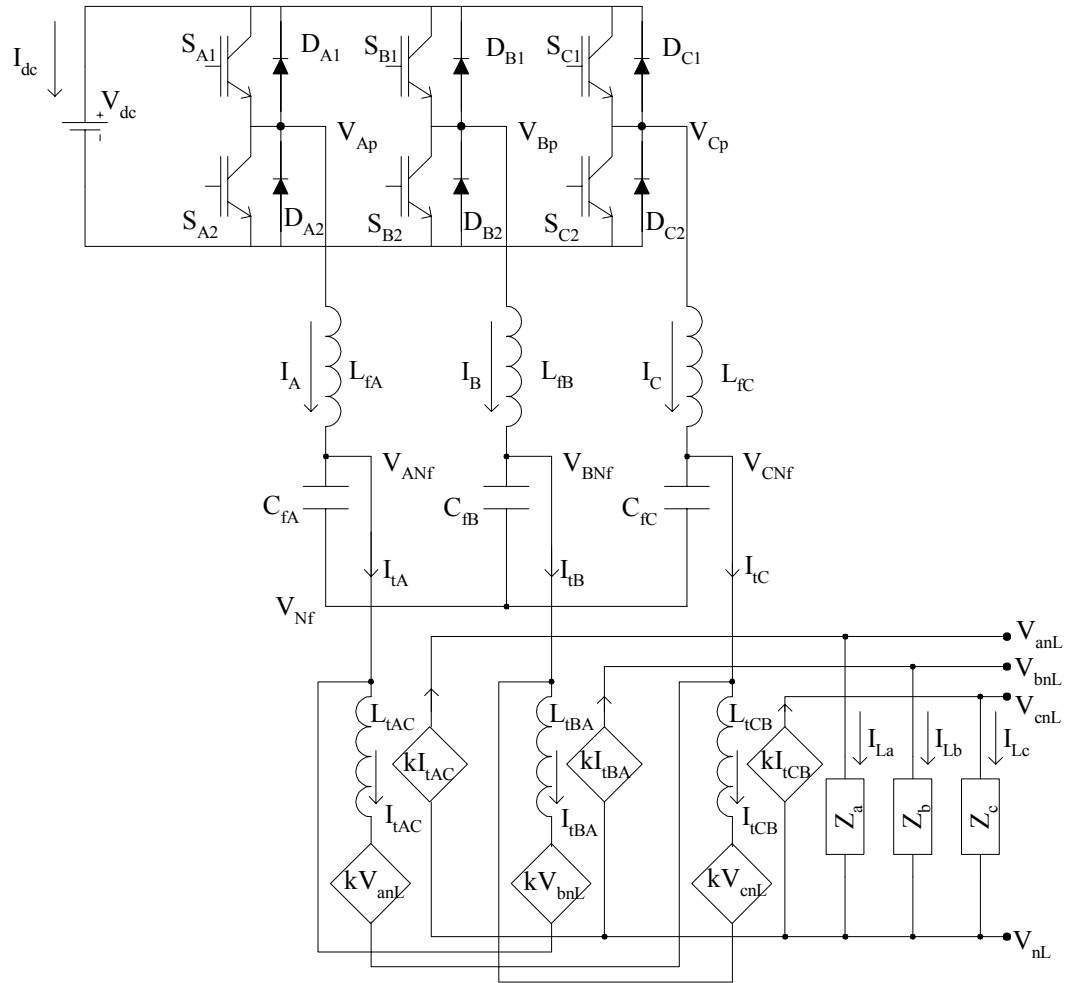


Figure 94: Schematic of the regulation test circuit containing the equivalent circuit representation of the Δ -Y transformer

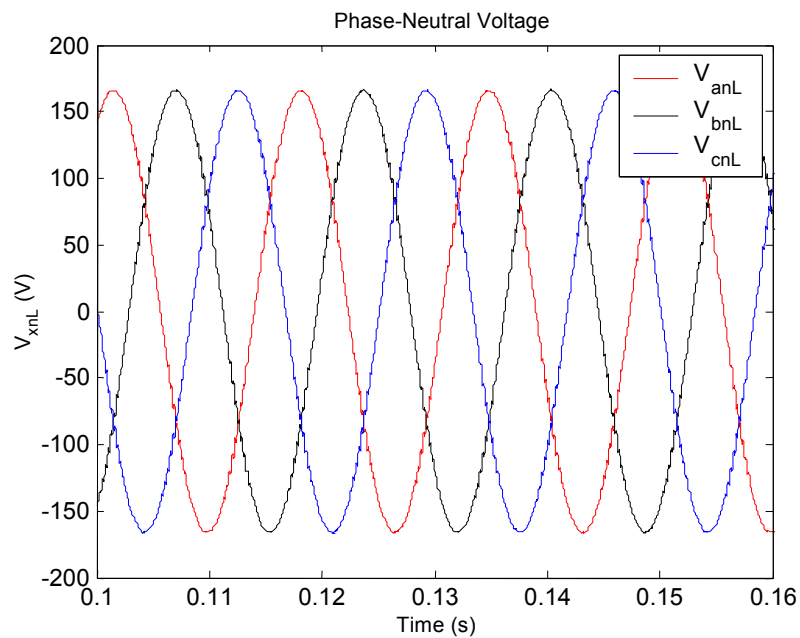


Figure 95: Transformer secondary terminal voltage waveform for a balanced resistive load

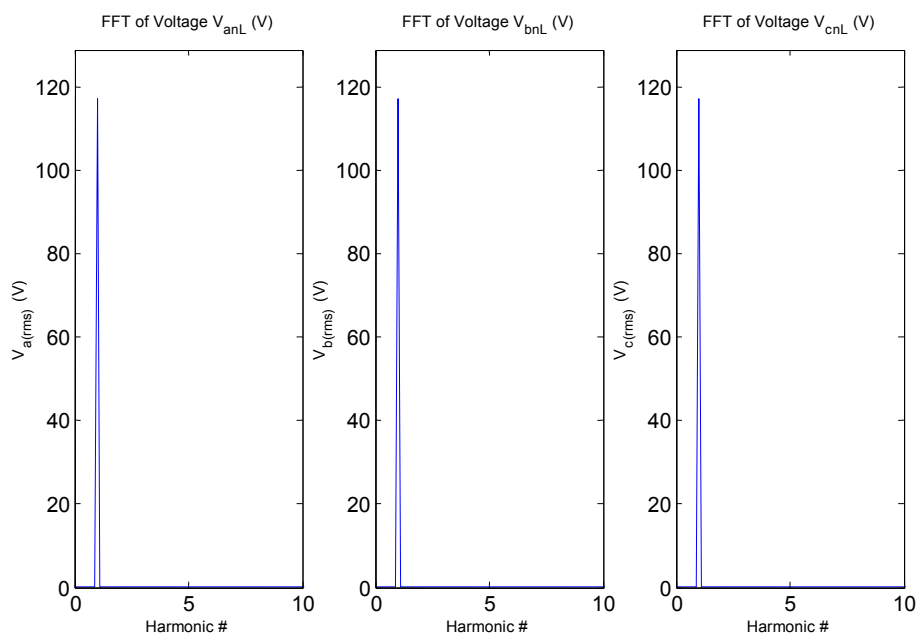


Figure 96: FFT of the transformer secondary terminal voltage in three phases for a balanced resistive load

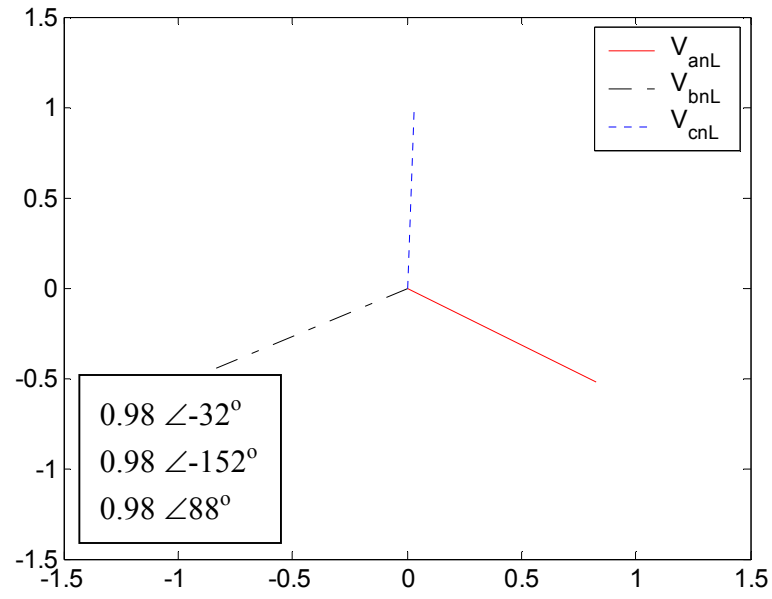


Figure 97: Phasor diagram of the three-phase voltages for a balanced resistive load

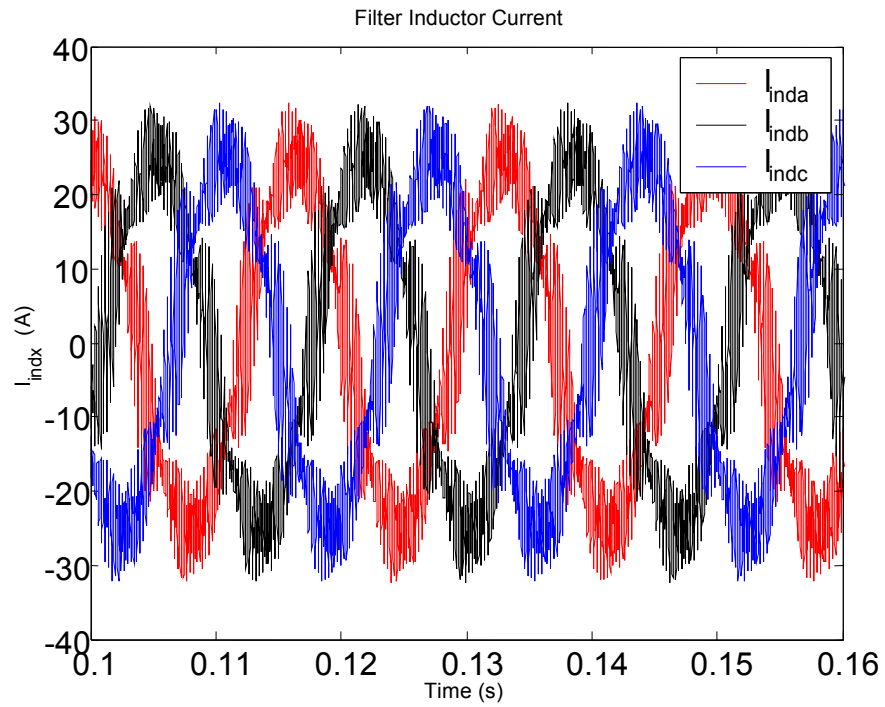


Figure 98: Three-phase filter inductor current waveform for a balanced resistive load

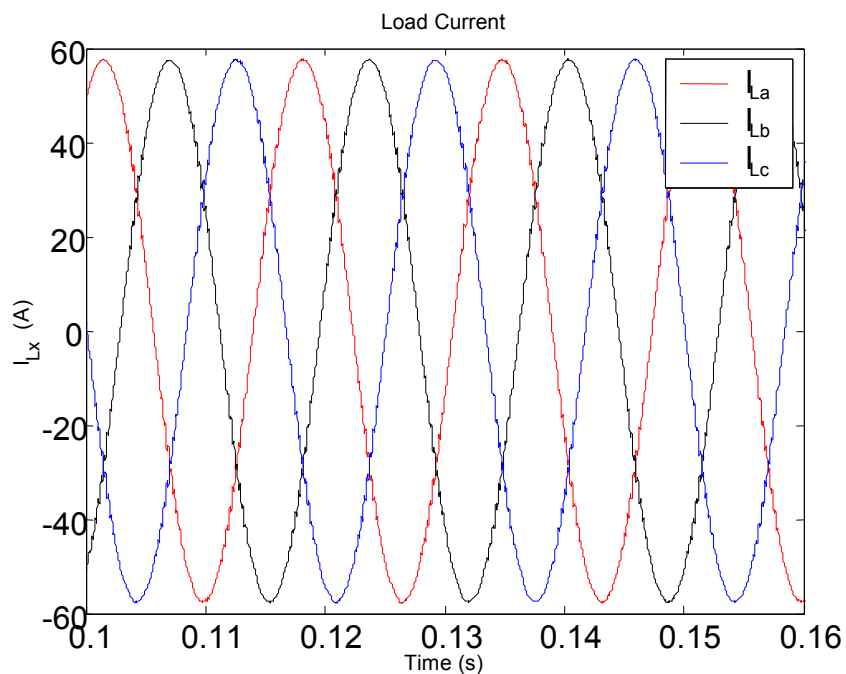


Figure 99: Three-phase load current waveform for a balanced resistive load

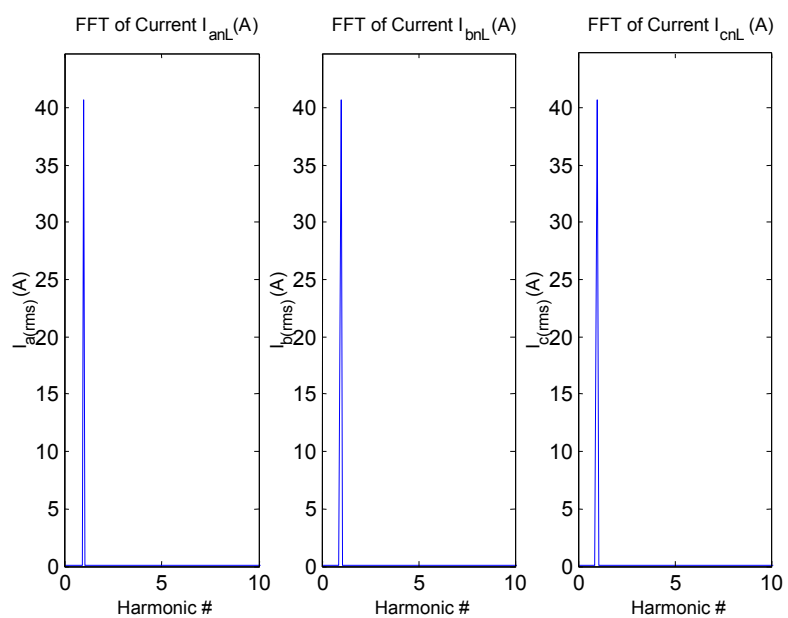


Figure 100: FFT of the load current in three phases for a balanced resistive load

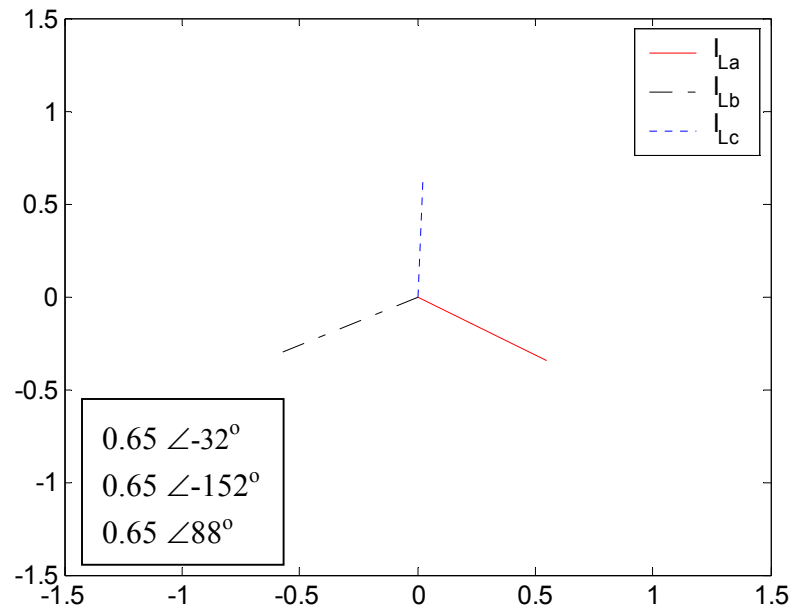


Figure 101: Phasor diagram of the three-phase currents for a balanced resistive load

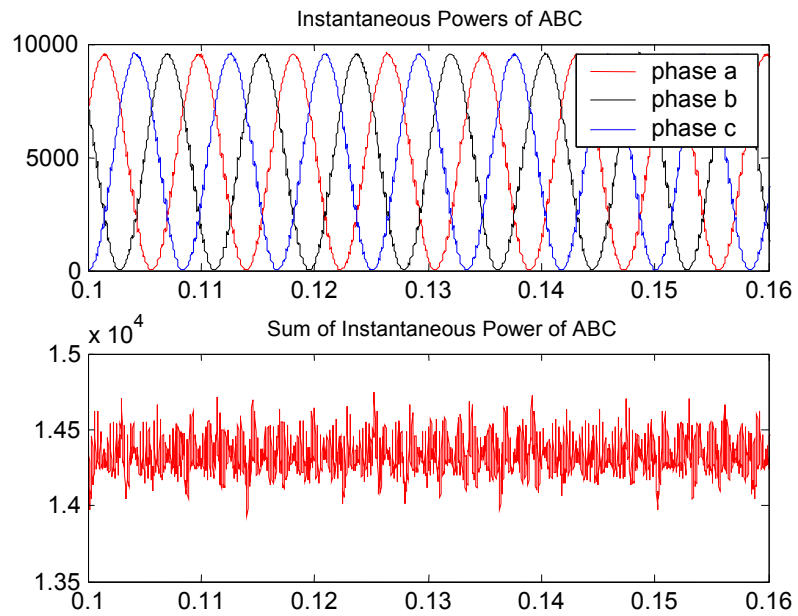


Figure 102: Instantaneous powers in three phases (top) and total power (bottom) for a balanced resistive load

The simulation waveforms for a three-phase balanced inductive load are displayed in Figures 103 through 110. The load consists of a series RL circuit of resistance R_x and inductive reactance X_x , where subscript 'x' represents any one of three phases.

$$R_x = \frac{V_{\text{rms}}^2}{P_o} \quad (52)$$

$$X_x = \frac{V_{\text{rms}}^2}{P_o} \quad (53)$$

where $V_{\text{rms}} = 208 \text{ V}$ and $P_o = 15 \text{ kW}$.

The transformer secondary voltage waveforms with respect to the neutral are shown in Figure 103. Subscript 'x' in the label of the figure represents any one of the three phases. The FFT is computed in MATLAB™ and plotted in Figure 104. Figure 105 gives the phasor diagrams of these three phase-neutral voltages. It is observed that the terminal voltages are balanced and the regulation is equal to about 3% in all three phases. Figure 106 gives the filter inductor current waveform. These currents show distortion owing to resonance of the filter inductor with the capacitor. The three-phase load currents drawn by the series RL load are displayed in Figure 107, and their FFT is plotted in Figure 108. The phasor diagram of these load currents is illustrated in Figure 109. As seen in Figure 109, the currents drawn by the balanced inductive load are equal in magnitude in all three phases and also equally displaced. Figure 110 gives the instantaneous three-phase powers and the total power drawn by the inductive load. The instantaneous powers of the three phases are of double the fundamental frequency i.e., 120 Hz. The sum of the three instantaneous powers is called the three-phase instantaneous power drawn by the inductive load. It is the equal to the sum of the instantaneous real and reactive power drawn in three phases. As seen in Figure 110, the three-phase instantaneous power drawn by the balanced load is more or less constant. This constant average value gives the three-phase real power drawn by the load. It also implies that the sum of the reactive powers drawn by three phases is zero, i.e., the reactive powers in three phases cancel each other.

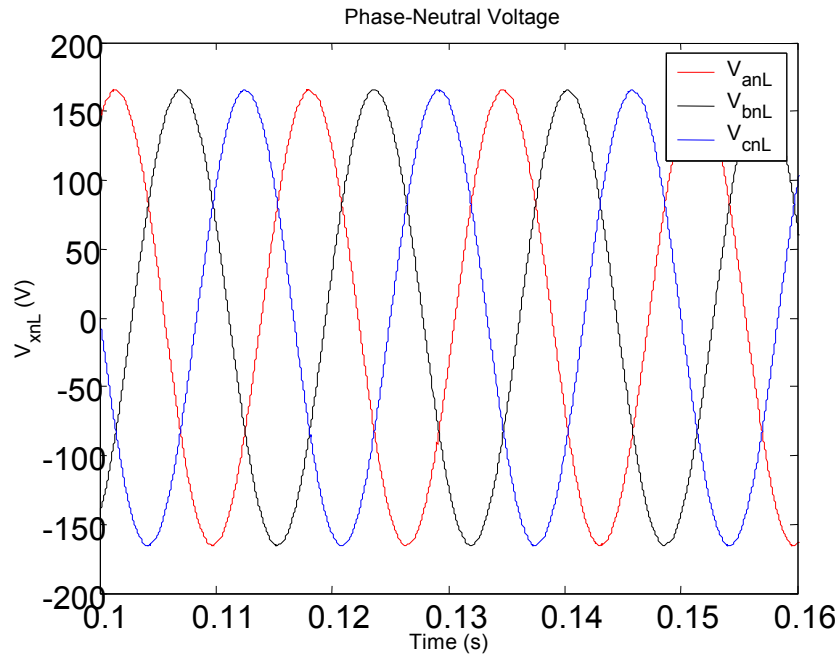


Figure 103: Transformer secondary terminal voltage waveform for a balanced inductive load

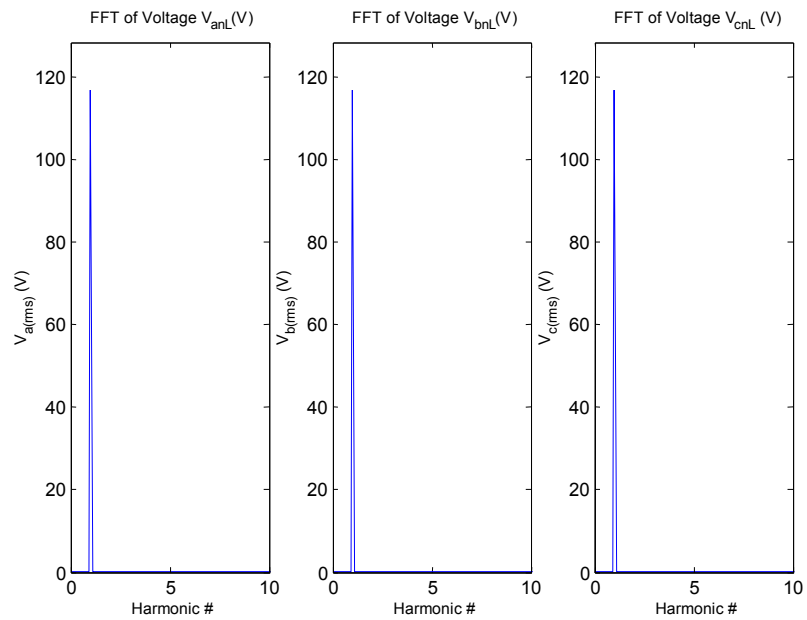


Figure 104: FFT of the transformer secondary terminal voltage in three phases for a balanced inductive load

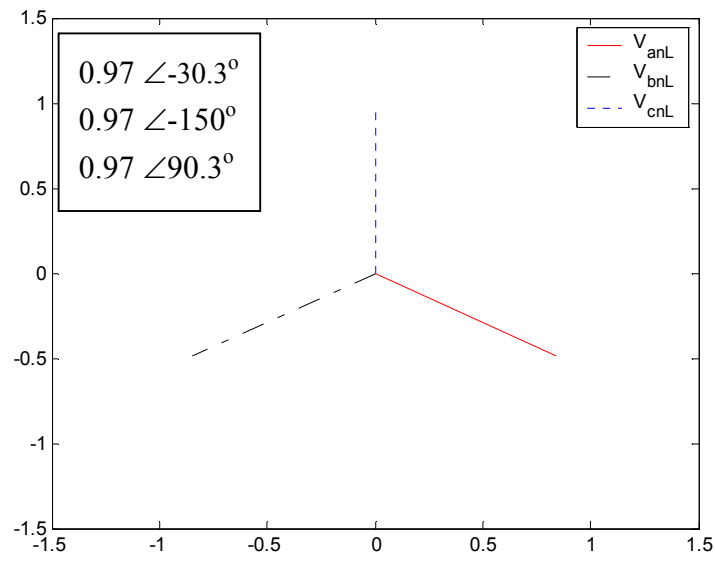


Figure 105: Phasor diagram of the three-phase voltages for a balanced inductive load

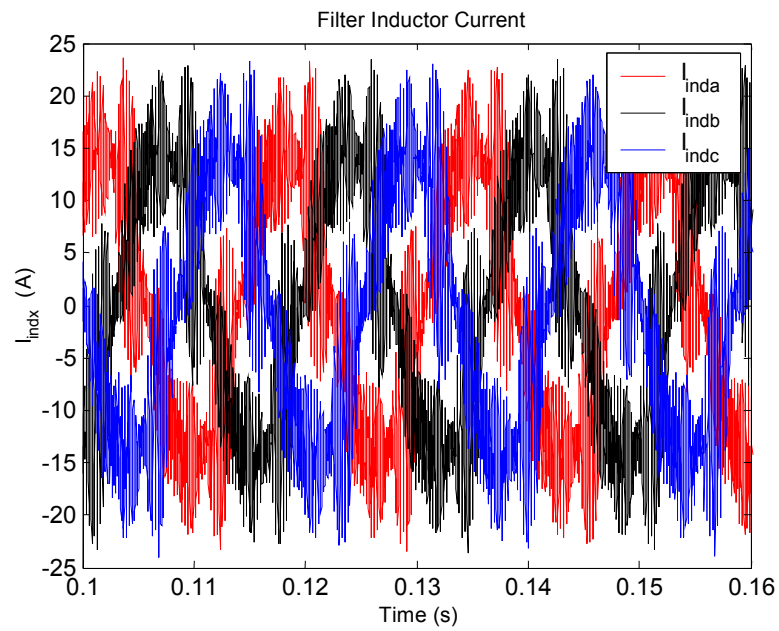


Figure 106: Three-phase filter inductor current waveform for a balanced inductive load

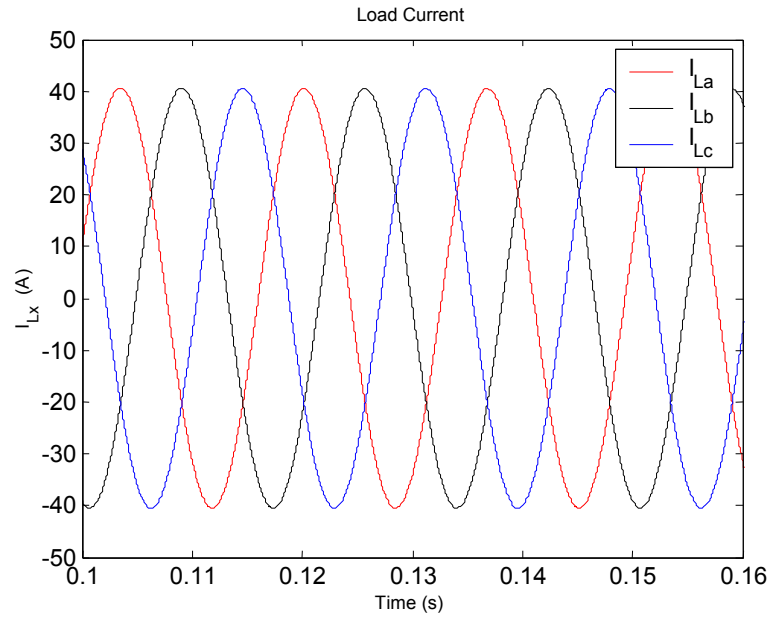


Figure 107: Three-phase load current waveform for a balanced inductive load

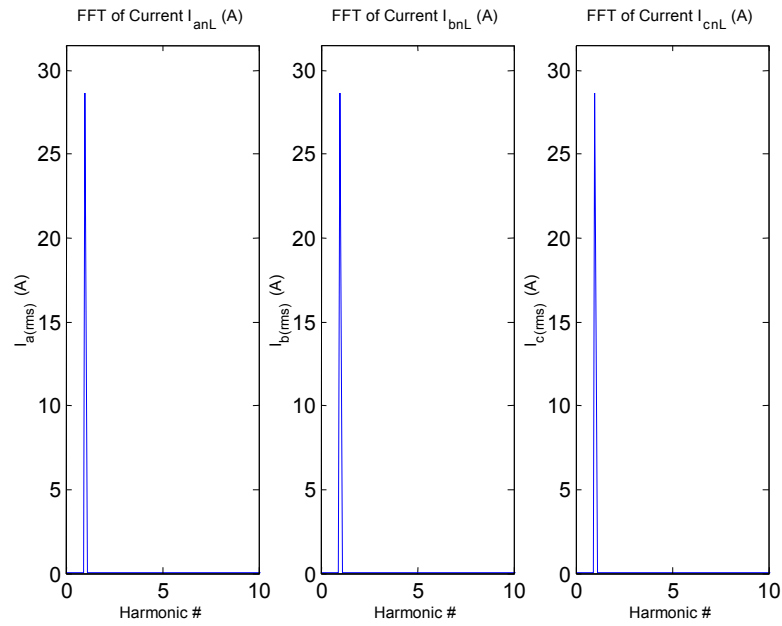


Figure 108: FFT of the load current in three phases for a balanced inductive load

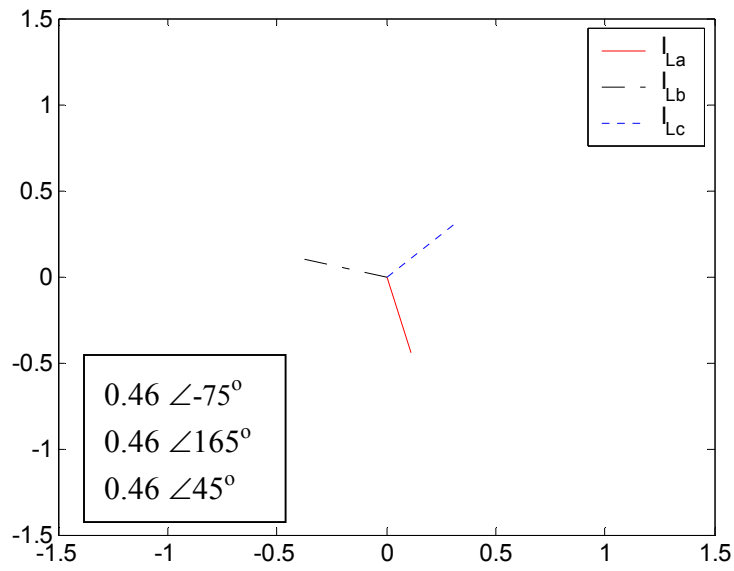


Figure 109: Phasor diagram of the three-phase currents for a balanced inductive load

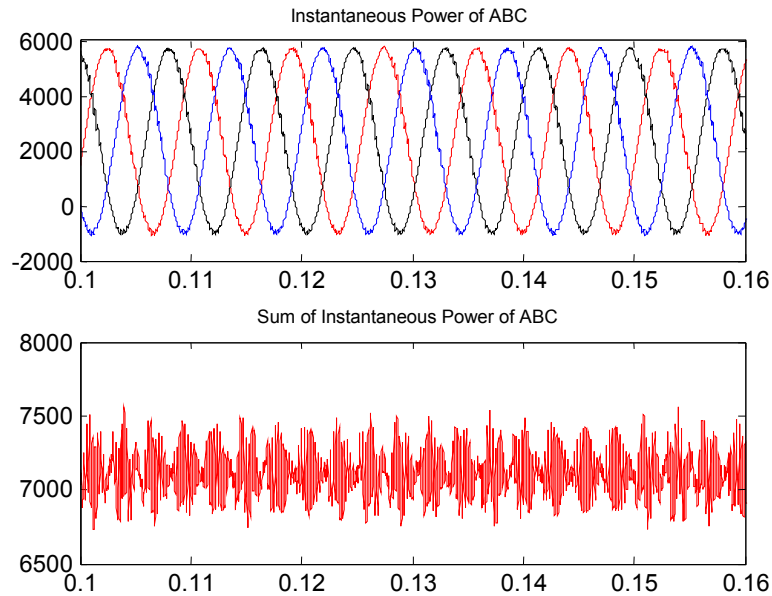


Figure 110: Instantaneous powers in three phases (top) and total power (bottom) for a balanced inductive load

The simulation waveforms for a three-phase balanced capacitive load are displayed in Figures 111 through 118. The load consists of a series RL circuit of resistance R_x and capacitive reactance X_x , where subscript 'x' represents any one of three phases.

$$R_x = \frac{V_{\text{rms}}^2}{P_o} \quad (54)$$

$$X_x = \frac{V_{\text{rms}}^2}{P_o} \quad (55)$$

where $V_{\text{rms}} = 208 \text{ V}$ and $P_o = 15 \text{ kW}$.

The transformer secondary voltage waveforms with respect to the neutral are shown in Figure 111. Subscript 'x' in the label of the figure represents any one of the three phases. The FFT is computed in MATLAB™ and plotted in Figure 112. Figure 113 gives the phasor diagrams of these three phase-neutral voltages. It is observed that the terminal voltages are balanced and the regulation is equal to about -1% in all three phases. Figure 114 gives the filter inductor current waveform. These currents show distortion owing to resonance of the filter inductor with the capacitor. The three-phase load currents drawn by the parallel RC load are displayed in Figure 115, and their FFT is plotted in Figure 116. The phasor diagram of these load currents is illustrated in Figure 117. As seen in Figure 117, the currents drawn by the balanced capacitive load are equal in magnitude in all three phases and equally displaced. Figure 118 gives the instantaneous three-phase powers and the total power drawn by the capacitive load. The instantaneous powers of the three phases are of double the fundamental frequency, i.e., 120 Hz. The sum of the three instantaneous powers is called the three-phase instantaneous power drawn by the capacitive load. It is equal to the sum of the instantaneous real and reactive power drawn in three phases. As seen in Figure 118, the three-phase instantaneous power drawn by the balanced load is more or less constant. This constant average value gives the three-phase real power drawn by the load. It also implies that the sum of the reactive powers drawn by three phases is zero, i.e., the reactive powers in three phases cancel each other.

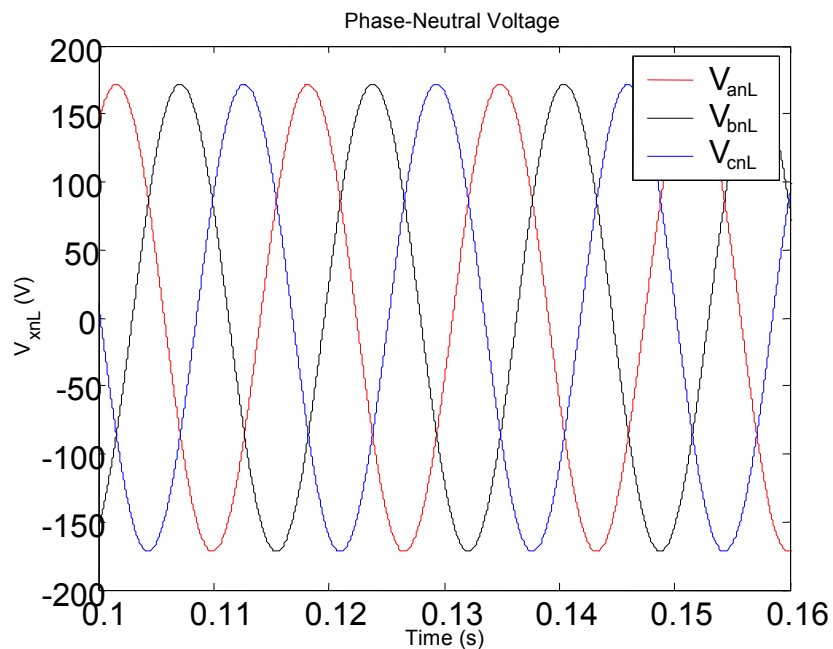


Figure 111: Transformer secondary terminal voltage waveform for a balanced capacitive load

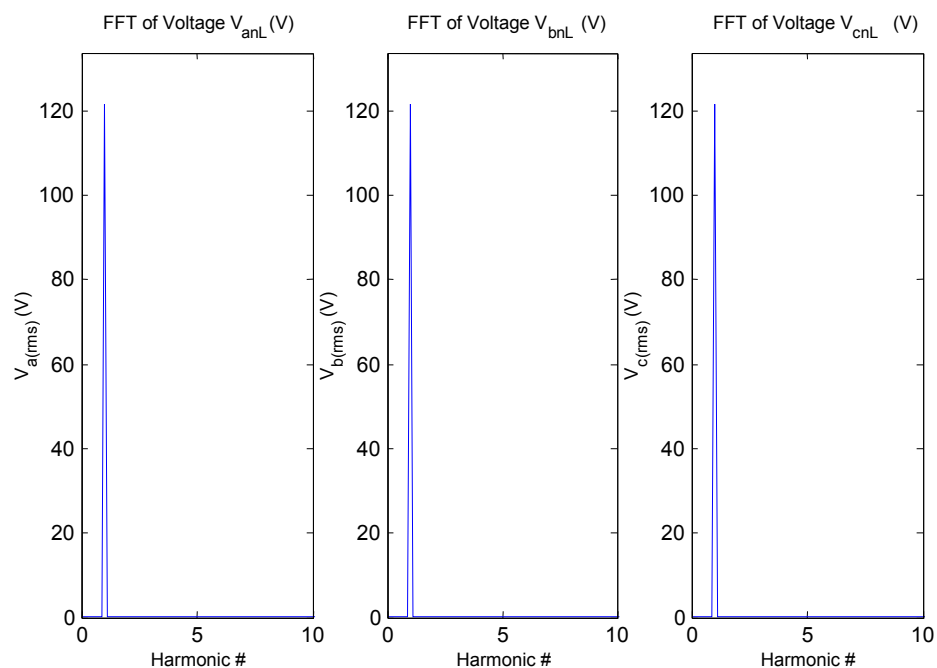


Figure 112: FFT of the transformer secondary terminal voltage in three phases for a balanced capacitive load

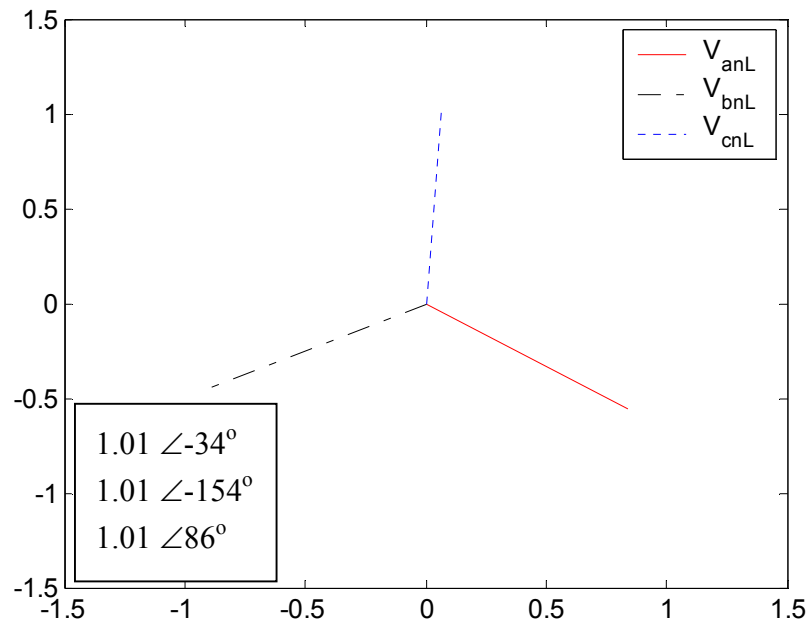


Figure 113: Phasor diagram of the three-phase voltages for a balanced capacitive load

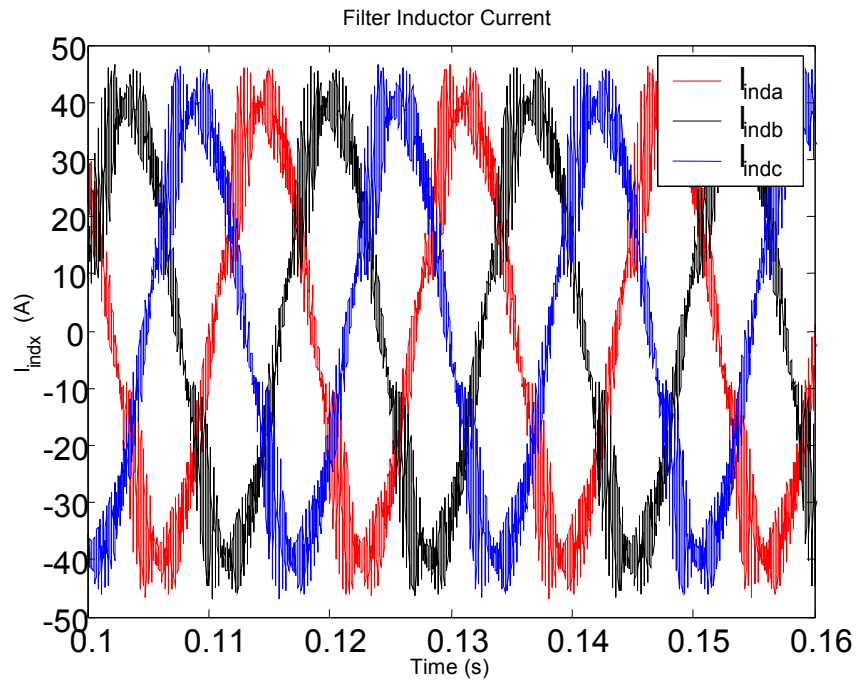


Figure 114: Three-phase filter inductor current waveform for a balanced capacitive load

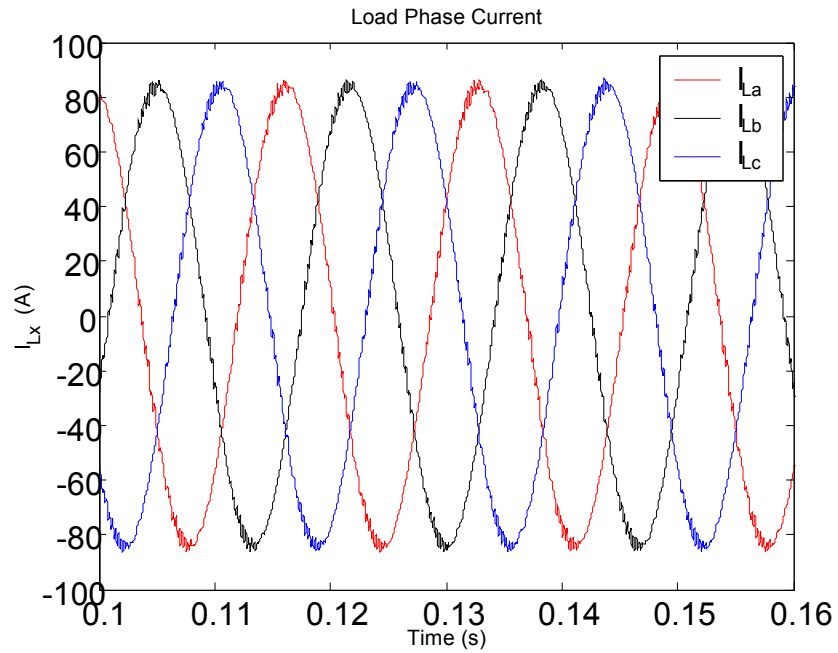


Figure 115: Three-phase load current waveform for a balanced capacitive load

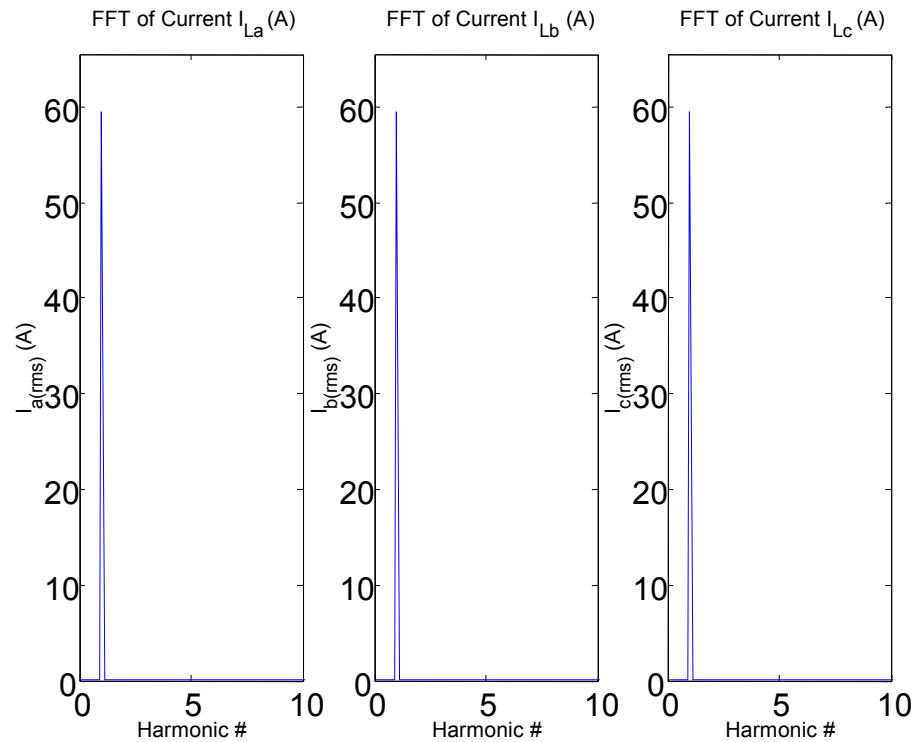


Figure 116: FFT of the load current in three phases for a balanced capacitive load

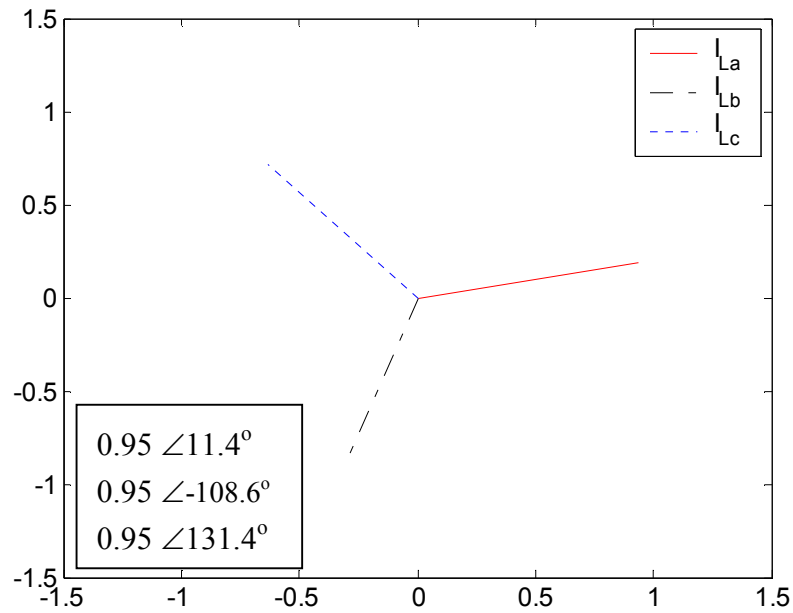


Figure 117: Phasor diagram of the three-phase currents for a balanced capacitive load

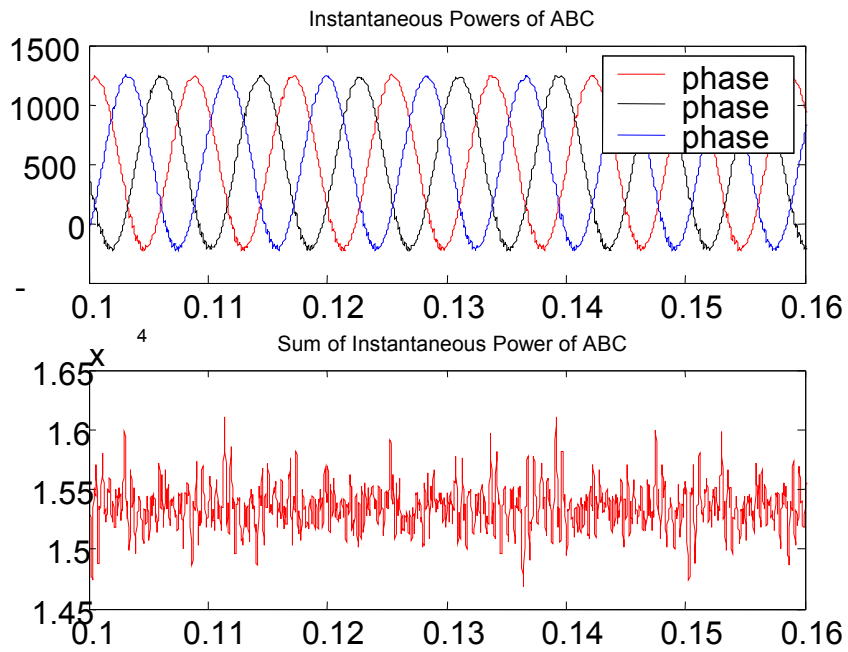


Figure 118: Instantaneous powers in three phases (top) and total power (bottom) for a balanced capacitive load

An unbalanced three-phase/four-wire load is also simulated to examine the performance of the MSDG system. The simulation waveforms for a three-phase unbalanced resistive load are displayed in Figures 119 through 126. In this case, the load resistance R_x is given by:

$$R_a = \frac{V_{rms}^2}{P_o} \quad (56)$$

$$R_b = 0.5 R_a$$

$$R_c = 0.8047 R_a$$

where $V_{rms} = 208$ V and $P_o = 15,000$ W.

The transformer secondary voltage waveforms with respect to the neutral are shown in Figure 119. Subscript 'x' in the label of the figure represents any one of the three phases. The FFT of the three-phase voltages is plotted in Figure 120. Figure 121 gives the phasor diagrams of these three phase-neutral voltages. From Figures 120 and 121, it is observed that the terminal voltages are unequal and so is the regulation in the three phases. Regulation is computed to be about 2% in phase 'a,' 4% in phase 'b' and nearly 4% in phase 'c.' Figure 122 shows the filter inductor current waveform. These currents are unequal in the three phases and also show distortion owing to resonance of the filter inductor with the capacitor. The three-phase load currents drawn by the resistive load are displayed in Figure 123. The FFTs of these three-phase load currents are plotted in Figure 124. The phasor diagram of these load currents is illustrated in Figure 125. As seen in Figures 124 and 125, the currents drawn by the unbalanced resistive load are unequal in magnitude in the three phases and are almost equally displaced in phase. This is because the three-phase/four-wire loads have equal power factor in spite of having unbalance in magnitude. Notably, the sum of the three-phase load currents is not equal to zero, and this contributes to a neutral current in the load that becomes the circulating current in the transformer primary (delta) winding. Figure 126 gives the instantaneous three-phase powers and the total power drawn by the unbalanced resistive load. The instantaneous powers of the three phases are of double the fundamental frequency, i.e., 120 Hz. The sum of the three instantaneous powers is called the three-phase instantaneous power drawn by the resistive load. It is equal to the sum of the instantaneous real power and the reactive power drawn in three phases. As seen in Figure 126, the three-phase instantaneous power drawn by the unbalanced load is a sinusoidal waveform unlike that of balanced load, which was nearly constant (Ref. Figure 28). The average value of the three-phase instantaneous power gives the three-phase real power drawn by the load.

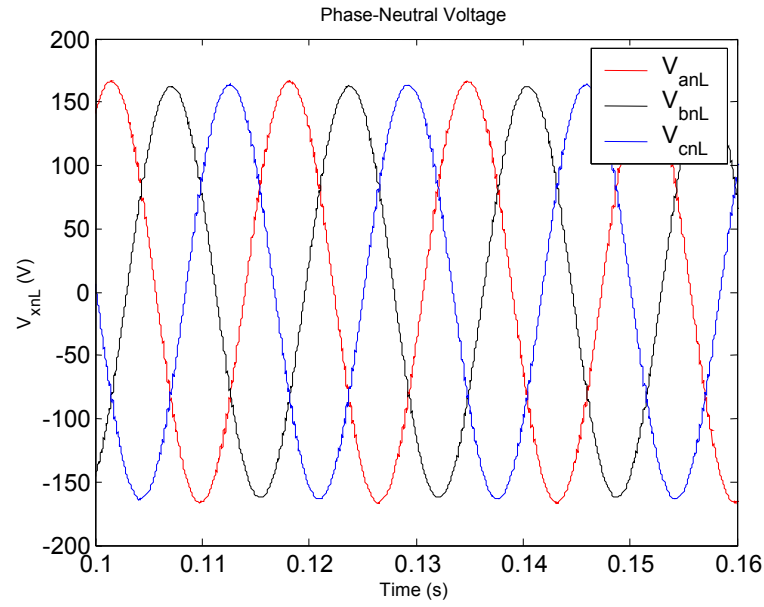


Figure 119: Transformer secondary terminal voltage waveform for an unbalanced resistive load

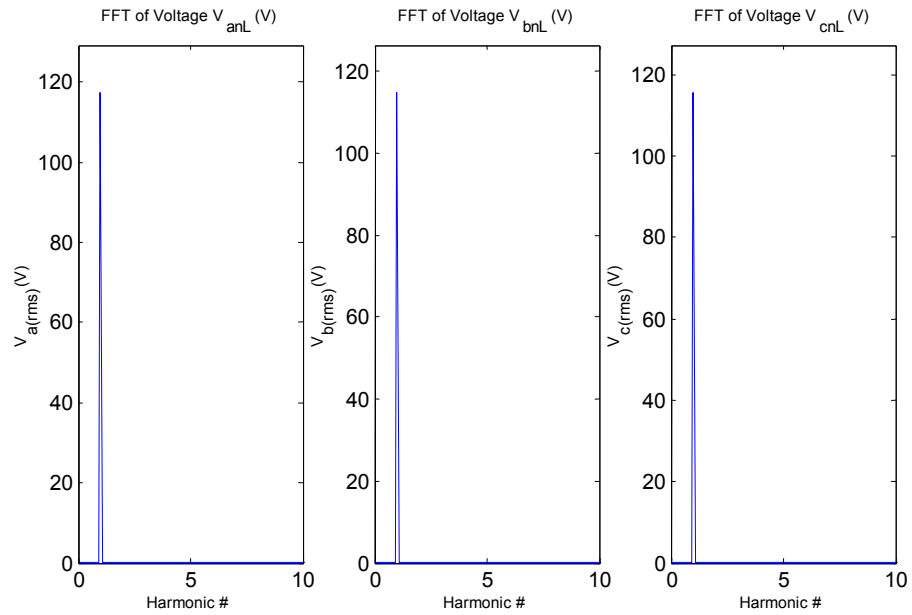


Figure 120: FFT of the transformer secondary terminal voltage in three phases for an unbalanced resistive load

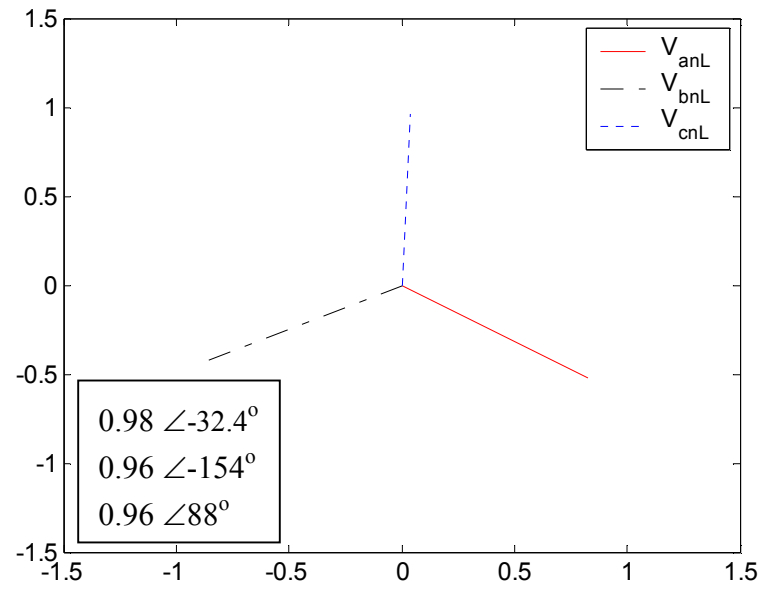


Figure 121: Phasor diagram of the three-phase voltages for an unbalanced resistive load

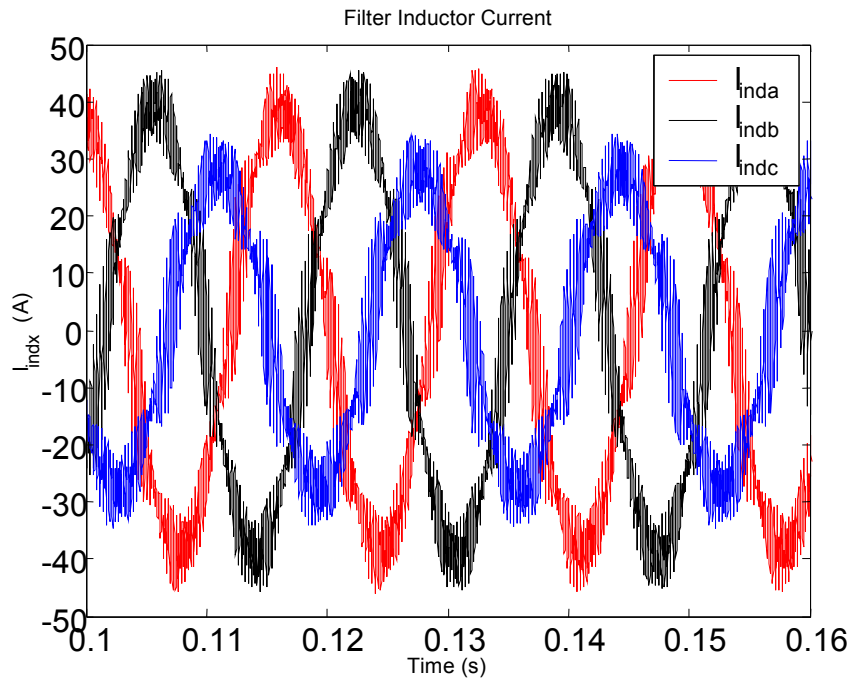


Figure 122: Three-phase filter inductor current waveform for an unbalanced resistive load

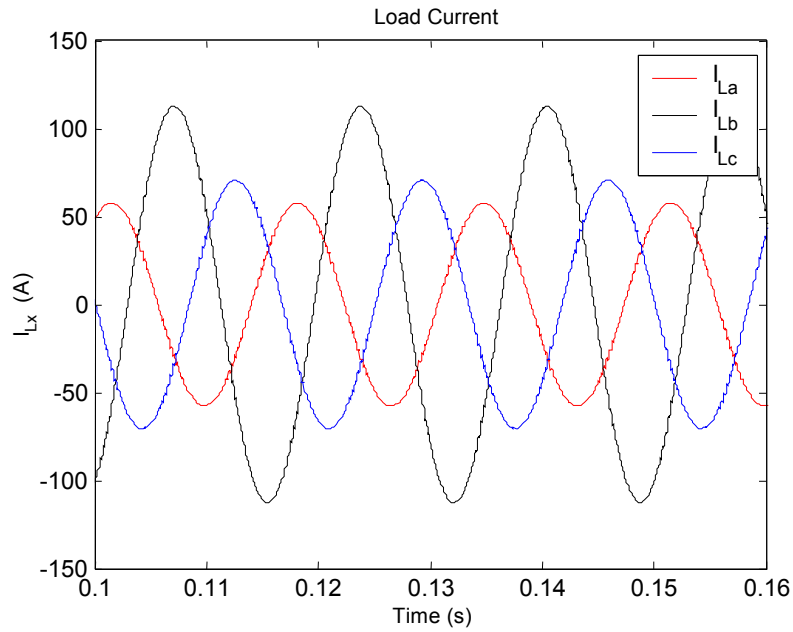


Figure 123: Three-phase load current waveform for an unbalanced resistive load

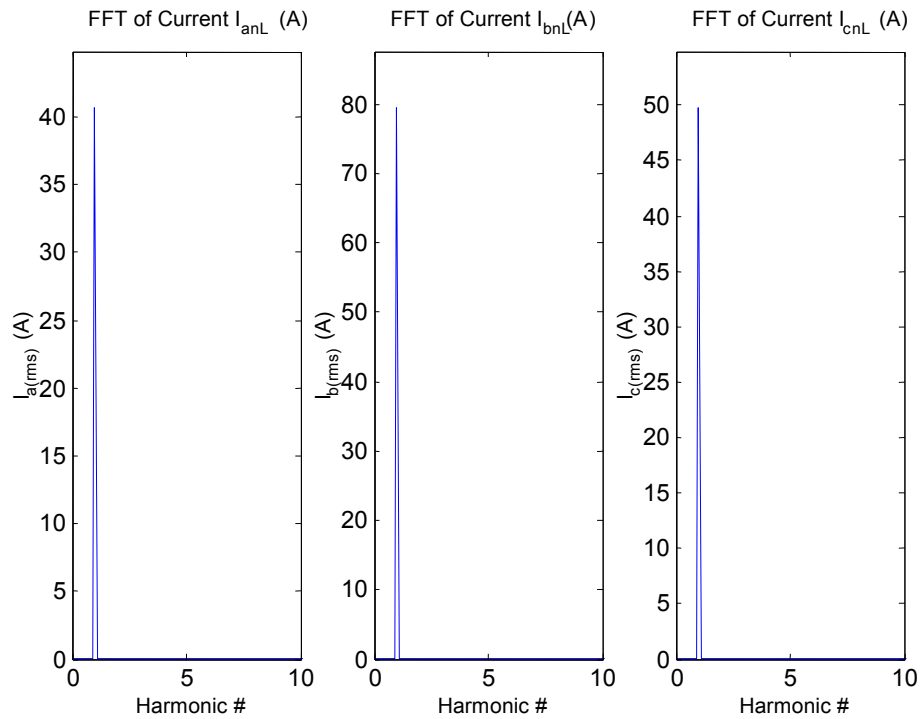


Figure 124: FFT of the load current in three phases for an unbalanced resistive load

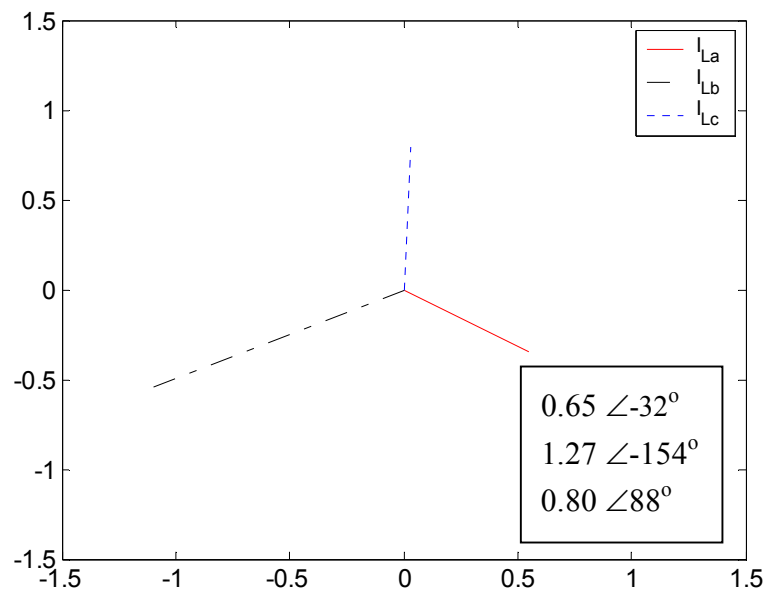


Figure 125: Phasor diagram of the three-phase currents for an unbalanced resistive load

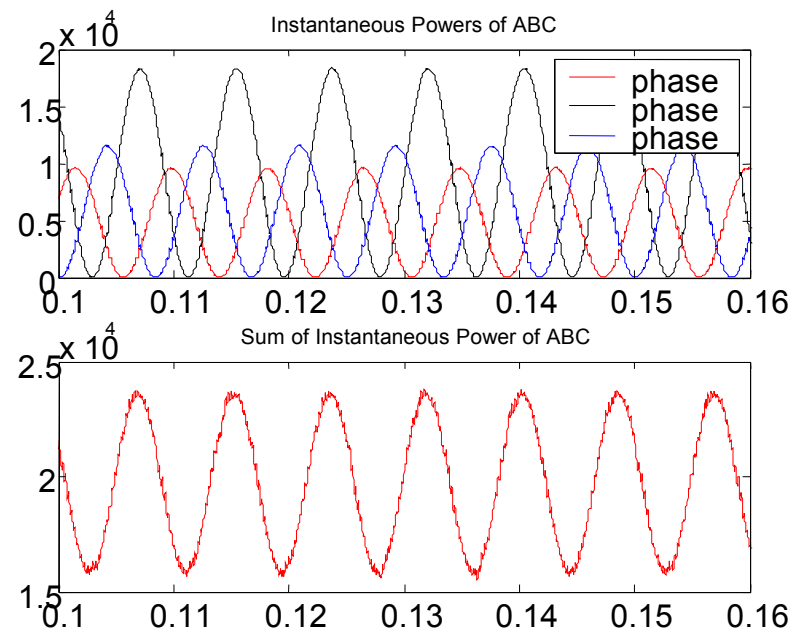


Figure 126: Instantaneous powers in three phases (top) and total power (bottom) for an unbalanced resistive load

An unbalanced three-phase/four-wire load is also simulated to examine the performance of the MSDG system. The simulation waveforms for a three-phase unbalanced inductive load are displayed in Figures 126 through 134. In this case, the load elements, resistance R_x and inductive reactance X_x are given by:

$$R_a = \frac{V_{rms}^2}{P_o} \quad (57)$$

$$R_b = 0.5 R_a$$

$$R_c = 0.8047 R_a$$

$$X_a = \frac{V_{rms}^2}{P_o} \quad (58)$$

$$X_b = 0.5 X_a$$

$$X_c = 0.8047 X_a$$

where $V_{rms} = 208$ V and $P_o = 15,000$ W.

The transformer secondary voltage waveforms with respect to the neutral are shown in Figure 127. Subscript 'x' in the label of the figure represents any one of the three phases. The FFT of the three-phase voltages is plotted in Figure 128. Figure 129 gives the phasor diagrams of these three phase-neutral voltages. From Figures 128 and 129, it is observed that the terminal voltages are unequal and so is the regulation in the three phases. Regulation is computed to be about 3% in phase 'a,' 5% in phase 'b' and 4% in phase 'c.' Figure 130 shows the filter inductor current waveform. These currents are unequal in the three phases and show distortion owing to resonance of the filter inductor with the capacitor. The three-phase load currents drawn by the series RL load are displayed in Figure 131. The FFTs of these three-phase load currents are plotted in Figure 132. The phasor diagram of these load currents is illustrated in Figure 133. As seen in Figures 132 and 133, the currents drawn by the unbalanced inductive load are unequal in magnitude in the three phases and are almost equally displaced in phase. This is because the three-phase/four-wire loads have equal power factor in spite of having unbalance in magnitude. Notably, the sum of the three-phase load currents is not equal to zero; and this contributes to a neutral current in the load that becomes the circulating current in the transformer primary (delta) winding. Figure 134 gives the instantaneous three-phase powers and the total power drawn by the unbalanced inductive load. The instantaneous powers of the three phases are of double the fundamental frequency, i.e., 120 Hz. The sum of the three instantaneous powers is called the three-phase instantaneous power drawn by the inductive load. It is the equal to the sum of the instantaneous real power and the reactive power drawn in three phases. As seen in Figure 134, the three-phase instantaneous power drawn by the unbalanced load is a sinusoidal waveform unlike that of balanced load, which was nearly constant (Ref. Figure 110). The average value of the three-phase instantaneous power gives the three-phase real power drawn by the load.

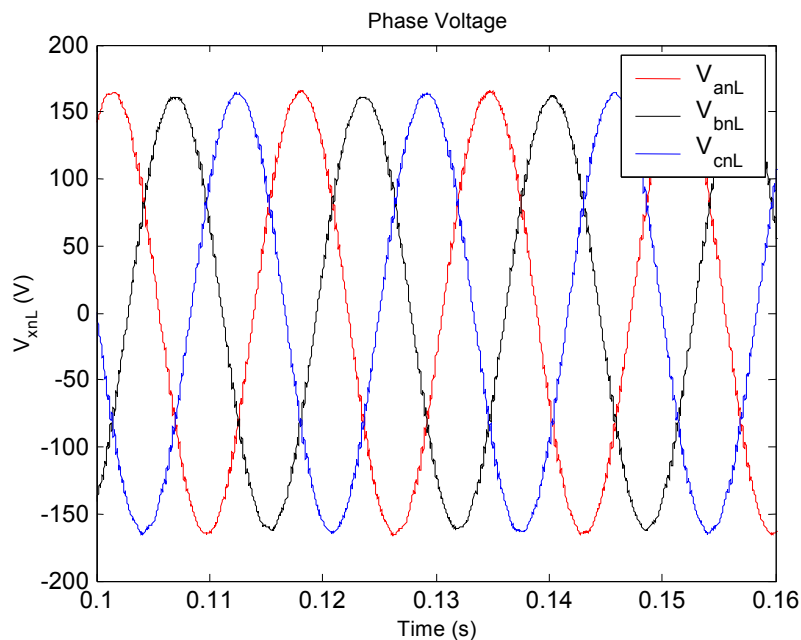


Figure 127: Transformer secondary terminal voltage waveform for an unbalanced inductive load

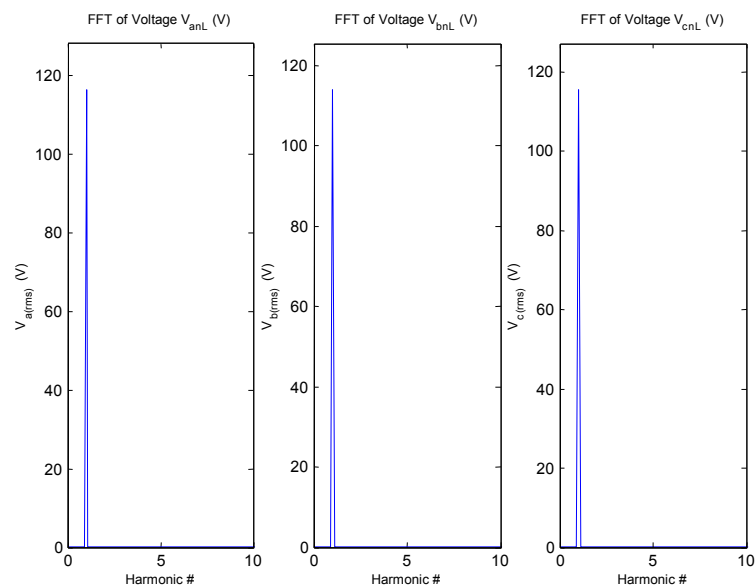


Figure 128: FFT of the transformer secondary terminal voltage in three phases for an unbalanced inductive load

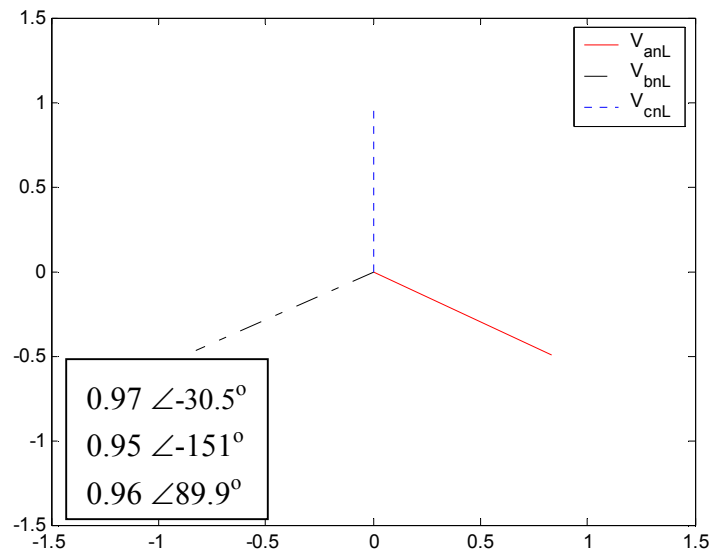


Figure 129: Phasor diagram of the three-phase voltages for an unbalanced inductive load

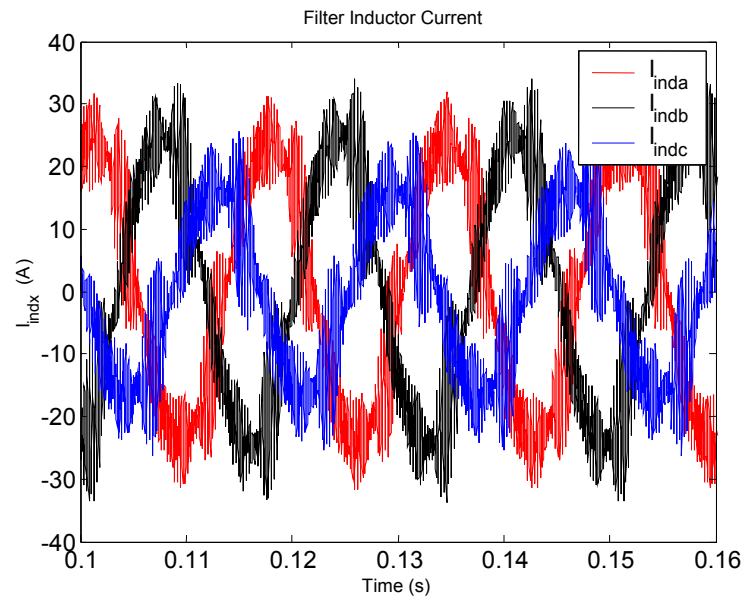


Figure 130: Three-phase filter inductor current waveform for an unbalanced inductive load

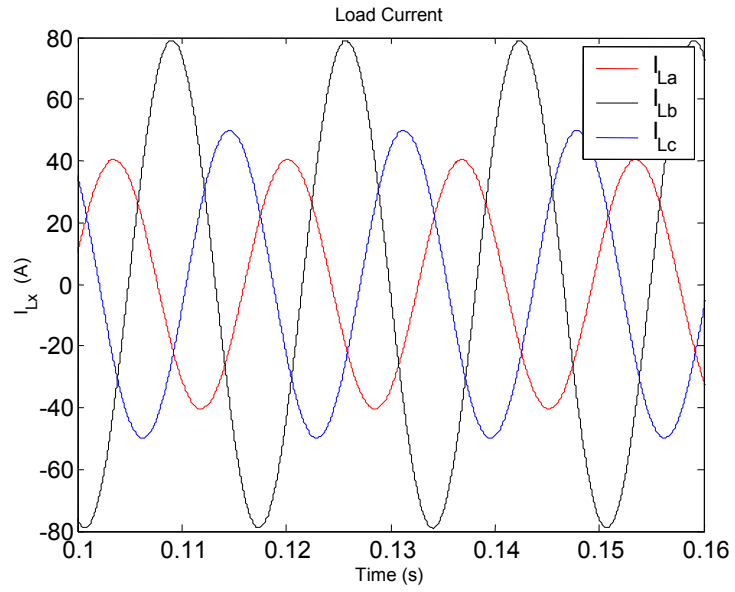


Figure 131: Three-phase load current waveform for an unbalanced inductive load

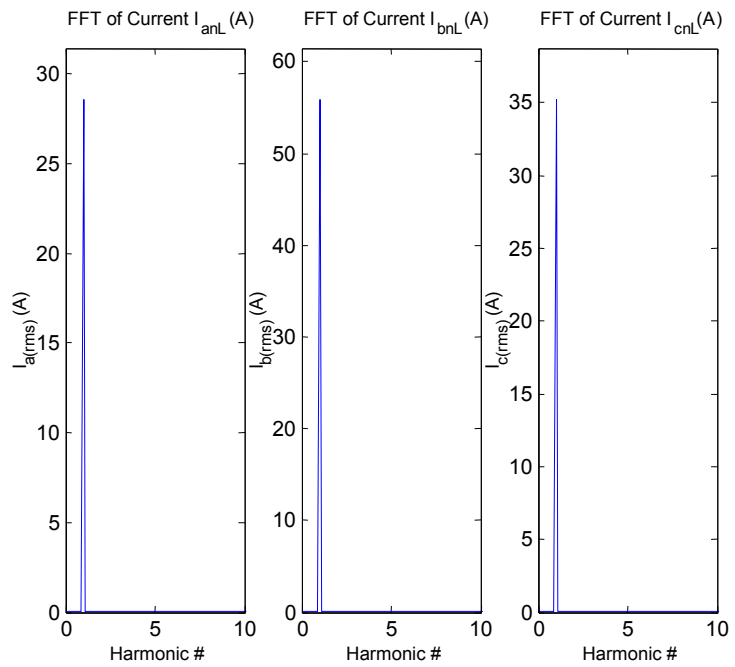


Figure 132: FFT of the load current in three phases for an unbalanced inductive load

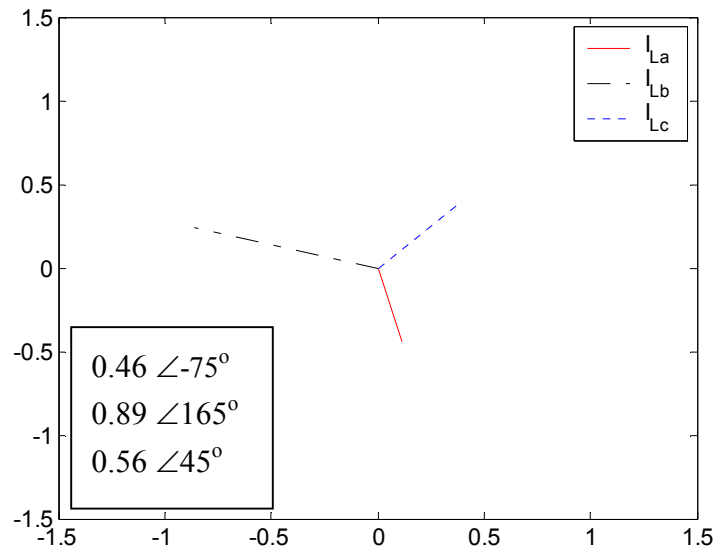


Figure 133: Phasor diagram of the three-phase currents for an unbalanced inductive load

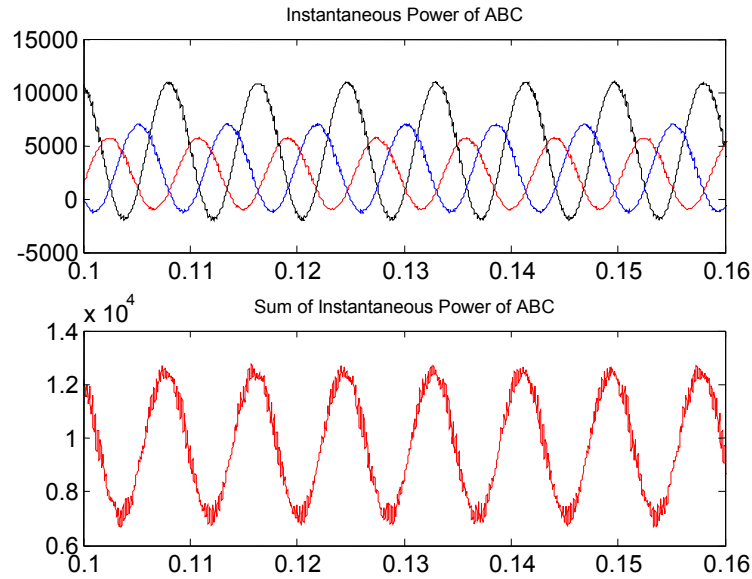


Figure 134: Instantaneous powers in three phases (top) and total power (bottom) for an unbalanced inductive load

An unbalanced three-phase/four-wire capacitive (parallel RC) load is also simulated to examine the performance of the MSDG system. The simulation waveforms for this case are displayed in Figures 135 through 142. In this case, the load elements, resistance R_x and inductive reactance X_x are given by:

$$R_a = \frac{V_{rms}^2}{P_o} \quad (59)$$

$$R_b = 2 R_a$$

$$R_c = 10 R_a$$

$$X_a = \frac{V_{rms}^2}{P_o} \quad (60)$$

$$X_b = 2 X_a$$

$$X_c = 10 X_a$$

where $V_{rms} = 208$ V and $P_o = 15,000$ W.

The transformer secondary voltage waveforms with respect to the neutral are shown in Figure 135. Subscript 'x' in the label of the figure represents any one of the three phases. The FFT of the three-phase voltages is plotted in Figure 136. Figure 137 gives the phasor diagrams of these three phase-neutral voltages. From Figures 136 and 137, it is observed that the terminal voltages are unequal and so is the regulation in the three phases. Regulation is computed to be about -2% in phase 'a,' 0% in phase 'b' and -1% in phase 'c.' Figure 138 shows the filter inductor current waveform. These currents are unequal in the three phases and show distortion owing to resonance of the filter inductor with the capacitor. The three-phase load currents drawn by the parallel RC load are displayed in Figure 139. The FFTs of these three-phase load currents is plotted in Figure 140. The phasor diagram of these load currents is illustrated in Figure 141. As seen in Figures 140 and 141, the currents drawn by the unbalanced capacitive load are unequal in magnitude in the three phases and are almost equally displaced in phase. This is because the three-phase/four-wire loads have equal power factor in spite of having unbalance in magnitude. Notably, the sum of the three-phase load currents is not equal to zero; and this contributes to a neutral current in the load that becomes the circulating current in the transformer primary (delta) winding. Figure 142 gives the instantaneous three-phase powers and the total power drawn by the unbalanced capacitive load. The instantaneous powers of the three phases are of double the fundamental frequency, i.e., 120 Hz. The sum of the three instantaneous powers is called the three-phase instantaneous power drawn by the capacitive load. It is the equal to the sum of the instantaneous real power and the reactive power drawn in three phases. As seen in Figure 142, the three-phase instantaneous power drawn by the unbalanced load is a sinusoidal waveform unlike that of a balanced load, which was nearly constant (Ref. Figure 118). The average value of the three-phase instantaneous power gives the three-phase real power drawn by the load.

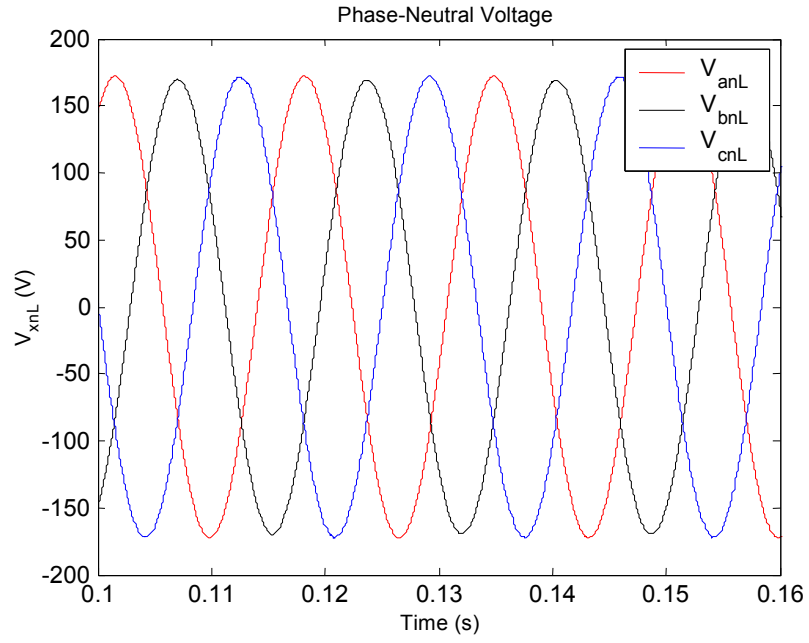


Figure 135: Transformer secondary terminal voltage waveform for an unbalanced capacitive load

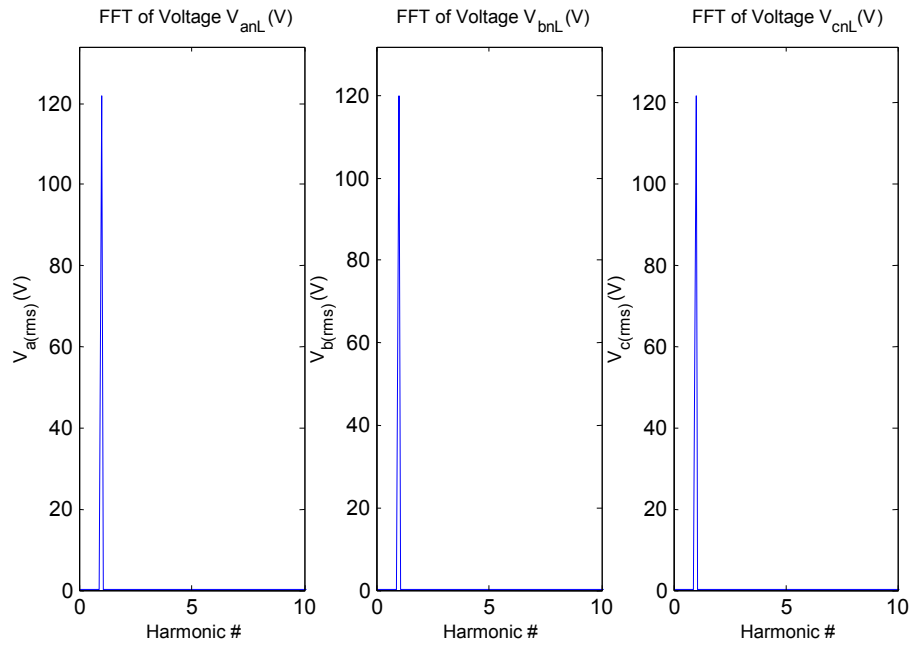


Figure 136: FFT of the transformer secondary terminal voltage in three phases for an unbalanced capacitive load

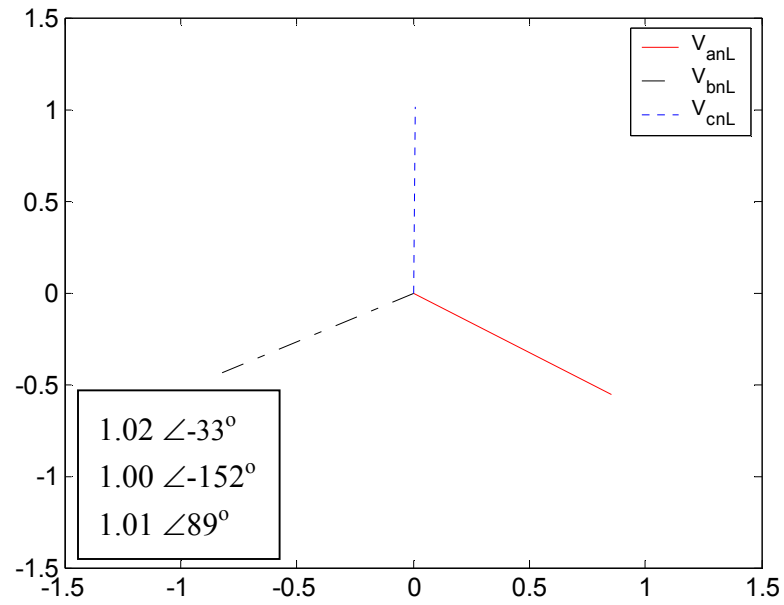


Figure 137: Phasor diagram of the three-phase voltages for an unbalanced capacitive load

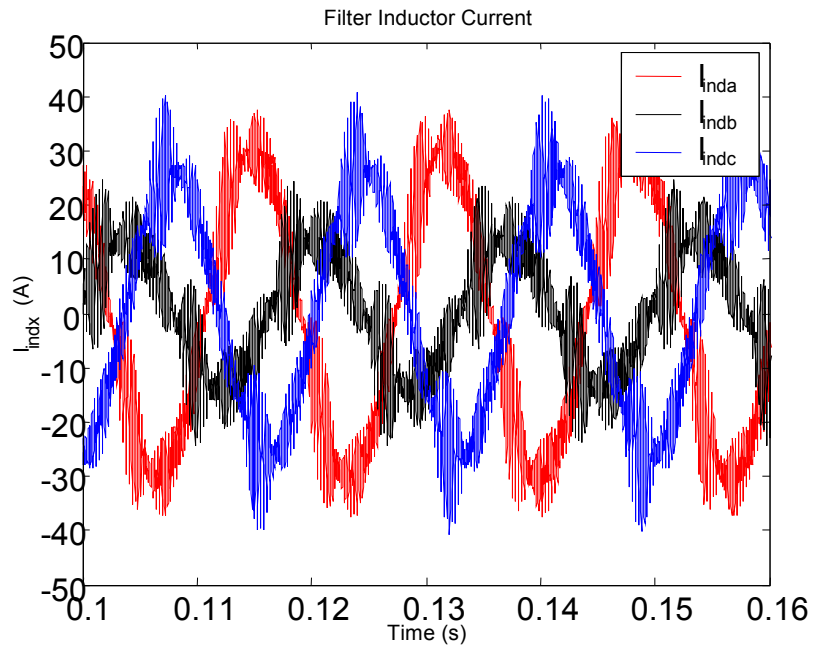


Figure 138: Three-phase filter inductor current waveform for an unbalanced capacitive load

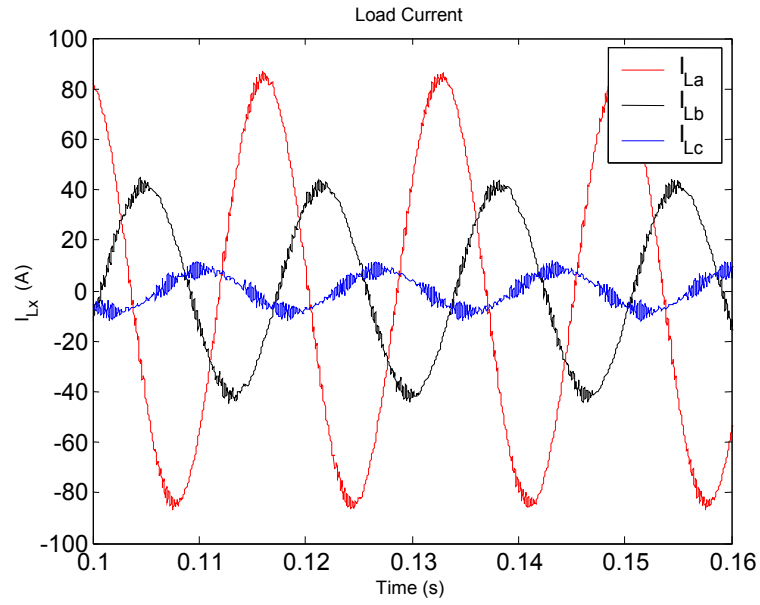


Figure 139: Three-phase load current waveform for an unbalanced capacitive load

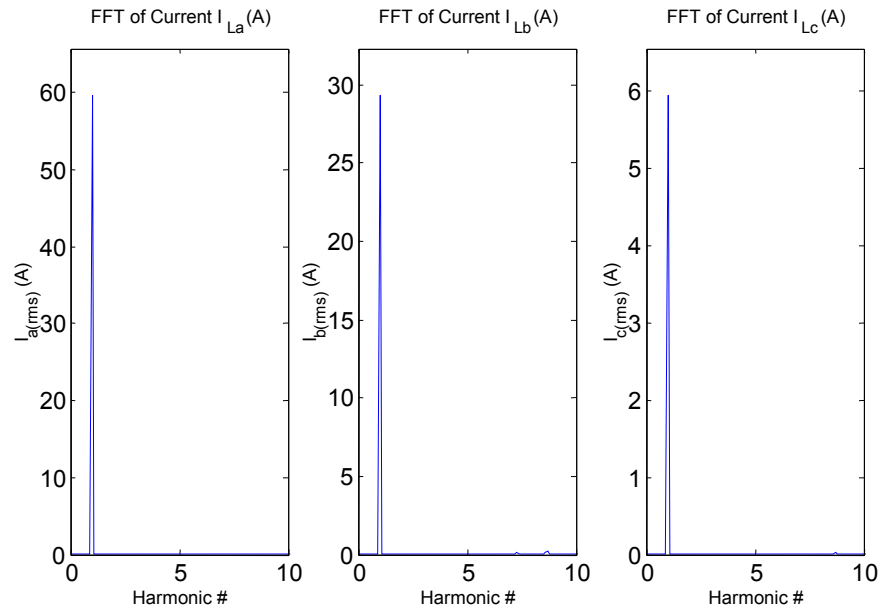


Figure 140: FFT of the load current in three phases for an unbalanced capacitive load

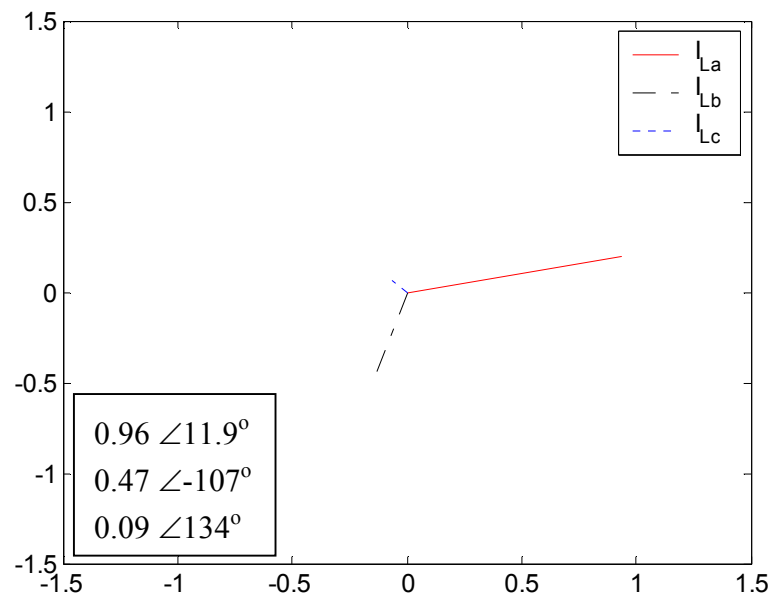


Figure 141: Phasor diagram of the three-phase currents for an unbalanced capacitive load

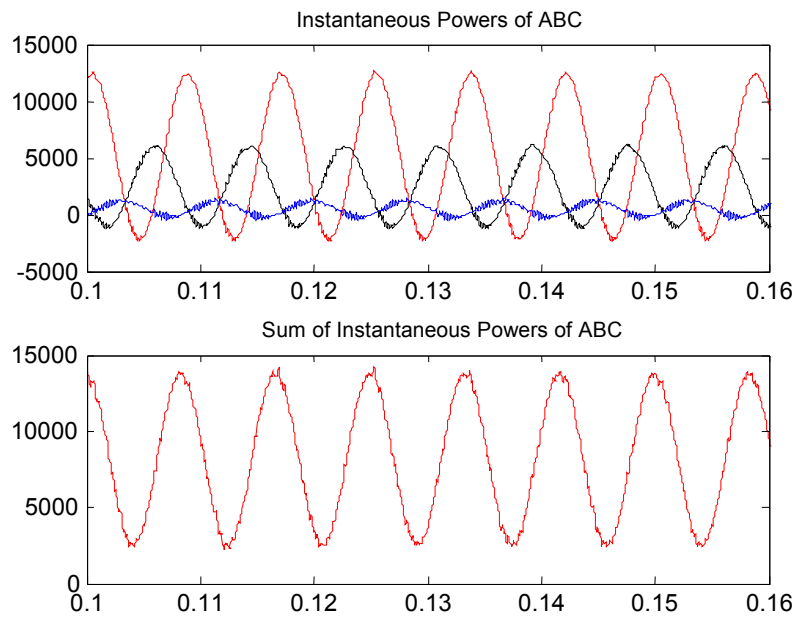


Figure 142: Instantaneous powers in three phases (top) and total power (bottom) for an unbalanced capacitive load

7.3 Experimental Testing of the Island Mode MSDG System

In this section, the steady state and transient behaviors of an island mode MSDG system when connected to different classes of loads are presented. Various loads, including linear loads — such as resistive, inductive and capacitive loads — as well as nonlinear loads — such as rectifiers — are used for this purpose. The performance of the system to unbalanced loads is also investigated.

The experimental setup has been described and the system parameters given in the previous chapters. The waveforms obtained from the experiment are presented below. Figure 143 gives the filter capacitor voltage and filter inductor current for the resistive load case. As seen in Figure 143, the filter inductor current is observed to contain harmonics while the filter capacitor voltage is sinusoidal. This is due to the nonlinear nature of the magnetizing current of the transformer [19]. Figure 144 illustrates the load terminal voltage and the load current for the same case. It is observed that for the resistive load, the current drawn by the load is in phase with the load terminal voltage. This is also evident from the phasor diagrams of voltage and current shown in Figure 145. The measurements made on the RisACE2000™ power analyzer of Rochester Instrument Systems® [20] are tabulated in Table 9.

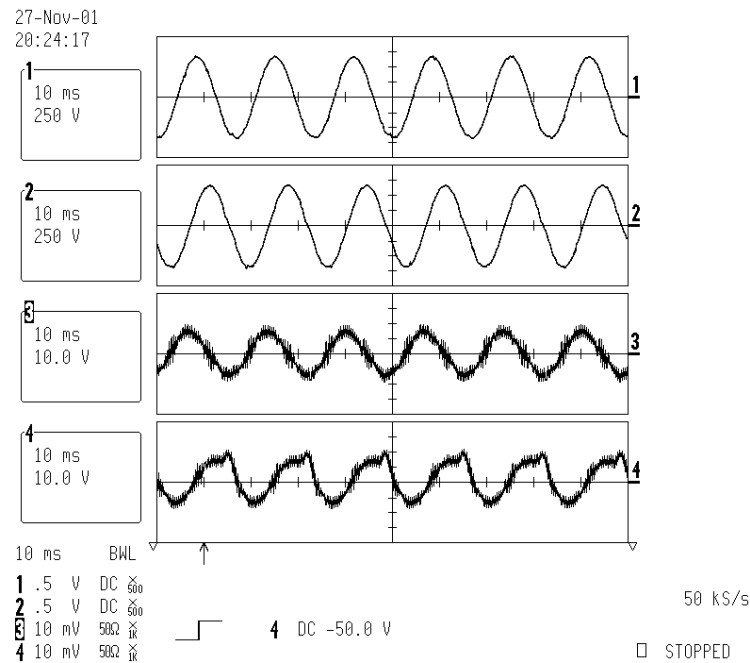


Figure 143: Filter capacitor line voltage ac & bc (top two) and filter inductor current a & b (bottom two) for a resistive load
The current is scaled at 1 A = 1 V.

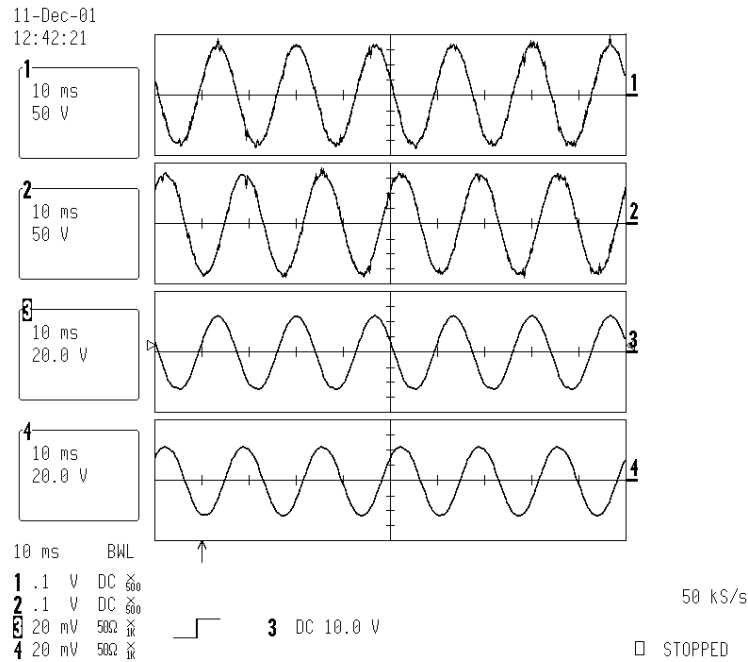


Figure 144: Load terminal voltage a & b (top two) and load current a & b (bottom two) for a resistive load
The current is scaled at 1 A = 1 V.

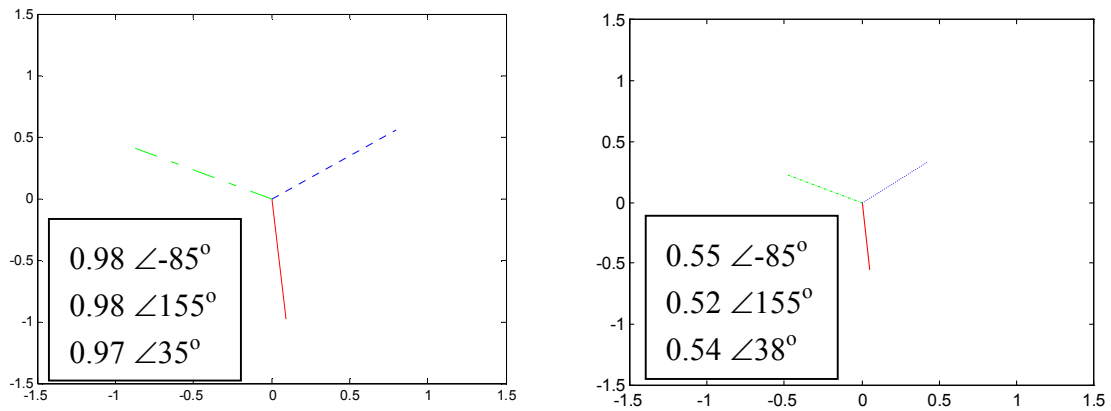


Figure 145: Phasor diagrams of load terminal voltage (left) and load current (right) for a resistive load (in pu)

Table 9: RisACE2000™ measurements for a resistive load

Voltage (V)	Current (A)	Real power (kW)	Reactive power (kVAr)	Power factor
119.5	30.34	10.89	-0.391	0.996 (leading)

Figure 146 gives the filter capacitor voltage and filter inductor current for a series RL load case. As in the resistive load case, the filter inductor current is observed to contain harmonics while the filter capacitor voltage is sinusoidal. This is due to the nonlinear nature of the magnetizing current of the transformer. Figure 147 illustrates the load terminal voltage and the load current. It is observed that the phase angle of the current drawn by the load lags that of the terminal voltage. This observation can also be made from the phasor diagrams shown in Figure 148. The measurements made on the RisACE2000™ for an inductive load are tabulated in Table 10.

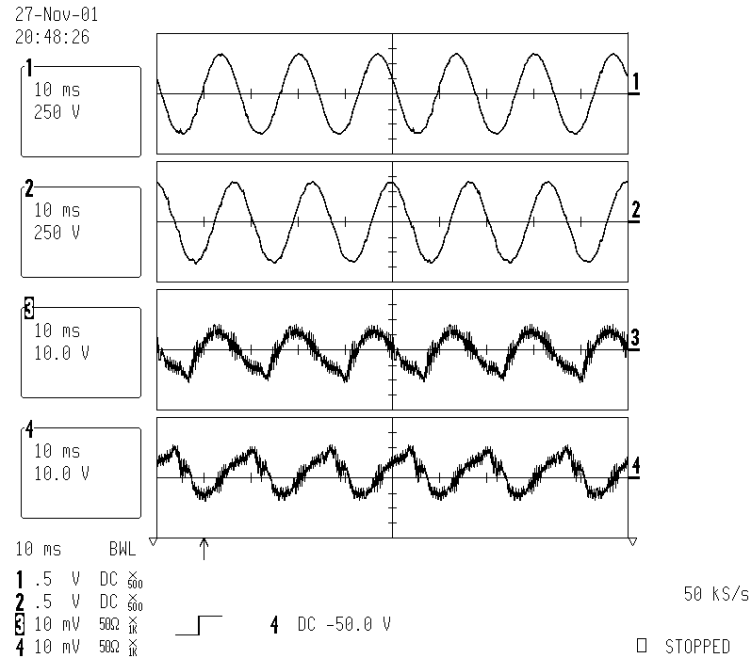
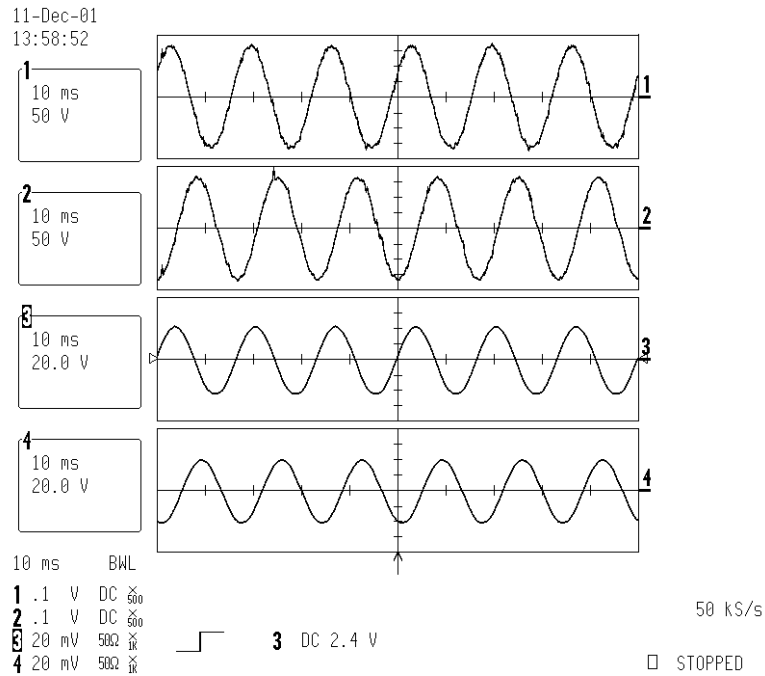
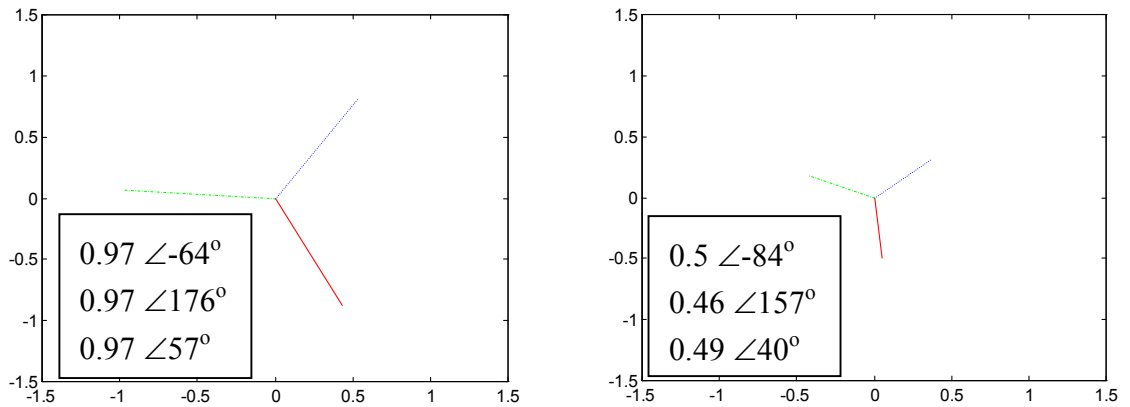


Figure 146: Filter capacitor line voltage ac & bc (top two) and filter inductor current a & b (bottom two) for a series RL load
The current is scaled at 1 A = 1 V.

The terminal voltage and load current waveforms for a capacitive load are illustrated in Figure 149. The load consists of power factor correction capacitors in parallel with a resistance connected to the secondary of the 480 V/208 Y (120 V) transformer. There is distortion in the load current waveform as some of the frequencies injected by the PWM inverter are excited by the capacitive load and the LC filter plus transformer. The load current leads the terminal voltage in this case. This is also evident from the phasor diagrams shown in Figure 150. The measurements made on RisACE2000™ for the capacitive load are tabulated in Table 11. The capacitive loads may draw large currents while getting charged. In case these large currents persist for long duration, the electric equipment will be damaged. As a safety measure, the capacitors are protected by fuses and have discharge resistors across them.



**Figure 147: Load terminal voltage a & b (top two)
and load current a & b (bottom two) for a series RL load**
The current is scaled at 1 A = 1 V.



**Figure 148: Phasor diagrams of load terminal voltage (left)
and load current (right) for a series RL load (in pu)**

Table 10: RisACE2000™ measurements for a series RL load

Voltage (V)	Current (A)	Real Power (kW)	Reactive Power (kVAr)	Power Factor
118.3	27.03	9.13	2.83	0.952 (lagging)

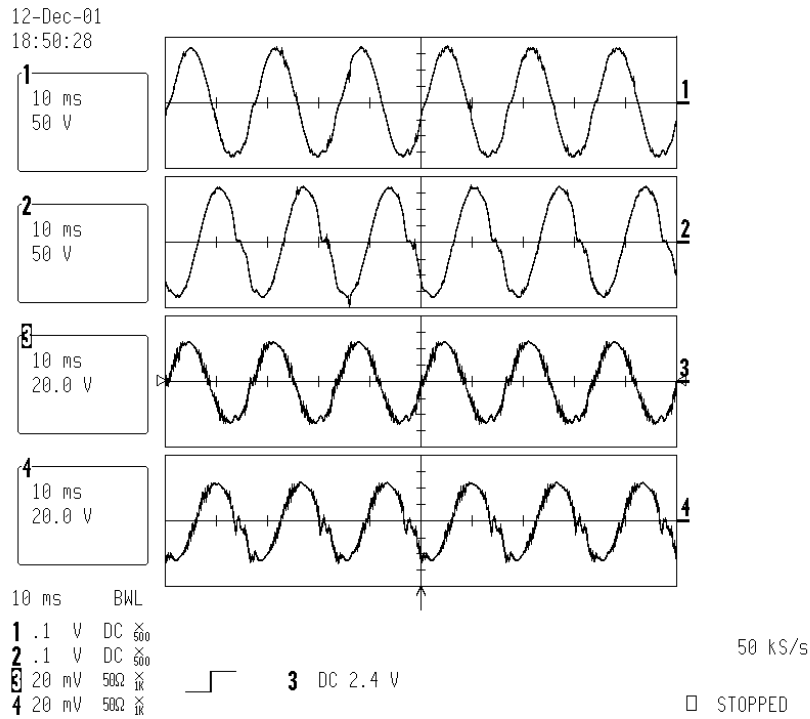


Figure 149: Load terminal voltage a & b (top two) and load current a & b (bottom two) for a parallel RC load
The current is scaled at 1 A = 1 V.

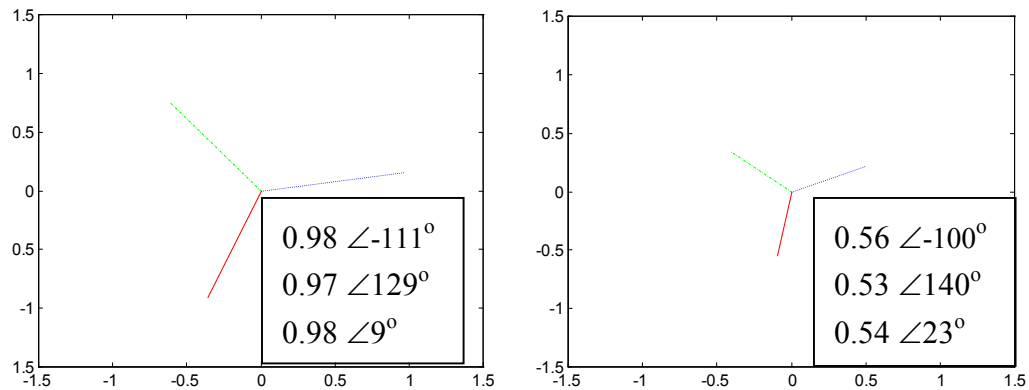


Figure 150: Phasor diagrams of load terminal voltage (left) and load current (right) for a parallel RC load (in pu)

Table 11: RisACE2000™ measurements for a parallel RC load

Voltage (V)	Current (A)	Real Power (kW)	Reactive Power (kVAr)	Power Factor
119.6	31.45	10.94	-2.592	0.966 (leading)

Experiments have been conducted on unbalanced and nonlinear loads also. Figure 151 gives the results for an unbalanced load. The load is a plasma-cutting machine made of soft switching power converters. It is a single-phase load that draws current only across two lines, a & b. To display the unbalance, waveforms of phases a and c are recorded. The load terminal voltage contains high frequency distortion, and the load current in phase 'a' is not a pure sinusoid. This is due to the nonlinear nature of the plasma-cutting machine. However, the waveform is nearly sinusoidal because of the power factor correction function available in the machine. The fundamental component of voltage and current is determined using FFT methods, and the phasor diagrams for the unbalanced load case are displayed in Figure 152. The measurements obtained on the RisACE2000™ power analyzer are tabulated in Table 12.

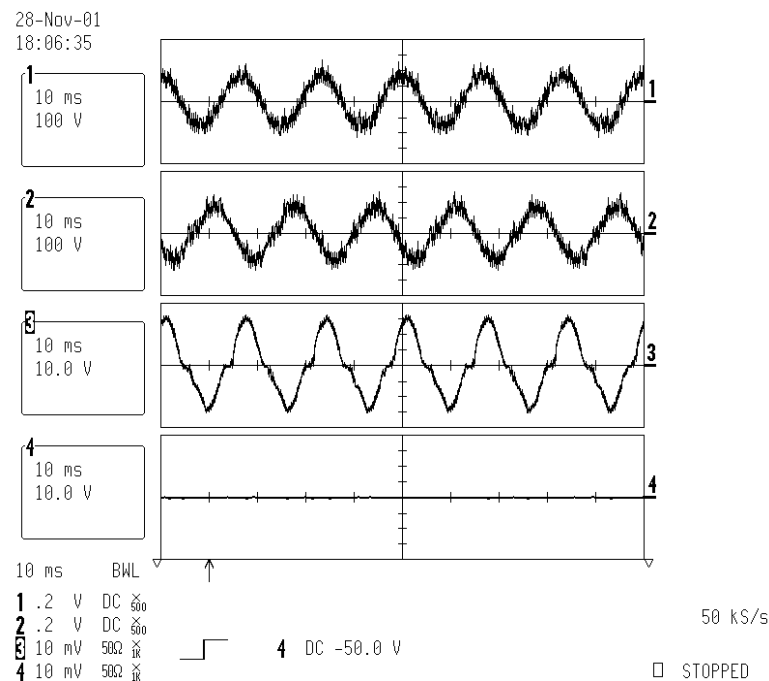


Figure 151: Load terminal voltage a & c (top two) and load current a & c (bottom two) for an unbalanced load
The current is scaled at 1 A = 1 V.

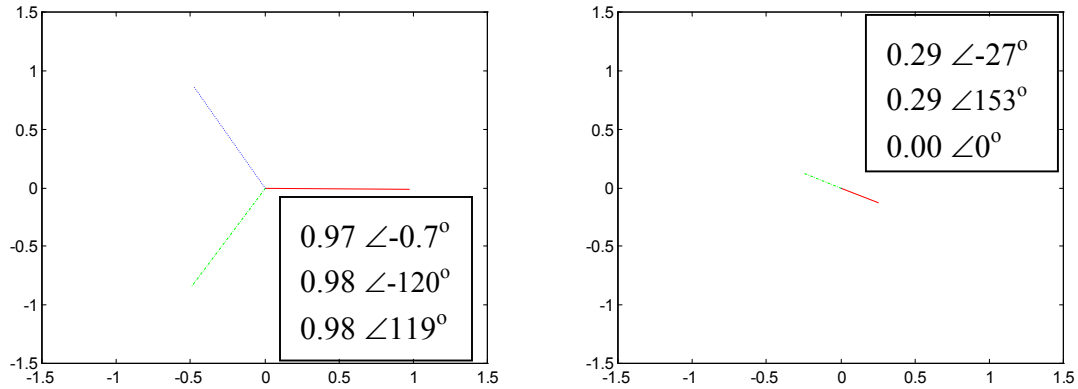


Figure 152: Phasor diagrams of load terminal voltage (left) and load current (right) for an unbalanced load (in pu)

Table 12: RisACE2000™ measurements for an unbalanced load

Phase	Voltage (V)	Current (A)	Real Power (kW)	Reactive Power (kVAr)	Power Factor
A	118.7	23.77	2.52	1.04	0.896 (lagging)
B	118.9	24.97	2.52	-1.79	0.756 (leading)
C	118.6	0	0	0	--

A three-phase diode bridge rectifier is used as a nonlinear load. The dc side of the diode bridge contains a capacitive load. The results obtained for a nonlinear load are shown in Figure 153. A precharge circuit for the dc bus capacitor is installed in the rectifier load that causes a little unbalance in the line currents drawn by the load. As seen in the figure, the terminal voltage waveform shows distortion. This is caused by the interaction of the LC filter (of the PWM inverter) and transformer with the nonlinear load.

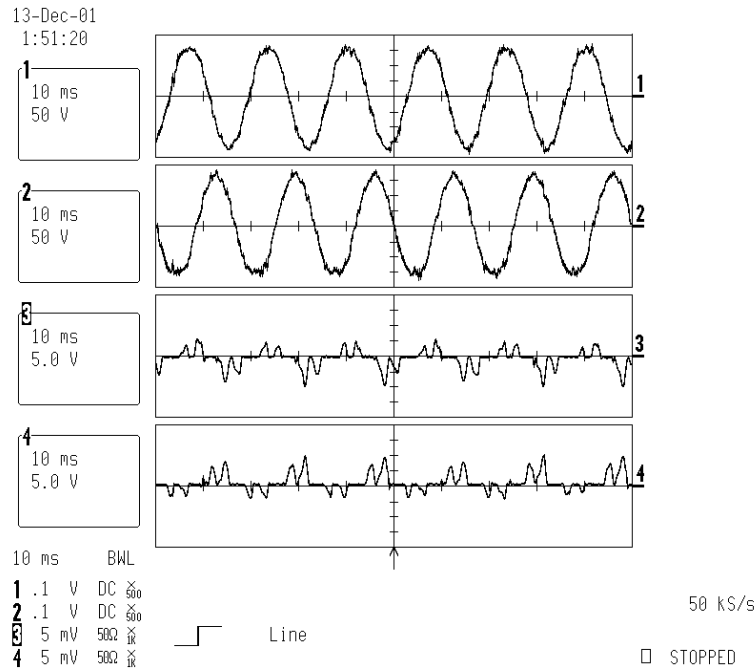


Figure 153: Load terminal voltage a & b (top two) and load current a & b (bottom two) for a three-phase diode rectifier
The current is scaled at 1 A = 1 V.

Table 8 gives the measurements made on the RisACE2000™ power analyzer for the rectifier load. The nonlinear loads such as rectifiers draw currents containing high amplitude pulses. The distortion in the current waveform recorded is very high as indicated by the total harmonic distortion (THD) of 93%. The MSDG system cannot support a nonlinear load to full power capacity because these loads draw high amplitude currents.

Table 13: RisACE2000™ measurements for three-phase diode bridge rectifier load

Voltage (V)	Current (A)	Real Power (kW)	Reactive Power (kVAr)	Power Factor	THD (%)
118	2.6	0.62	0.11	0.71 (lagging)	93.4

The waveforms showing transients in the voltage and current waveforms when the load is abruptly switched are recorded. Figure 154 illustrates the transients recorded on resistive load switching. The transformer secondary winding is in open-circuit condition before the load is connected to it. The transformer secondary voltage shows distortion before the load is connected because of the interaction between the LC filter and the magnetizing current of the transformer. The LC filter to the inverter is designed for a corner frequency of 933 Hz in order to minimize the interaction. It is observed that the distortion is reduced on application of the load.

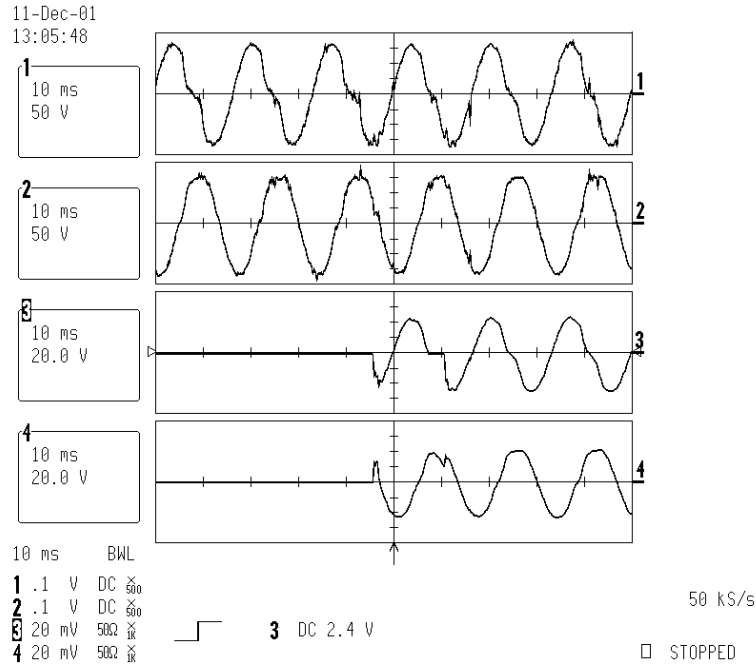


Figure 154: Transient waveforms – load terminal voltage a & b (top two) and load current a & b (bottom two) for a resistive load
The current is scaled at 1 A = 1 V.

The transient waveforms for an inductive (series RL) load are displayed in Figure 155. In the case of inductive load, the load current makes a smooth transition from its initial state to the steady state.

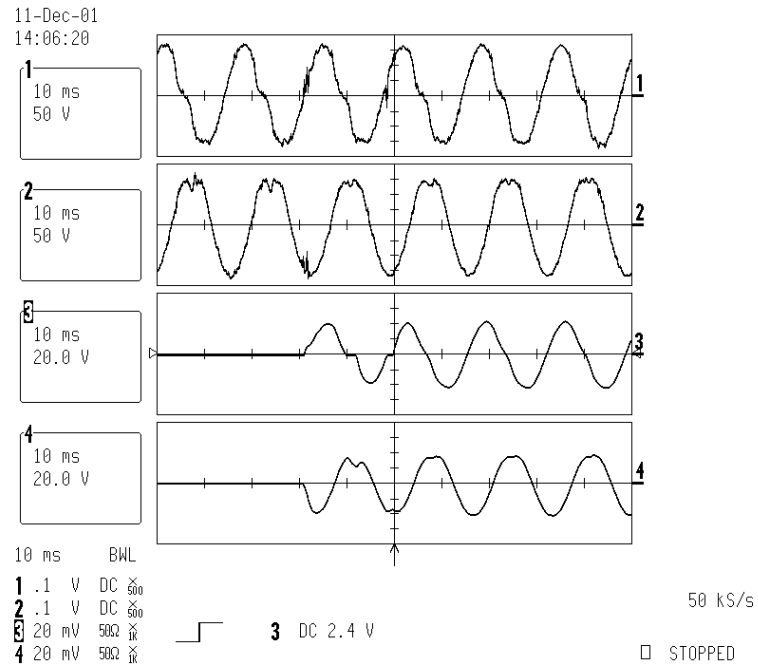


Figure 155: Transient waveforms – load terminal voltage a & b (top two) and load current a & b (bottom two) for a series RL load
The current is scaled at 1 A = 1 V.

8 Conclusions and Future Work

8.1 *Summary of Completed Work*

Micro-source generation systems are considered to be a valuable solution for providing power quality solutions for sensitive load scenarios while supplying electrical energy generated from environmentally preferred means at a competitive cost. However, they require additional energy storage to meet abrupt changes in power demand in the island mode. The inherent delay in the response of the micro-sources to fluctuations in power demand of the load is responsible for this requirement.

A detailed study is made herein for a micro-turbine-based generation system employing lead-acid batteries for energy storage. In this application, batteries are subjected to high-rate charging and discharging for a short interval of time, usually in the order 5 to 200 seconds. Thus, an MSDG system requires batteries with good charge acceptance and low internal resistance to maintain high power efficiency.

A guideline for the sizing of batteries for MSDG applications is presented. The design procedure takes into consideration the high-rate discharge effects on batteries. It ensures that the battery can provide the maximum instantaneous power required by the load. A provision is made for including UPS and cold start functionality in the MSDG system while sizing the batteries. The guidelines can be extended to other forms of MSDG systems and other types of batteries with some modifications.

A simulation is conducted using MATLAB Simulink™ software to verify the operation of the battery-based MSDG system. Mathematical models are used to represent typical load power demand and micro-source response. The lead-acid battery is represented by an equivalent circuit whose elements are functions of the battery parameters. The design strategy is verified by the response of the system to a step change in load demand.

The report highlights the necessity of having auxiliary energy storage for successful operation of MSDG systems in island mode for feeding sensitive loads.

A motor-drive inverter along with its controller has been successfully utilized for the utility application as an MSDG system. The inverter in an island mode MSDG system is rated to supply the total real and reactive power requirements of all loads connected to the system. Also, it requires being overrated to withstand possible over-voltages and over-currents under fault conditions that may occur in a power distribution system. For open-loop control, the inverter is operated using the V/f control scheme existing in the motor-drive controller. The initial phase of the controller is to ramp the ac voltage and frequency of the inverter to their reference set points. During this ramping phase, critical loads that are sensitive to the frequency of the ac power supplied are disconnected.

The major components of the MSDG system are the space-vector pulse-width modulator, the inverter, the LC filter, the Δ -Y transformer and the load. Their selection based on the design specifications is explained. These components are simulated as subsystems and grouped together to form the MSDG system model in MATLAB Simulink™ software. The results obtained from simulation are according to the theoretical concepts. It is observed that for an inductive load, the terminal voltage drops with increasing real power drawn from the island MSDG system.

An experimental platform of the MSDG system was built based on the design specifications. Additional protection circuitry is included to safeguard the equipment and meet the National Electricity Code® specifications. The experimental results verify the simulation results.

The modified inverter will be used to study and benchmark the performance of an island mode MSDG for a complex set of loads under the current phase of the project during the next task. During the subsequent phase option years of the project, more inverters will be integrated into the laboratory-scale microgrid to demonstrate a cluster of microsources that provide an industrial power system with high power quality.

MSDG systems are gaining more popularity because of increasing demand for a reliable power supply. An MSDG system can aid in improving the reliability of power supply when connected to such loads alongside the main grid supply. Nevertheless, it is also capable of operating independently to supply power to electrical loads where the main grid supply is unavailable for some reason. Another advantage of MSDG systems is the ability to add functions such as voltage sag correction and harmonic filtering.

Analytical models for an MSDG system consist of micro-sources such as micro-turbines, fuel cells, etc. that are interfaced to the ac system through an optional ac/dc rectifier, energy storage and a dc/ac inverter have been developed. The models have been used to study the regulation properties of the system. Power is transferred to the load by an inverter through the LC filter circuit and the Δ -Y transformer. Besides the power level and power factor of the load, the resistance and reactance of the LC filter plus transformer influence the terminal voltage characteristics and so its regulation. A positive regulation signifies that the terminal voltage falls in magnitude with increase in load, and a negative regulation signifies that the voltage rises with increase in load. It is observed that the regulation is positive for resistive and inductive loads and negative for capacitive loads. As expected, in the case of unbalanced three-phase/four-wire loads, the regulation is unequal in the three-phases. The MATHCAD™ software package has been used to perform the theoretical analysis, and results are presented for different classes of loads. These results have further been verified by conducting digital simulation in MATLAB Simulink™.

The time-domain waveforms are illustrated from digital simulation models of the system using MATLAB Simulink™ for different classes of linear loads, viz., balanced and unbalanced resistive, inductive and capacitive loads. Several performance characteristics are displayed in the form of Fast Fourier Transforms (FFTs), phasor diagrams, waveforms of currents, voltages and powers.

The experimental hardware had undergone extensive testing to benchmark the performance of the single inverter island mode system. Then, experimental results illustrated performance characteristics for different types of loads including balanced and unbalanced, linear and nonlinear loads, which show agreement with analytical and simulations results. While the system is capable of supplying rated power to linear loads, it can source less than rated power to nonlinear loads. This is because of the high-amplitude harmonic currents drawn by nonlinear loads such as rectifiers. It is observed that the design of the output LC filter is critical to obtain the desired performance under any load condition. A low corner frequency for the LC filter may cause interaction with harmonics injected by nonlinear loads. A higher corner frequency would make it ineffective in filtering the switching ripples of the inverter.

Some transient waveforms are also presented that reveal the performance of the system under starting conditions. The quality of waveforms deteriorates under nonlinear loads and transient conditions.

8.2 Future Work

The inverter controller will be modified further during the option year to maintain adequate power quality levels under these conditions. Simulation results already indicate an improvement of performance is achievable using augmented controllers [21].

The hardware platform that has been developed under this task will be expanded to include a cluster of inverters and various loads to enable the tasks listed in the option years to be completed. Figure 156 presents the photograph of the laboratory infrastructure, which incorporates cable trays to interconnect various source and load stations that have been developed under the project.



Figure 156: Photograph of cable tray system that forms the backbone of the laboratory-scale microgrid

During the option years of the project, the current electrical system will be expanded to incorporate grid interconnection through two additional inverters of various configurations. A schematic of the complete laboratory-scale microgrid is shown in Figure 4 in Chapter 1. Sections of the schematics illustrated in pink were completed during the current year. Option years tasks will complete the microgrid as subsequently. However, much of the physical infrastructure necessary for option years 2 and 3 has been put in place.

Specific tasks to be conducted during the option years include:

8.2.1 Expansion of Laboratory-Scale Microgrid to Allow Utility Interface with Two Inverters

This task is expected to result in a laboratory-scale microgrid that can be used to study the operational characteristics of two distributed generation inverters with and without utility interface.

8.2.2 Fabrication of Additional Power Source Emulator and Inverter Hardware

This task is expected to result in the availability of two laboratory-scale distributed generation systems to be used with the microgrid emulator to study various operating scenarios.

8.2.3 Demonstration of Islanding and Reconnection of Inverters with the Grid

This task is expected to result in demonstration of islanding and reconnection transients of two laboratory-scale distribution generation systems in a synergistic fashion.

8.2.4 Demonstration of Two Inverter System Under Power Quality Transient

This task is expected to result in the demonstration of the operation of a distributed generation system under typical power quality problems.

8.2.5 Computer Simulation

This task is expected to result in a detailed computer model of two distributed power inverters operating on a laboratory-scale island mode and utility interactive mode microgrid emulator.

9 References

- [1] *ITI (CBEMA) Curve Application Note*, Information Technology Industry Council (ITI), Washington D.C., 2000.
- [2] IEEE Std. 1346-1998, *IEEE Recommended Practice for Evaluating Electric Power System Compatibility with Electronic Process Equipment*, IEEE, New York, NY, 1998.
- [3] Lasseter, R.; Piagi, P. "Providing Premium Power Through Distributed Resources," *Advanced Technology*, HICSS – 33, Jan. 2000.
- [4] Draft Report for CERTS, *Year 2000 Testing of Capstone and Honeywell MTGs During Load Changes*, Southern California Edison, Irvine, Feb 1, 2001.
- [5] Larminie, James; Dicks, Andrew. *Fuel Cell Systems Explained*, John Wiley and Sons, 2000.
- [6] Willis, H.L.; Scott, W.G. *Distributed Power Generation Planning and Evaluation*, Marcel Dekker Inc., New York, 2000.
- [7] Akagi, H.; Kanazawa, Y.; Nabae, A. "Instantaneous Reactive Power Compensators Comprising Switching Devices without Energy Storage Components," *IEEE Trans. on Industry Applications*, Vol. IA-20, No. 3, May/June 1984, pp. 625 - 630.
- [8] Technical Marketing Staff, *Rechargeable Batteries Applications Handbook*, Gates Energy Products Inc., EDN Series for Design Engineers, Butterworth-Heinemann, MA, 1992.
- [9] *ABSOLYTE IIP Series Specifications*, GNB Technologies, Lombard, IL.
- [10] *NP Series Sealed Rechargeable Lead-Acid Battery Application Manual*, Yuasa Inc., Reading, PA.
- [11] *PNGV Battery Test Manual*, U.S. Department of Energy, Idaho National Engineering Laboratory, DOE/ID-10597, Jan. 1997.
- [12] Wiegman, H.L.N. *Battery State Estimation and Control for Power Buffering Applications*, Ph.D. Dissertation, University of Wisconsin-Madison, December 1999.
- [13] Capstone MicroTurbine™ Communication protocol, Capstone Turbine Corporation, CA
- [14] Salameh, Z.M.; Casacca, M.A.; Lynch, W.A. "A Mathematical Model for Lead-Acid Batteries," *IEEE Trans. on Energy Conversion*, Vol. 7, No. 1, March 1992, pp. 93 - 97.
- [15] Ryan, M.J.; Lorenz, R.D.. "A Novel Controls-Oriented Model of a PM Generator with Diode Bridge Output," *WEMPEC Research Report*, pp. 97-106.
- [16] Bergen, A.R. *Power Systems Analysis*, Prentice-Hall Inc., Eaglewood Cliffs, NJ, 1986.
- [17] Say, M.G. *The Performance and Design of Alternating Machines*, Pitman, London, 3rd Ed.

- [18] *ECE 712 Course Notes*, University of Wisconsin-Madison, WI.
- [19] Al-Haj, A.H.; El-Amin, I. "Factors That Influence Transformer No-Load Current Harmonics," *IEEE Trans. on Power Delivery*, Vol. 15, No. 1, January 2000, pp. 163 - 166.
- [20] *RisACE2000 – User Manual*, Rochester Instrument Systems, New York, NY.
- [21] Venkataramanan, G.; Illindala, M. "Microgrids and Sensitive Loads," panel paper presented at IEEE PES Winter Meeting, January 2002, NY.
- [22] *1336 Plus Adjustable Frequency AC Drive – User Manual*, Allen-Bradley Company Inc., Milwaukee, WI.
- [23] Al-Haj, A.H.; El-Amin, I. "Factors That Influence Transformer No-Load Current Harmonics," *IEEE Trans. on Power Delivery*, Vol. 15, No. 1, January 2000, pp. 163 - 166.
- [24] *9T23B3873 Datasheets*, GE Transformer Catalog, GE Industrial Systems, Fort Wayne, IN.

REPORT DOCUMENTATION PAGE			Form Approved OMB NO. 0704-0188	
Public reporting burden for this collection of information is estimated to average 1 hour per response, including the time for reviewing instructions, searching existing data sources, gathering and maintaining the data needed, and completing and reviewing the collection of information. Send comments regarding this burden estimate or any other aspect of this collection of information, including suggestions for reducing this burden, to Washington Headquarters Services, Directorate for Information Operations and Reports, 1215 Jefferson Davis Highway, Suite 1204, Arlington, VA 22202-4302, and to the Office of Management and Budget, Paperwork Reduction Project (0704-0188), Washington, DC 20503.				
1. AGENCY USE ONLY (Leave blank)		2. REPORT DATE November 2002		3. REPORT TYPE AND DATES COVERED Subcontract: December 2000—November 2001
4. TITLE AND SUBTITLE Hardware Development of a Laboratory-Scale Microgrid Phase 1—Single Inverter in Island Mode Operation: Base Year Report, December 2000—November 2001			5. FUNDING NUMBERS CF: AAD-0-30605-14 DP03.1001	
6. AUTHOR(S) G. Venkataramanan, M.S. Illindala, C. Houle, and R.H. Lasseter				
7. PERFORMING ORGANIZATION NAME(S) AND ADDRESS(ES) Wisconsin Power Electronics Research Center 1414 Engineering Drive Madison, WI 53706			8. PERFORMING ORGANIZATION REPORT NUMBER	
9. SPONSORING/MONITORING AGENCY NAME(S) AND ADDRESS(ES) National Renewable Energy Laboratory 1617 Cole Blvd. Golden, CO 80401-3393			10. SPONSORING/MONITORING AGENCY REPORT NUMBER NREL/SR-560-32527	
11. SUPPLEMENTARY NOTES NREL Technical Monitor: Holly Thomas				
12a. DISTRIBUTION/AVAILABILITY STATEMENT National Technical Information Service U.S. Department of Commerce 5285 Port Royal Road Springfield, VA 22161			12b. DISTRIBUTION CODE	
13. ABSTRACT (<i>Maximum 200 words</i>) This report summarizes the activities of the first year of a three-year project to develop control software for micro-source distributed generation systems. The focus of this phase was on internal energy storage requirements, the modification of an off-the-shelf motor drive system inverter to supply utility-grade ac power, and a single inverter system operating in island mode. The report provides a methodology for determining battery energy storage requirements, a method for converting a motor drive inverter into a utility-grade inverter, and typical characteristics and test results of using such an inverter in a complex load environment.				
14. SUBJECT TERMS Distributed generation; distributed power; distributed energy; island mode operation; microgrid; inverter; hardware; interconnection; system integration			15. NUMBER OF PAGES	
			16. PRICE CODE	
17. SECURITY CLASSIFICATION OF REPORT Unclassified	18. SECURITY CLASSIFICATION OF THIS PAGE Unclassified	19. SECURITY CLASSIFICATION OF ABSTRACT Unclassified	20. LIMITATION OF ABSTRACT UL	